Towards Hybrid Wakefield Acceleration

Max F. Gilljohann

München 2021

Towards Hybrid Wakefield Acceleration

Max F. Gilljohann

Dissertation
der Fakultät für Physik
der Ludwig-Maximilians-Universität
München

vorgelegt von
Max F. Gilljohann
aus Solingen

München, den 24.10.2021

Erstgutachter: Prof. Dr. Stefan Karsch
Zweitgutachter: Prof. Dr. Ulrich Schramm
Tag der mündlichen Prüfung: 10.03.2022

Zusammenfassung

Teilchenbeschleuniger spielen eine wichtige Rolle in vielen Bereichen der Forschung, wie Hochenergie-Physik, Medizin, Chemie und Materialforschung. Moderne Teilchenbeschleuniger basieren auf Mikrowellenresonatoren, deren Beschleunigungsgradienten durch Vakuumdurchschläge limitiert sind, was dazu führt, dass sie groß und teuer sind. Plasmabasierte Beschleuniger, wie Laser- und Teilchen-getriebene Kielfeldbeschleuniger (LWFAs und PWFAs), versprechen mit ihren drei Größenordnungen höhere Beschleunigungsgradienten (im Bereich von $100\,\mathrm{GeV\,m^{-1}}$) dieses Problem zu lösen.

LWFA erlaubt es kompakte und kosteneffiziente Beschleuniger mit Teilchenenergien bis 10 GeV und Teilchenströmen über 1 kA zu erzeugen. Sie besitzen außerdem inhärent synchronisierte Laser für viele verschiedene Anwendungen. Die Stabilität und Energieverteilung ist normalerweise jedoch noch weit entfernt von Mikrowellenresonatorenbasierten Systemen. Das PWFA-Konzept erreicht deutlich höhere Energien und verspricht ultra-hohe Strahlqualitäten. Es ist daher potenziell hervorragend geeignet um Freie Elektronenlaser mit harter Röntgenstrahlung (XFELs) zu treiben, und ist ein aussichtsreicher Kandidat für zukünftige Generationen von großen Beschleunigeranlagen. Es besteht daher ein großes Interesse den PWFA-Prozess zu erforschen und weiterzuentwickeln, jedoch existieren weltweit nur eine Handvoll Forschungseinrichtungen in denen dies möglich ist.

Das neuartige Konzept der *hybriden Kielfeldbeschleuniger* kombiniert die Vorteile von LWFA und PWFA in einen einzelnen Beschleuniger. Dabei werden die LWFA-erzeugten Elektronenstrahlen benutzt um den PWFA-Prozess zu treiben. Dies erlaubt einzigartige Möglichkeiten für fundamentale PWFA-Forschung in weit verbreiteten Laseranlagen, und die Perspektive von ultra-hohen Elektronenstrahlqualitäten, der Kompaktheit und dem synchronisierten Laser machen sie zu einem idealen Treiber von XFELs.

In dieser Arbeit präsentiere ich die erste experimentelle Umsetzung eines hybriden Kielfeldbeschleunigers. Zu diesem Zweck wurden unübertroffene Strahlqualitäten in einer LWFA-Stufe erzeugt, die dazu benutzt wurden den PWFA-Prozess in einer zweiten Stufe zu treiben und einen zweiten Elektronenstrahl mit Gradienten von über $10\,\mathrm{GeV\,m^{-1}}$ zu beschleunigen. Dieser zweite Elektronenstrahl wird ebenso in der LWFA-Stufe erzeugt, und (extern) in die PWFA-Stufe mit einer Effizient von über 50 % eingekoppelt.

Weiterhin nutzen wir den hybriden Beschleuniger um fundamentale PWFA-Forschung zu betreiben. Unsere Schattenbild-Diagnostik zeigt die Formierung eines ringförmigen Ionenkanals in dem PWFA-Prozess, der einige Jahre zuvor vorhergesagt wurde und weitreichende Implikationen für einige Arten von Plasmabeschleunigern wie AWAKE am CERN hat. Nach unseren Kenntnissen ist dies die erste experimentelle Demonstration.

Mit diesen beiden Meilensteinen demonstrieren wir nicht nur die experimentelle Machbarkeit eines hybriden Kielfeldbeschleunigers, sondern auch sein Potenzial bei der Erforschung zukünftiger Beschleuniger.

Abstract

Particle accelerators play an important role in many fields of research, like high-energy physics, medicine, chemistry and material science. State-of-the-art accelerators are based on radio-frequency (RF) cavities, which suffer from limited acceleration gradients because of vacuum breakdown. This leads to machines like particle colliders and accelerator-based light sources being large and expensive. Plasma based accelerators, such as laser- and particle-driven wakefield accelerators (LWFAs, PWFAs), promise to solve this problem by offering acceleration gradients on the order of $100\,\mathrm{GeV\,m^{-1}}$, which exceeds the ones of RF accelerators by more than three orders of magnitude.

LWFA and PWFA both come with their individual advantages, but also challenges. LWFA allows to build overall compact and cost-efficient accelerators with particle energies of up to 10 GeV and currents exceeding the kA-level. It furthermore inherently comes with a well synchronized laser for various applications. However, the stability and energy spread in LWFA systems is usually far from state-of-the-art RF accelerators. The PWFA scheme, on the other hand, achieves much higher beam energies in a single stage and promises ultra-high beam qualities. It is thereby potentially well suitable to drive hard X-ray free-electron-lasers (XFELs) and is arguably the most promising candidate for future generations of large-scale accelerators. So, there is a strong interest in studying and developing the PWFA process, but it requires a highly relativistic particle driver in the first place. So far, there are only a handful PWFA research facilities worldwide, like FACET-II at SLAC and FLASHForward at DESY, because they require kilometer-long RF accelerators and are hence large and expensive.

The novel scheme of *hybrid wakefield acceleration* combines the advantages of LWFA and PWFA into a single accelerator by driving the PWFA process with LWFA-generated electron beams. This enables unique opportunities for fundamental PWFA research in widely available laser facilities, and the prospect of ultra-high beam qualities, compactness and a synchronized laser makes them an ideal driver for XFELs,

In this thesis, I present the first experimental realization of the hybrid wakefield acceleration scheme. For that, beams with unprecedented qualities were generated with the LWFA process, which were used to drive the PWFA process and accelerate witness beams with gradients exceeding $10\,\mathrm{GeV\,m^{-1}}$ in a proof-of-principle experiment. The witness beams are generated in the LWFA process and (externally) injected into the PWFA stage with capture efficiencies exceeding 50 %.

We furthermore use the hybrid accelerator to pursue fundamental PWFA research. Our shadowgraphic measurements show the formation of an annular plasma ion channel, which was theoretically predicted several years ago and has severe implications on some types of plasma accelerators like AWAKE at CERN. To our knowledge, this is the first experimental demonstration.

With these two milestones, we not only demonstrate the experimental readiness of hybrid wakefield acceleration, but also its potential for future accelerator research.

Contents

I

Introduction

— It is 11pm. Why are we not shooting yet?

This thesis presents a first and major experimental step towards a novel type of particle accelerator concept, called *Hybrid Wakefield Acceleration* [1]. It combines two types of plasma accelerators with the prospect of enabling unique research opportunities towards the next generations of particle colliders and light sources.

In the following, we will discuss the limitations of conventional particle accelerators and the emerging need for novel concepts. We will show that the hybrid wakefield acceleration scheme is a promising candidate to overcome these limits and thereby open new doors in various fields of science.

Motivation

Particle accelerators are used in many fields of research, like high-energy physics, medicine, chemistry and material science, and significantly advanced the fundamental understanding of the universe and matter we have today.

Modern high-energy accelerators are based on radio-frequency (RF) cavities, which means that the particle beams are accelerated by oscillating electromagnetic fields in metallic cavities. This has one major caveat: they suffer from vacuum breakdown [2], which limits their achievable fields and hence acceleration gradients to several tens of $\mathrm{MeV\,m^{-1}}$ [3].

A well known application of RF accelerators is their use in particle colliders for high-energy physics. Some noticeable discoveries are:

- The antiproton in 1955 at the Bevatron with a particle collision energy of 6.2 GeV.
- The muon neutrino in 1962 at the Brookhaven National Laboratory (BNL) with a collision energy of 15 GeV.

- The W and Z bosons in 1983 at the Super Proton Synchrotron at CERN with a collision energy of 400 GeV.
- The Higgs boson in 2012 at the LHC with a collision energy of 14 TeV.

These discoveries show the steady need for higher collision energies. All of these examples were using hadron collisions from storage-ring accelerators where particles are forced onto circular trajectories with magnetic fields. This type of accelerator overcomes the limitation of low acceleration gradients, as the RF cavities are passed through in each revolution of the electron beam. However, the particle energy is now limited by the achievable magnetic fields of the bending magnets that force the beam on the circular trajectory.

A promising alternative to hadron colliders are electron/positron (lepton) colliders, as these are non-composite particles (unlike hadrons), such that the collision events are much cleaner and require less energy. However, storage-ring accelerators become inefficient for electrons and positrons because of the high radiation losses in the bending magnets. Linear accelerators (Linacs), on the other hand, do not suffer from radiation losses, but every RF cavity can accelerate the beam only once. The LHC, being the most powerful collider today, is a superconducting circular accelerator built in an underground tunnel with a circumference of 27 km and a building cost of approximately 4 billion Euro. So far, the Higgs boson is the only major new particle discovery of the LHC in the available energy range up to 14 TeV, and the LHC does not yield enough events with the Higgs boson for high-precision measurements. To further push the boundaries of modern physics, it is likely necessary to reach higher energies than currently available, but conventional RF accelerators approach their limits in terms of size and cost. There are four major propositions for the next generation of colliders, which all (in their first stages) serve as so called *Higgs factories* for high-precision measurements on the Higgs boson.

FCC The Future Circular Collider (FCC) at CERN is a proposed 100 km circumference accelerator that first collides electron-positron pairs with up to 365 GeV center-of-mass energy and later protons with energies of 100 TeV. The estimated cost for both stages will be on the order of 25 billion Euro [4, 5].

CEPC The Electron–Positron Collider (CEPC) in China is another proposed circular collider, which may be upgraded with the Super Proton Proton Collider (SPPC) [6]. It also consists of a 100 km circumference tunnel and yields center-of-mass energies of 240 GeV for the CEPC and up to 150 TeV for the SPPC.

ILC The International Linear Collider (ILC) was originally planned to deliver up to 500 GeV center-of-mass energy in a 34 km long tunnel (and up to 1 TeV with an upgrade) [7], which was later reduced to 250 GeV in a 20 km long tunnel [8] for cost reasons. The overall cost is expected to be around 6 billion Euro [9].

CLIC The Compact Linear Collider (CLIC) is under investigation at CERN. It is a linear electron-positron collider that may be built in three stages with center-of-mass

energies of 380 GeV, 1500 GeV and 3000 GeV and a length of 11 km to 50 km. The estimated cost for the first stage is around 6 to 7 billion Euro, and the cost for each of the two subsequent stages is only slightly lower.

So far, it is not known if any one of these accelerators will ever be built, mainly because of their high costs.

Another major application of accelerators is the field of X-ray imaging. Free-electron lasers (FELs), especially for hard X-rays (XFELs), are arguably considered as the next generation of light sources [10], as they can deliver ultra-short and coherent pulses of radiation with wavelengths down to the angstrom level (see, e. g., [11]). This is done by propagating high-energy electron beams through a magnetic undulator, where, under certain conditions, they undergo a micro-bunching process and radiate synchronously [12]. There are only a few XFEL facilities worldwide, like the European XFEL [11] at Deutsches Elektronen-Synchrotron (DESY), or the Linac Coherent Light Source II (LCLS-II) at the Stanford Linear Accelerator Center (SLAC). All current XFELs use RF accelerators with lengths on the kilometer scale.

A major cost driver of conventional RF accelerators is their size due to the limited accelerating gradient. This makes machines like particle colliders, synchrotrons and FELs expensive and sparse. Especially for large-scale particle colliders, it becomes more and more difficult to reason the expense for fundamental research without apparent foreseeable applications in society. This led to the development of novel accelerator concepts that are trying to overcome the limits of RF accelerators. Arguably, the most promising candidate is plasma acceleration [13, 14], which does not suffer from vacuum breakdown and achieves three orders of magnitude higher acceleration gradients. This might allow building compact and cost-effective FELs [15] and may be the path towards building the next generation of particle colliders [16].

Plasma Acceleration

The concept of plasma acceleration was theoretically proposed by Tajima & Dawson [13] in 1979. In their scheme, a strong laser pulse is propagated through plasma, where it drives a *wakefield* in form of a plasma wave. The strong electrostatic fields of these wakefields allow accelerating charged particle bunches with gradients exceeding the ones of RF accelerators by orders of magnitude. Several years later, Chen *et al.* [14] proposed a slightly different variant using charged particle bunches instead of laser pulses for driving the wakefield. In the following, these laser or particle bunches are referred to as *drivers*, and the accelerated particle bunches as *witnesses*. These schemes are referred to as laser-driven wakefield acceleration (LWFA) and charged particle-driven wakefield acceleration (PWFA), respectively. Although there are several variations of both schemes, here we will focus on LWFA with ultra-short laser pulses and PWFA with ultra-short electron bunches. Note: the term *plasma wakefield acceleration* is often used as a synonym for PWFA in an ambiguous way and should not be mistaken with *plasma acceleration* that represents the general scheme of wakefield acceleration in plasma including LWFA and

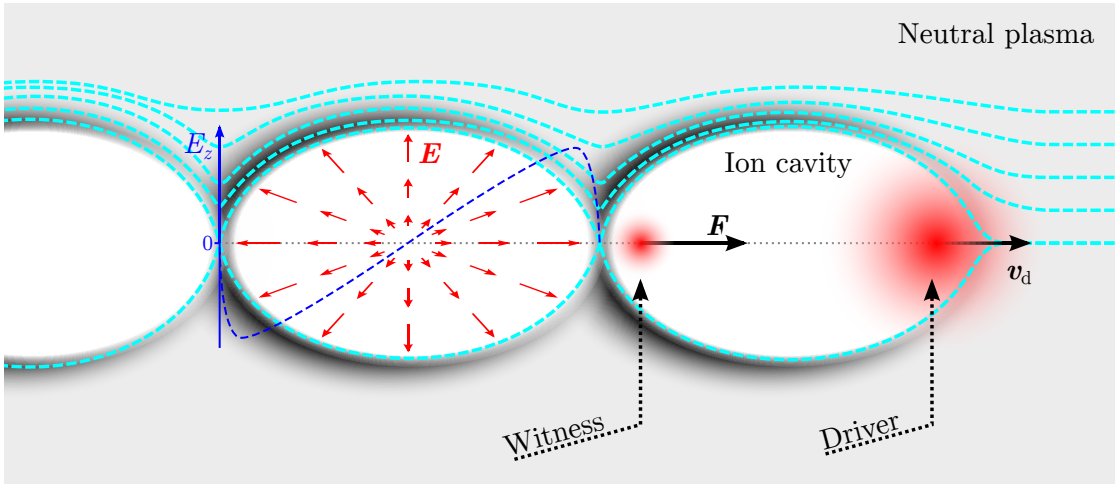

Figure I.1: Sketch of a plasma wakefield. The electron or laser driver is propagating to the right ($v_d \approx c$) through neutral plasma. The plasma electron density is shown by the gray-scale background. The driver pushes the plasma electrons aside, while the ions are much heavier and assumed to be stationary. This leads to an ion cavity forming behind the driver that attracts the electrons back to the driver axis (gray dotted line). The traces of electrons with different initial radii with respect to the driver axis are shown as cyan dashed lines. The ion cavities exhibit almost radial electrostatic fields, as denoted exemplarily in the second cavity by red arrows and the field along the driver axis E_z as the dashed blue graph. This leads to an electron witness bunch in the back of the cavity experiencing accelerating and focusing forces. As the whole structure moves with the driver velocity, which is close to the speed of light, the witness bunch will remain in the accelerating fields for long times.

PWFA.

The basic principle of plasma acceleration is sketched in Figure I.1. The driver propagates through an initially neutral plasma and creates a charge separation by pushing plasma electrons to the side. This happens because both types of drivers have associated radial forces that act repelling to electrons, which is the ponderomotive force for laser pulses and the Coulomb force for electron bunches. For currently available drivers, the ions are too heavy to be significantly influenced (by the driver itself), and they remain almost inert. The expelled electrons are attracted back to the driver axis by the ion background, which leads to a plasma oscillation and correspondingly the formation of a plasma wave. For high driver strengths, the repelling forces can lead to a full blowout of electrons, which forms a cavity consisting only of plasma ions [17], also referred to as *bubble*. It has a length of approximately the plasma wavelength $\lambda_\mathrm{p} \sim \sqrt{n_\mathrm{e}}^{-1}$, where n_e is the plasma electron density. Bubbles contain almost linear electrostatic fields pointing radially from the center to the border [18], and field strengths exceeding tens of gigavolts per meter for typical accelerator parameters. Witness electron bunches placed in the bubble on the opposite side of the driver (as sketched in Figure I.1), will experience accelerating fields in the direction of the driver, as well as focusing fields towards the driver axis. A key feature is that the wave structure moves with a velocity of the driver, which is close to the speed of light, so the witness will co-propagate with the accelerating fields over long distances.

There are different methods of *injecting* a witness bunch into the plasma wave. Most commonly, the witness is created from plasma electrons in the acceleration stage itself, which is referred to as *internal* injection. This can be done, e. g., by distorting the plasma wave with density gradients [19] or auxiliary laser pulses [20], by utilizing ionization mechanics [21, 22], or by letting the plasma wave break [17]. Furthermore, *external* injection of externally generated electron beams can be used, e. g., from RF pre-accelerators [23–26].

Laser-driven wakefield acceleration was the initially proposed type of plasma acceleration by Tajima & Dawson [13], and it required more than two decades of development till the first accelerators delivered quasi-monochromatic electron bunches at energies of 100 MeV [27–29]. Nowadays, LWFA is widely used and studied in many laboratories around the world. Numerous advances lead to e. g. nanocoulomb-scale electron beams with energies up to hundreds of MeV [30, 31], high total energy gains approaching the 10 GeV level [32], and high stability over many hours [33]. The main driver behind this progress is the advancement of laser systems with steadily increasing peak powers [34]. This was significantly driven by the invention of Chirped Pulse Amplification (CPA) by Strickland & Mourou [35] in 1985, which nowadays enables the development of moderate-cost and ultra-high power laser systems. The most common type of lasers used for LWFA are based on amplification in titanium-doped sapphire (Ti:Sa) crystals, also referred to as *Ti:Sa lasers*. State-of-the-art Ti:Sa systems deliver pulse lengths around 30 fs and peak powers exceeding the petawatt level.

When such strong and ultra-short laser pulses propagate through plasma, their oscillating fields lead to a quiver motion of the plasma electrons via the ponderomotive force $\boldsymbol{F}_p = -e^2/(4m\omega^2)\nabla \boldsymbol{E}^2$. This acts as a repulsive force to any kind of charged particle,

especially to electrons with a high charge-to-mass ratio. Noteworthy, the ponderomotive force is orders of magnitude lower than the direct Lorentz force of the electromagnetic wave, as it mostly averages out due to its oscillatory nature. This has several implications on the interaction with plasma, like a strong laser-induced ionization.

One drawback of using laser pulses is that their (group) velocity in plasma is noticeably lower than the vacuum speed of light. It is given by $v_\mathrm{g} = c\sqrt{1-\omega_\mathrm{p}^2/\omega_0^2}$, where ω_0 is the laser frequency and $\omega_\mathrm{p} \sim \sqrt{n_\mathrm{e}}$ the plasma frequency. A typical plasma density of $1 \times 10^{19}\,\mathrm{cm}^{-3}$ results in a plasma wavelength of $\lambda_\mathrm{p} = 10.6\,\mathrm{nm}$ and a group velocity of $v_\mathrm{g} = 0.997c$, which is slightly lower than the speed of light. This results in two problems. Firstly, an accelerated witness electron bunch will become faster than the driver after reaching several MeV and eventually outrun it. For example, an electron bunch with kinetic energy of 100 MeV placed at the back of the bubble will have a velocity of $v_e = 0.99999 > v_g$ and outrun the laser driver within less than 4 mm. This process is called *dephasing*, and it leads to two problems: Firstly, it limits the overall energy gain within a single acceleration stage. Although there are techniques to suppress dephasing, e. g., by using tapered plasma density profiles [36] or superluminal laser pulses [37], they come with further limitations. Secondly, it can lead to plasma electrons becoming trapped in the plasma wave by wavebreaking [17, 38–41]. A criterion for trapping is that the velocity v_e of a plasma electron reaches the phase velocity of the plasma wave $v_\mathrm{ph,pw}$, so $v_\mathrm{e} \gtrsim v_\mathrm{ph,pw} = v_\mathrm{g}$. If the amplitude of the plasma wave becomes high enough, electrons from the background plasma acquire sufficient energy to surpass this threshold and become trapped. This can be more or less controlled and utilized as an injection mechanism, referred to as *self-injection*. However, it can also lead to an unwanted dark current [42].

The PWFA scheme [14], on the other hand, works with relativistic charged particle drivers instead of laser pulses. The radial electrostatic fields in their rest frame transform into quasi-transverse fields $\boldsymbol{E}$ in the lab frame. The Coulomb force acted on the plasma electrons $\boldsymbol{F} = e\boldsymbol{E}$ is thus also mainly transverse. In contrast to a laser driver, a relativistic particle bunch has a velocity very close to the speed of light and the witness bunch does not outrun the driver as much, so dephasing is practically absent. This enables much longer acceleration lengths, such that the total energy gain in a single stage can be significantly increased. So far, energy gains of 42 GeV in a single meter-scale acceleration stage have been reported [45]. The high driver velocity also leads to an increased energy threshold for trapping, so dark currents as well as self-injection are suppressed.

Because of their uni-polar fields, particle drivers require much lower fields to exert a given force on plasma electrons than a laser. This has strong implication on the ionization mechanics, as the driver itself does not necessarily ionize the background gas to high levels as a laser driver does. There are two proposed injection methods that utilize this property to possibly create ultra-low emittance witness beams that are suitable to e. g. drive FELs. These are the Trojan Horse scheme [44] and Wakefield-Induced Ionization Injection (WII) [43, 46], and they both rely on locally ionizing a dopant gas within the plasma wave bubble. Both schemes are sketched in Figure I.2. In the Trojan Horse scheme, a laser pulse is focused collinearly to the electron driver into the center of the

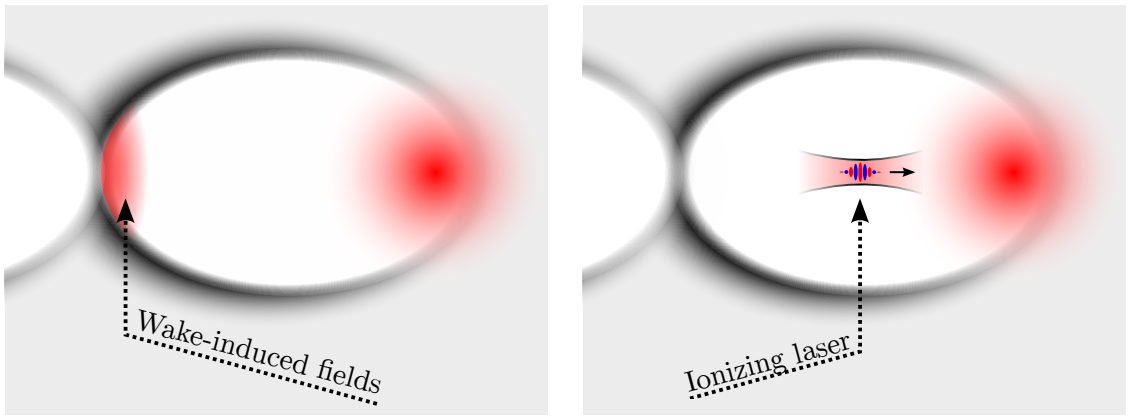

(a) Wakefield-Induced Ionization Injection [43] (b) Trojan Horse injection [44]

Figure I.2: Novel injection schemes for potentially ultra-low emittance beams in PWFA. The Wake-Induced Ionization Injection scheme (a) by Martinez de la Ossa *et al.* [43] ionizes a higher level of the background plasma by the strong fields of the plasma wave in the back of the bubble. The Trojan Horse injection scheme by Hidding *et al.* [44] uses a laser to ionize a higher level in the center of the bubble. These electrons will subsequently fall back to the end of the bubble and get accelerated.

bubble. The power and the Rayleigh length of the laser are adjusted such that it can ionize a dopant gas in a small volume around the focus. The region over which electrons are created can ideally be made very small, which leads to a small transverse spread in momentum and position and hence a small emittance. The electrons will subsequently fall back to the end of the bubble and get accelerated from there on. In the WII scheme, a dopant gas is ionized by the strong accelerating fields of the plasma wave itself. This requires well-defined driver and plasma parameters, such that the fields are within a certain range to ionize only in a small region in the back of the bubble. Additionally, measures must be taken to restrict the injection over a short length, e. g., by limiting the dopant to a small length of the gas target. Furthermore, as the witness bunches reach highly relativistic velocities much faster than in RF accelerators because of the higher acceleration gradients, the emittance growth due to space-charge is strongly reduced.

There are currently only a few PWFA research facilities available worldwide. These include the National User Facility for Advanced Accelerator Experimental Tests II (FACET-II) at SLAC National Accelerator Laboratory [47], FLASHForward at DESY [48], or the AWAKE project at CERN [49, 50] (which works with long proton drivers). All of these use RF accelerators on a kilometer scale to deliver the drive beams. This leads to the research opportunities on Trojan Horse and WII being very limited, and both schemes are yet lacking an experimental demonstration. The Trojan Horse scheme has the additional requirement of a laser that is synchronized on a femtosecond-level to the driver. Even state-of-the-art RF-based PWFA facilities only reach a synchronization of a laser with a jitter of tens of fs (see e. g. [47, 51]). Even without Trojan Horse and WII,

the performance of RF-driven PWFA systems generates beam brightnesses exceeding the ones of conventional RF systems by orders of magnitude (see e. g. [52–54]).

The LWFA and PWFA scheme both promise to reduce the overall accelerator size with high acceleration gradients, but they have their own individual strengths. LWFA allows to build overall compact and inexpensive accelerators with high charge and moderate energy. It also comes with an inherently synchronized laser that can be used for e. g. diagnostics or injection methods. The PWFA scheme, on the other hand, promises the generation of ultra-high quality electron beams that are necessary for hard X-ray FEL systems, and is a promising candidate for building future high-energy colliders. However, they also come with their individual drawbacks, which is the relatively high energy spread and unstable operation of LWFA, and the need for large pre-accelerators and high cost of PWFA. Recently, Wang *et al.* [55] achieved a breakthrough with a proof-of-concept experiment demonstrating lasing of an FEL driven by an LWFA-generated electron beam. They achieved beam qualities with energy spreads of 0.5 %, which is extraordinary for LWFA systems and does not represent the beam qualities achieved at most other LWFA systems. However, even with these high beam qualities, the FEL operation is limited, and the authors state that further improvements of the LWFA-generated electron beams are necessary for actual FEL applications [55]. Here, the PWFA scheme with Trojan Horse or WII may be a solution, but PWFA with RF drivers defeats the promise of a compact FEL. As we will discuss below, a promising solution to this problem is to combine the strengths of LWFA and PWFA.

Creating Synergies: The Hybrid Scheme

The hybrid acceleration scheme [1] combines the advantages of both LWFA and PWFA in a single accelerator. In essence, an LWFA stage is used to create a drive electron bunch for a subsequent PWFA stage. Even though this scheme initially was considered as an energy booster for LWFA machines [1], the prospects of hybrid acceleration go far beyond. Firstly, it allows fundamental PWFA research in abundant, 100 TW-scale laser facilities by lifting the requirement of large-scale RF pre-accelerators that are only available in a handful facilities worldwide. Secondly, it can serve as an energy, brightness and quality transformer [56], where high-quality electron beams created by novel injection mechanisms like Trojan Horse or WII can be accelerated with lower-quality LWFA beams. This enables a plethora of opportunities, like driving FELs with small-scale laser systems instead of large RF accelerators. Thirdly, it allows PWFA with an inherently synchronized laser with femtosecond jitter, which is suitable for advanced diagnostics like few-cycle shadowgraphy [57], optical injection schemes like Trojan Horse [44] or seeding FELs [58].

Although it is obvious that – in theory – LWFA-generated electron beams can drive their own plasma waves and accelerate witness bunches therein, the technical realization proves to be challenging. Realizing LWFA and PWFA accelerators is a non-trivial task on its own and requires a high amount of control and knowledge over the involved parts, like laser systems, plasma targets and diagnostics. Previous experiments already gathered some indirect evidence that it may be feasible to drive a plasma wave with

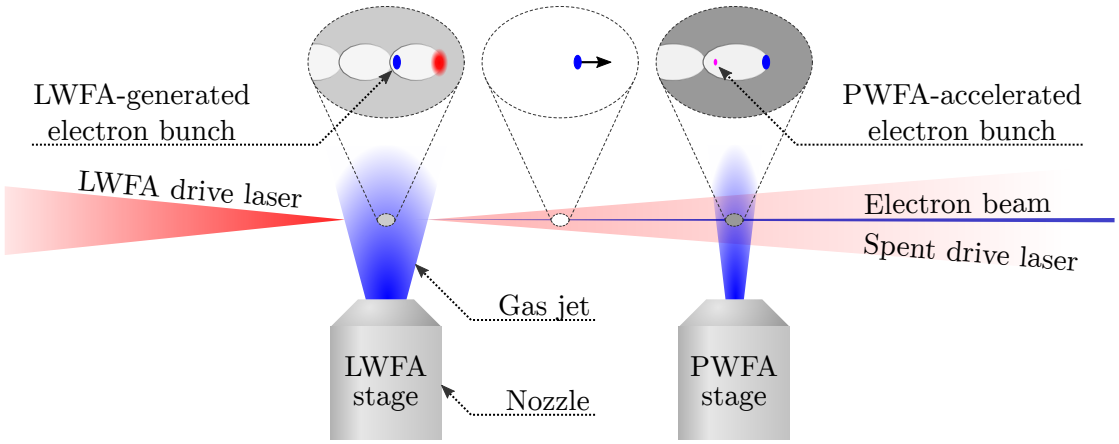

Figure I.3: Scheme of hybrid wakefield acceleration. An electron bunch is generated in an LWFA stage and subsequently used to drive the PWFA in a second stage. There, either externally or internally injected electron (witness) bunches can be accelerated.

LWFA-generated electron beams. Chou *et al.* [59] observed a strong deceleration of LWFA-generated electrons in a subsequent plasma stage, which indicates a collective plasma response and may be explained by the generation of a plasma wave. Heigoldt *et al.* [60] performed measurements of the temporal profile of LWFA-generated electron bunches, where he observed a second bunch appearing at the point where the laser depletes. One possible explanation is that at this point the electron bunch takes over to drive a wakefield, and the second electron bunch is injected when the wakefield falls back from the laser to the first electron bunch. Kuschel *et al.* [61] observed a focusing effect of an LWFA-generated electron bunch in a separate gas target, where the bunch is generating focusing fields by exciting a plasma wave. However, all of these experiments are lacking a clear demonstration of involved plasma waves. After the original proposal, it took many years of technical advances until we were finally able to make a first and major step towards utilizing the full potential of the hybrid scheme. This was mainly limited by the achievable LWFA beam parameters in terms of current and divergence. Improved laser powers and beam qualities, and a thorough optimization of the LWFA target and injection mechanism allowed us to generate unprecedented electron beams with charges on the nanocoulomb level and divergences below 1 mrad FWHM [30, 62]. This laid the basis for studying the hybrid scheme for the very first time.

We reached two major goals with our studies. Firstly, we demonstrated the feasibility of the hybrid scheme with proof-of-principle experiments. In a first step, we proved that LWFA-generated electron bunches can drive strong plasma waves in a separate plasma targets by direct shadowgraphic measurements. In a second step, we demonstrated that these plasma waves can be used to accelerate externally injected witness bunches. Secondly, we demonstrate that the hybrid scheme is a valuable tool for pursuing fundamental PWFA research. With shadowgraphic measurements, we were able to observe and study

an ion channel formation in the PWFA process, which was theoretically predicted [63, 64] for several years and has strong implications, e. g., on large-scale PWFA designs using long drivers like the AWAKE project [29, 49, 65]. To our knowledge, our measurements are the first reported observations of this process. This demonstrates the experimental readiness and the potential of the hybrid wakefield acceleration scheme for future research.

Structure of this Work

This work is structured in four chapters discussing the theoretical and experimental methods, and the observations and results of our studies towards the hybrid wakefield acceleration scheme.

Chapter 1 The first chapter introduces the theoretical concepts that are necessary to understand the plasma acceleration process. This includes laser and plasma physics, and finally the generation of plasma wakefields.

Chapter 2 The second chapter describes the experimental setup and methods of the laser system and the accelerator.

Chapter 3 The third chapter demonstrates the experimental feasibility of hybrid wakefield acceleration. We present three experiments that show main conclusions we drew from first studies towards the first proof-of-principle demonstration.

Chapter 4 The fourth chapter discusses observations and studies of the plasma ion dynamics and their implications on the design of large-scale accelerators as a first demonstration of fundamental PWFA research with the hybrid scheme.

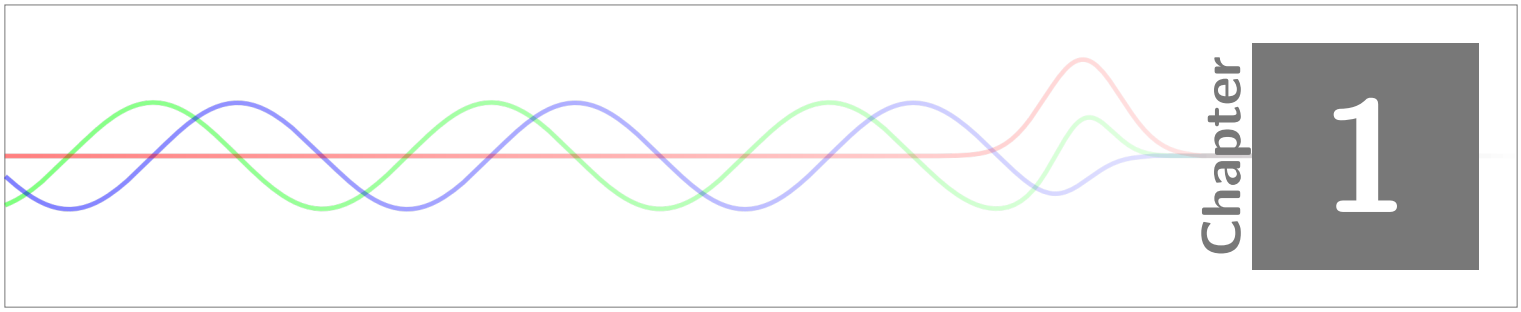

Chapter 1

Theoretical Background

— Can someone remind me how the x scale transforms in an FFT?

This chapter will introduce the underlying theoretical concepts and models of the hybrid acceleration scheme. These are well-known and can be found in many textbooks and review articles on electrodynamics (e. g. [66]), basic plasma physics (e. g. [67]) and laser-plasma interaction (e. g. [68–70].

We will start with the mathematical description of laser pulses and plasma, and how both interact in a very basic way. Afterwards, we discuss laser- and electron-driven wakefields and their limitations.

1.1 Laser Pulses

As laser pulses are electromagnetic waves, they obey Maxwell's equations. In the presence of unbound charges with charge density ρ and current $\boldsymbol{J}$, the microscopic representation can be used [66]

$$\nabla \cdot \boldsymbol{E} = \frac{\rho}{\epsilon_0} \tag{1.1}$$

$$\nabla \cdot \boldsymbol{B} = 0 \tag{1.2}$$

$$\nabla \times \boldsymbol{E} = -\frac{\partial \boldsymbol{B}}{\partial t} \tag{1.3}$$

$$\nabla \times \boldsymbol{B} = \mu_0 \left(\boldsymbol{J} + \epsilon_0 \frac{\partial \boldsymbol{E}}{\partial t} \right) \tag{1.4}$$

where $\boldsymbol{E}$ and $\boldsymbol{B}$ are the electric and magnetic fields, and ϵ_0 and μ_0 are the vacuum permittivity and permeability. These can be simplified by introducing the magnetic

vector potential $\boldsymbol{A}$ and the scalar electric potential ϕ with

$$\boldsymbol{B} = \nabla \times \boldsymbol{A} \tag{1.5}$$

$$\boldsymbol{E} = -\nabla\Phi - \frac{\partial \boldsymbol{A}}{\partial t}. \tag{1.6}$$

and applying the Lorenz gauge $\nabla A = c^{-2}\frac{\partial \Phi}{\partial t}$. Now, the four Maxwell's equations reduce to

$$\Box\Phi = \left(\frac{1}{c^2}\frac{\partial^2}{\partial t^2} - \nabla^2\right)\Phi = \frac{\rho}{\epsilon_0} \tag{1.7}$$

$$\Box\boldsymbol{A} = \left(\frac{1}{c^2}\frac{\partial^2}{\partial t^2} - \nabla^2\right)\boldsymbol{A} = \mu_0\boldsymbol{J} \tag{1.8}$$

with the d'Alembert operator $\Box = \left(\frac{1}{c^2}\frac{\partial^2}{\partial t^2} - \nabla^2\right)$.

In vacuum, the charge density ρ and current $\boldsymbol{J}$ are zero, and solutions for Φ and $\boldsymbol{A}$ are wave equations. Thus,

$$\Phi = 0 \tag{1.9}$$

$$\boldsymbol{A} = -\boldsymbol{A}_0 \sin\left(\omega t - \boldsymbol{k}\boldsymbol{x} + \phi\right) \tag{1.10}$$

are particular solutions, where ϕ is a phase and $\boldsymbol{k}$ is a wave vector with $\boldsymbol{k} \parallel \boldsymbol{A_0}$ and $k = 2\pi/\lambda$. This leads to the electric and magnetic fields

$$\boldsymbol{E} = \omega\boldsymbol{A}_0 \cos\left(\omega t - \boldsymbol{k}\boldsymbol{x} + \phi\right) \tag{1.11}$$

$$\boldsymbol{B} = \boldsymbol{k} \times \boldsymbol{A}_0 \cos\left(\omega t - \boldsymbol{k}\boldsymbol{x} + \phi\right) \tag{1.12}$$

such that the amplitudes become $E_0 = \omega A_0$ and $B_0 = kA_0 = \omega c^{-1} A_0$ with the dispersion relation $c = \omega/k$. This describes a plane electromagnetic wave with wavelength $\lambda = 2\pi/k$ traveling along $\hat{\boldsymbol{k}}$. As Maxwell's equations are linear ordinary differential equations (ODEs), a superposition of different plane waves

$$\boldsymbol{A} = \sum_0^n \boldsymbol{A}_{0,n} \sin\left(\omega_n t - \boldsymbol{k}_n\boldsymbol{x} + \phi_n\right) \quad \text{with} \quad n \in \mathbb{N} \tag{1.13}$$

is also a solution to Maxwell's equations. Some descriptions, like focused laser pulses, require an infinite sum of such plane waves.

We first consider the temporal behavior of a continuum of plane waves with frequencies ω and wave vectors $\boldsymbol{k}$ with $\boldsymbol{k}\boldsymbol{x} = kz = \omega c^{-1} x$ and corresponding amplitude $\tilde{A}_0(\omega)$ and phase $\tilde{\phi}(\omega)$. Then, equation 1.13 can be written in the form

$$A = \int_0^\infty \mathrm{d}\omega \tilde{A}_0(\omega) \sin\left(\omega\tau + \tilde{\phi}(\omega)\right) \tag{1.14}$$

where $\tau = t - z/c$ is a co-moving coordinate. Correspondingly the electromagnetic field becomes

$$E = \frac{1}{2}\left[\int_0^\infty \mathrm{d}\omega \tilde{E}_0(\omega) e^{i\omega\tau + i\tilde{\phi}(\omega)} + \text{c.c.}\right]. \tag{1.15}$$

Here, $E_0(\omega)$ is the spectral amplitude. The integral has the form of a Fourier transformation, such that the spectral amplitude $\tilde{E}_0(\omega)$ and temporal amplitude $E_0(t)$ are the Fourier transformations of each other

$$E_0(\xi) = \frac{1}{\sqrt{2\pi}} \left(\mathcal{F}\tilde{E}_0\right)(\xi). \tag{1.16}$$

This implies that a temporally infinite plane wave has only a single (sigma-function) wavelength, and a temporally limited pulse a spectral amplitude with a certain width. Thus, a short laser pulse consists of a superposition of a wide spectrum of plane waves.

In addition to the temporal and spectral description and behavior of laser pulses, the spatial evolution plays an important role in laser systems and experiments. Often, laser beams can be approximated with a Gaussian transverse profile. Here, we use the convention that the propagation axis is $\boldsymbol{z}$. Assuming a single wavelength λ, spatial amplitude $\boldsymbol{E}_0 = E_0(\rho)\hat{\boldsymbol{n}}$ ($\rho = \sqrt{x^2+y^2}$) and polarization $\hat{\boldsymbol{n}}$ in the xy-plane:

$$\boldsymbol{E}(\rho) = \boldsymbol{E}_0(\rho)e^{i\omega\tau}\hat{\boldsymbol{n}} + \text{c.c.}. \tag{1.17}$$

The amplitude needs to satisfy the Helmholtz equation

$$\nabla_\perp^2 E_0 + 2ik\frac{\partial E_0}{\partial z} = 0 \tag{1.18}$$

where $\nabla_\perp^2 = \partial_x^2 + \partial_y^2$ is the transverse Laplace operator. This leads to the solution

$$\boldsymbol{E}_{\text{Gauss}}(\rho,t) = \hat{\boldsymbol{n}}\frac{E_0}{2}\frac{w_0}{w(z)}e^{-\frac{\rho^2}{w^2(z)}}e^{ik\frac{\rho^2}{2R(z)}-i\zeta(z)}e^{i\omega\tau} + \text{c.c.} \tag{1.19}$$

where $\rho^2 = x^2+y^2$ and the beam parameters

$$w_0 = \sqrt{\frac{\lambda z_R}{\pi}} \tag{1.20}$$

$$w(z) = w_0\sqrt{1+\left(\frac{z}{z_R}\right)^2} \tag{1.21}$$

$$R(z) = z\left(1+\left(\frac{z_R}{z}\right)^2\right) \tag{1.22}$$

$$\zeta(z) = \arctan\frac{z}{z_R} \tag{1.23}$$

are used. The typical shape of a Gaussian beam is sketched in figure 1.1. At each longitudinal position z, the radius at which the amplitude drops to $1/e$ of the maximum in the center is given by $w(z)$. At $z=0$, the radius has a minimum $w(z=0) = w0$, which is referred to as *waist* or *focus*. The parameter z_R is called Rayleigh length and defines the length over which the peak intensity drops to $1/2$. When moving one Rayleigh length from the waist, the size of the beam increases by a factor of $\sqrt{2}$ to $w(z_\text{R}) = \sqrt{2}w_0$, and the amplitude at $r=0$ decreases by a factor of 2. Far away from the waist ($z/z_\text{R} \gg 1$), the

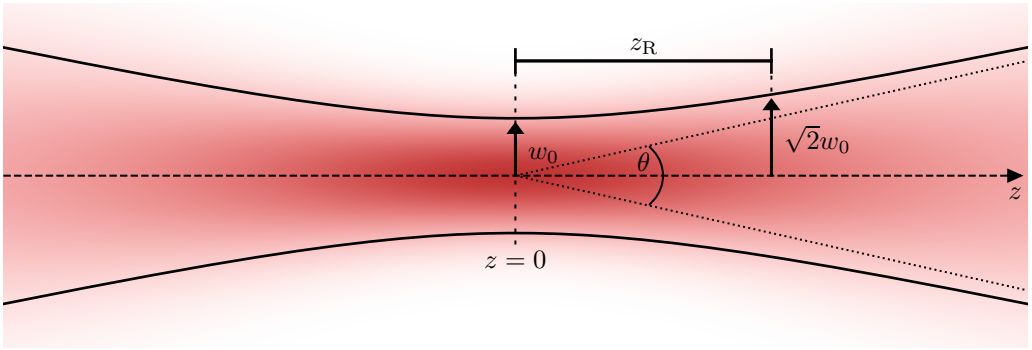

Figure 1.1: Propagation of a Gaussian beam. At the waist, the transverse size of the envelope of the electric field is w_0. In a distance of one Rayleigh length z_R the beam size has increased to $w(z_R) = \sqrt{2}w_0$.

width increases and the amplitude drops almost linearly, and the size increases linearly with an opening angle or *divergence* of $\theta = 2w_0/z_\mathrm{R}$.

Three useful parameters of laser beams are the pulse energy, peak power and peak intensity. The intensity is defined as

$$I = \epsilon_0 c \left\langle E^2 \right\rangle_t = \frac{\epsilon_0 c}{2} E_0^2 \tag{1.24}$$

where $\langle E^2 \rangle_t$ is the average over a single oscillation period. The intensity is thereby the (areal) power density, as it is the energy contained in the electromagnetic fields divided by its duration and transverse size. In laser physics it is customary to express the intensity in the unit $\mathrm{W\,cm^{-2}}$. The laser power is defined by the integration of the intensity over the spatial domain

$$P = \iint I \,\mathrm{d}x\,\mathrm{d}y \tag{1.25}$$

and the pulse energy is the integration over the spatial and temporal domain

$$E = \iiint I \,\mathrm{d}x\,\mathrm{d}y\,\mathrm{d}t \tag{1.26}$$

For a Gaussian pulse with $E_0 = \tilde{E}_0 \exp(-t^2/\sigma_t^2 - \rho^2/w_0^2)$, the intensity becomes

$$I = I_0 \exp\left(-2\frac{t^2}{\sigma_t^2} - 2\frac{\rho^2}{w_0^2}\right) = I_0 \exp\left(-\frac{t^2}{2\sigma_{t,I}^2} - \frac{\rho^2}{2\sigma_{\rho,I}^2}\right) \tag{1.27}$$

with the amplitude

$$I_0 = \frac{\epsilon c}{2} \tilde{E}_0^2 \tag{1.28}$$

and the pulse width $\sigma_{\rho,I} = w_0/2$ and length $\sigma_{t,I} = \sigma_t/2$. The full-width-half-maximum (FWHM) width is given by

$$\sigma_{\mathrm{FWHM},I} = 2\sqrt{2\ln(2)}\sigma_{\rho,I} = \sqrt{2\ln(2)}w_0 \approx 1.18 w_0 \tag{1.29}$$

1.2 Electron Motion in Laser Fields

In the last part, we considered the beam propagation in vacuum where the charge ρ and the current $\boldsymbol{J}$ are zero. This is obviously not valid when we consider the interaction of laser pulses with plasma. There, the density ρ and current $\boldsymbol{J}$ are influenced by the electric and magnetic fields $\boldsymbol{E}$ and $\boldsymbol{B}$, which are in turn influenced by ρ and $\boldsymbol{J}$. This coupling makes it difficult to find solutions for the evolution of a system, and usually numerical methods are required for realistic scenarios.

In the following discussions, we will consider the interaction of laser pulses with a single charged particle. We will simplify the model by assuming that the feedback from the electron on the electromagnetic fields is negligible, such that the laser will not be perturbed by the particle. For that, we will set ρ and $\boldsymbol{J}$ in Maxwell's equations to zero.

Firstly, we will look at the behavior of a single particle in the presence of a plane electromagnetic wave. The second part will then show that a spatially limited laser beam will deflect charged particles via the so-called *ponderomotive force*, which is fundamental for the process of wakefield generation.

The force that is acted on charged particles from electromagnetic fields is the Lorentz force

$$\boldsymbol{F} = q\left(\boldsymbol{E} + \boldsymbol{v} \times \boldsymbol{B}\right), \tag{1.30}$$

where $\boldsymbol{v}$ and q are the velocity and charge of the particle, and $\boldsymbol{E}$ and $\boldsymbol{B}$ the fields at the particle's position. The Lorentz force along with Maxwell's equations can be used to describe most of the laser-plasma interaction on a low level. In vacuum and our simplified case of single particles ($\rho = 0$ and $\boldsymbol{J} = 0$), the vector potential allows to simplify the Lorentz force to

$$\boldsymbol{F} = q\left(-\frac{\partial \boldsymbol{A}}{\partial t} + \boldsymbol{v} \times \nabla \times \boldsymbol{A}\right). \tag{1.31}$$

For the interaction with particles, it is helpful to introduce the (dimensionless) *normalized vector potential* $\boldsymbol{a} = e\boldsymbol{A}/m_\mathrm{e}c$ and corresponding amplitude $a_0 = eA_0/m_\mathrm{e}c$. With this, the Lorentz force can be rewritten as

$$\frac{\boldsymbol{F}}{m_\mathrm{e}c} = \frac{q}{e}\left(-\frac{\partial \boldsymbol{a}}{\partial t} + \boldsymbol{v} \times \nabla \times \boldsymbol{a}\right). \tag{1.32}$$

Consider first a plane electromagnetic wave in vacuum with a vector potential

$$\boldsymbol{A}(z,t) = A_0 \cos\left(i\omega\tau\right)\boldsymbol{e}_x. \tag{1.33}$$

Finding the solution of the equation of motion of an electron with charge $q = e$ is lengthy, and the result is [68]

$$x(\tau) = \frac{ca_0}{\omega}\sin\left(\omega\tau\right) \tag{1.34}$$

$$y(\tau) = 0 \tag{1.35}$$

$$z(\tau) = \frac{ca_0^2}{4}\left[\tau + \frac{1}{2\omega}\sin\left(2\omega\tau\right)\right]. \tag{1.36}$$

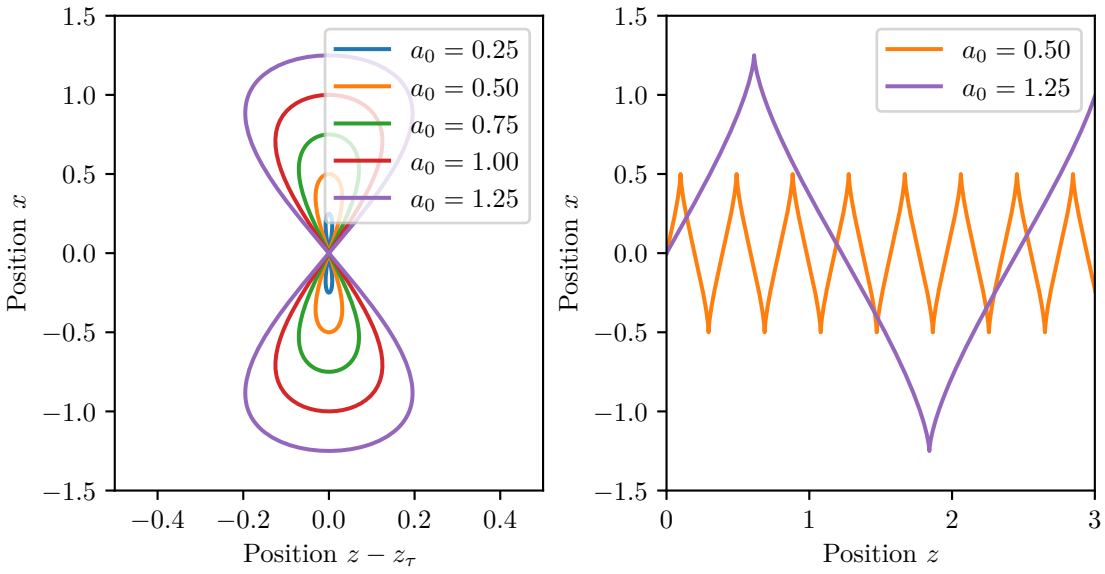

Figure 1.2: Motion of a particle in a plane electromagnetic wave for different amplitudes a_0. The left side shows the *figure 8 motion* in a co-moving frame, the right side shows the motion in the laboratory frame. For higher a_0, the longitudinal motion becomes more and more dominant.

This motion consists of two parts. Firstly, there is a constant drift along z, which is given by

$$z_d(t) = \frac{ca_0^2}{4}\tau = \frac{ca_0^2}{4}(t - z_d(t)/c) \tag{1.37}$$

$$\Rightarrow z_d(t) = \frac{a_0^2}{4 + a_0^2}t \tag{1.38}$$

The second part of z is an oscillation with the second harmonic (2ω) of the electromagnetic wave. This is shown in Figure 1.2 It can be shown that the electron velocity becomes relativistic when a_0 approaches unity.

If one considers a temporally limited pulse in 1D, one can show that the momentum after the pulse has passed is the same as before, so no net energy gain from the fields to the particle happens [68].

For laser beams with a non-infinite transverse size, the motion of a charged particle is different from the pure figure-8 motion and drift in a plane wave. As we will show, charged particles are repelled from regions with high field amplitude. Consider a particle in the center of a temporally infinite Gaussian beam. The particle will begin to oscillate in transverse direction, and thus move towards decreasing field amplitudes. The fields that accelerate it back towards the center will then be lower, and the particle eventually drifts away from the center. Generally, this drift will happen from regions of high amplitude to regions of low amplitude. This process can be described by a force exerted by the laser, which is called *ponderomotive force*.

Here, we will assume low field amplitudes $a \ll 1$, which also leads to particle velocities $v \ll c$, such that the magnetic term of the Lorentz force can be neglected. We will further assume a beam with an arbitrary transverse profile $a_0(\boldsymbol{r})$ and transverse polarization $\tilde{\boldsymbol{n}}$

$$\boldsymbol{a}(\boldsymbol{r}, t) = a_0(r) \exp^{i(\omega t - \boldsymbol{k}\boldsymbol{r})} \hat{\boldsymbol{n}} + \text{c.c.} \tag{1.39}$$

Consider a charged particle, initially located at a position $\boldsymbol{r}_0$ with vector potential $a_0(\boldsymbol{r}_0)$. When the particle oscillates, it will experience slightly varying fields that can be approximated by a Taylor expansion. We will therefore expand the vector potential around r_0

$$a_0(\boldsymbol{r}) \approx a_0(\boldsymbol{r})|_{\boldsymbol{r}=\boldsymbol{r}_0} + \nabla a_0(\boldsymbol{r})|_{\boldsymbol{r}=\boldsymbol{r}_0} \boldsymbol{r} + \cdots \tag{1.40}$$

The 0_{th} order will result in an oscillation, while the 1^{th} order will lead to a drift. This drift can be associated with a ponderomotive force $\boldsymbol{F}_{\text{p}}$ given by [68]

$$\boldsymbol{F}_{\text{p}} = -\frac{q^2}{4m_{\text{e}}\omega^2} \nabla E^2 \tag{1.41}$$

or in terms of the vector potential

$$\boldsymbol{F}_{\text{p}} = -\frac{q^2}{4e^2} m_{\text{e}} c^2 \nabla a^2 \tag{1.42}$$

where q is the particle charge. The ponderomotive force is thus directed towards decreasing field amplitudes for both positively and negatively charged particles.

Thus, when a tightly focused laser pulse propagates through plasma, it pushes charged particles out of its way. For a typical plasma consisting of electrons and protons, the difference in mass leads to a difference in acceleration, such that the laser will generate a charge separation, as it pushes the electrons further than the protons. This will give rise to the generation of wakefields, as discussed later.

1.3 Basic Plasma Properties

The intensities we reach in our experiments are usually exceeding $1 \times 10^{18}\,\text{W}\,\text{cm}^{-2}$. As a comparison, an intensity of $3.5 \times 10^{16}\,\text{W}\,\text{cm}^{-2}$ corresponds to fields exceeding the binding fields between the electron and proton of a hydrogen atom, so the laser pulse almost instantly ionizes hydrogen or outer shell electrons even in a wide area around its peak [71]. This process is called barrier suppression ionization (BSI). The laser is able to ionize even further from the peak intensity via tunnel ionization and multi-photon ionization. Usually, intensities above $1 \times 10^{14}\,\text{W}\,\text{cm}^{-2}$ are sufficient to ionize hydrogen with these processes [70]. In our experiments, the laser pulse is focused into hydrogen gas, and we can consider it being fully ionized and act as a plasma of electrons and protons at the time the peak of the laser pulse arrives.

In contrast to the single particle treatment from the last section, the electromagnetic fields created by the plasma cannot be neglected here. This leads to a collective behavior, as they respond not only to the laser fields, but also to their own fields.

As the plasma is created from gas, there is an overall equal number of charges, even though there may be imbalances locally. The plasma is therefore called *quasi neutral*. The plasma particles are generally charged, and thus respond to electromagnetic fields. If the plasma is locally perturbed, e. g., by adding an external test charge, the positively and negatively charged plasma particles will reposition, such that the external charge is shielded and decays exponentially with distance. This process is called Debye-shielding, and the length over which the electrostatic potential of the test charge decays by $1/e$ is called Debye length λ_D. It is given by

$$\lambda_\mathrm{D} = \sqrt{\frac{\epsilon_0 k_\mathrm{B} T}{n_\mathrm{e} e^2}}, \tag{1.43}$$

where ϵ_0 is the vacuum permittivity, k_B the Boltzmann constant and T the temperature.

Another important property of plasma is that a perturbation leads to a particle oscillation. This can easily be explained with Dawson's sheet model [72], which will be described in the following. Consider an initially neutral plasma with particle density n_p and static (immobile) ions in 1D. Assume further that electrons are slightly moved in a collective way, such that they do not cross each other. An electron with initial equilibrium position x_0, which is moved by a distance Δx to $x = x_0 + \Delta x$, crosses over a length of ions corresponding to a charge of $e n_\mathrm{p} \Delta x$. As electrons do not cross each other, for the electron at x, there is an excess of electrons with a charge of $e n_\mathrm{p} \Delta x$ on one side, and an excess of ions with the same charge on the other side. With Gauss's theorem, this leads to a field $E = 4\pi n_\mathrm{p} e \Delta x$ and a corresponding force

$$F = -\frac{n_\mathrm{p} e^2}{\epsilon_0} \Delta x \tag{1.44}$$

which has the form of a harmonic oscillator $F = -k\Delta x$. Its frequency ω_p is given by

$$\omega_\mathrm{p} = \sqrt{\frac{k}{m_\mathrm{e}}} = \sqrt{\frac{e^2 n_0}{m_\mathrm{e} \epsilon_0}} \tag{1.45}$$

which is the cold plasma frequency. So, if electrons are moved from their equilibrium position, they start oscillating with the plasma frequency ω_p.

The shielding and oscillation of plasma particles changes the propagation of electromagnetic waves. In a cold plasma, this is governed by the dispersion relation [69]

$$\omega_0^2 = \omega_\mathrm{p}^2 + c^2 k_L^2, \tag{1.46}$$

where ω_L is the laser frequency. Firstly, there is no real solution for the wave number k when $\omega_p > \omega_0$. This means that electromagnetic waves with frequencies below the plasma frequency cannot propagate and are shielded by the plasma. On the other hand, for electromagnetic waves with $\omega_0 > \omega_p$, solutions exist for k and the wave can propagate. This propagation is described by the phase and group velocities v_ph and v_g by

$$v_\mathrm{ph} = \frac{\omega_\mathrm{L}}{k} = \frac{c}{\eta} \tag{1.47}$$

$$v_\mathrm{g} = \frac{\partial \omega_\mathrm{L}}{\partial k} = \eta c \tag{1.48}$$

with the plasma's refractive index

$$\eta = \sqrt{1 - \frac{\omega_\mathrm{p}^2}{\omega_\mathrm{L}^2}} = \sqrt{1 - \frac{n_\mathrm{p}}{n_\mathrm{cr}}} \tag{1.49}$$

where $n_\mathrm{cr} = \epsilon_0 m_\mathrm{e} e^{-2} \omega_L^2$ is the critical density above which an electromagnetic wave with frequency ω_L cannot propagate. The refractive index is lower or equal to unity, or imaginary. The group and phase velocities of an electromagnetic waves with $\omega_\mathrm{L} > \omega_\mathrm{p}$ are thus below and above the speed of light, respectively.

1.4 Wakefield Generation

As discussed previously, the ponderomotive force of a laser pulse deflects electrons from its center, which also happens when an electron bunch propagates through plasma via its Coulomb force. This creates a local charge separation and a corresponding restoring force. When the laser pulse or particle bunch has passed, the plasma electrons will begin to oscillate around their equilibrium positions. In a 1D case, two electrons with a distance $\Delta x = x_2 - x_1$ will have the same oscillation period and amplitude, but a phase difference of $\Delta\phi_x = -\omega_\mathrm{p}\Delta x / v_\mathrm{g}$, where v_g is the velocity of the particle driver or group velocity of the laser. This results in a linear dependence on the phase $\phi_x(x) = -\omega_\mathrm{p} x / v_\mathrm{g}$ with the position x. The total phase of the electron oscillation is therefore $\phi = \omega_\mathrm{p} t + \phi_x(x) = \omega_\mathrm{p} t + \omega_\mathrm{p} x / v_\mathrm{g}$, and can thus be described by a electron wave with $k_\mathrm{p} = \omega_\mathrm{p} / v_\mathrm{g}$ and corresponding phase velocity $v_\mathrm{p,ph} = \omega_\mathrm{p} / k_\mathrm{p} = v_\mathrm{g}$, which is equal to the group velocity of the driver. This plasma wave is referred to as a *wakefield*.

Under some conditions the density perturbation of a plasma in the presence of a laser pulse or particle bunch can be solved analytically. For that, a system of differential equations consisting of the Continuity equation, the Poisson equation, and the equation of motion of the electrons need to be solved.

In order to calculate the density perturbation δn of a plasma for a weak and non-evolving laser or particle driver ($a_\mathrm{L} \ll 1$ and $n_\mathrm{b} \ll n_\mathrm{p}$), a set of three closed differential equations need to be fulfilled. Firstly, the continuity equation

$$\frac{\partial \delta n}{\partial t} + n_\mathrm{p} \nabla \boldsymbol{v} = 0 \tag{1.50}$$

requires that no charge is created or removed. The second equation is the equation of motion of the plasma electrons

$$\frac{\partial \boldsymbol{p}}{\partial t} = \boldsymbol{F}_E + \boldsymbol{F}_\mathrm{pond} = -e\boldsymbol{E} + \frac{m_\mathrm{e} c^2}{4} \nabla \boldsymbol{a}^2, \tag{1.51}$$

which is the combination of the ponderomotive force and the Coulomb force from either plasma or particle beam charges

$$\nabla \boldsymbol{E} = -\frac{e}{\epsilon_o} \left(\Delta n - n_\mathrm{b} \right). \tag{1.52}$$

These three equations can be used to get a single wave equation for the density perturbation δn [14, 73]

$$\left(\frac{\partial^2}{\partial t^2} + \omega_\mathrm{p}\right)\frac{\delta n}{n_\mathrm{p}} = \frac{c^2}{4}\nabla^2 \boldsymbol{a}^2 - \omega_\mathrm{p}^2\frac{n_\mathrm{b}}{n_\mathrm{p}}. \tag{1.53}$$

Here, the first term on the right side is the contribution of an electron driver and the second term the contribution of a laser driver. In a co-moving longitudinal coordinate with $\xi = z - ct$, the derivatives become $\partial_t = c^{-1}\partial_\xi$ and $\nabla = \partial_\perp + \partial_z = \partial_\perp + \partial_\xi$, such that [74]

$$\left(c^2\frac{\partial^2}{\partial \xi^2} + \omega_\mathrm{p}\right)\frac{\delta n}{n_\mathrm{p}} = \frac{c^2}{4}\left(\nabla_\perp^2 + \nabla_\xi^2\right)\boldsymbol{a}^2 - \omega_\mathrm{p}^2\frac{n_\mathrm{b}}{n_\mathrm{p}}. \tag{1.54}$$

$$\left(c^2\nabla_\perp^2 + \omega_\mathrm{p}^2\right)\frac{E_z}{E_0} = c\omega_\mathrm{p}\left(\frac{\boldsymbol{a}^2}{2} - \frac{\delta n}{n_\mathrm{p}}\right) \tag{1.55}$$

This can be integrated to [74]

$$\frac{\delta n}{n_0} = \frac{\omega_\mathrm{p}}{c}\int_0^\xi \mathrm{d}\xi' \sin\left(\frac{\omega_\mathrm{p}}{c}(\xi - \xi')\right)\left[\left(\nabla_\perp^2 + \frac{\partial^2}{\partial \xi'^2}\right)\frac{a^2}{4} + \frac{n_\mathrm{b}}{n_\mathrm{p}}\right]. \tag{1.56}$$

The integration of the longitudinal electric field for the case of only a laser driver ($n_\mathrm{b} = 0$) yields [74]

$$\frac{E_z}{E_0} = \frac{\omega_\mathrm{p}}{c}\int_0^\xi \mathrm{d}\xi' \sin\left(\frac{\omega_\mathrm{p}}{c}(\xi - \xi')\right)\frac{\partial}{\partial \xi'}\frac{a^2}{4}. \tag{1.57}$$

For a Gaussian particle driver, the calculation becomes more complex and involves Bessel functions I_0 and K_0. It can be shown, that the electric field is [74]

$$\frac{E_z}{E_0} = k_\mathrm{p}^3\int_0^\xi \mathrm{d}\xi' \int_0^\infty \mathrm{d}r'\, r' \cos\left(k_\mathrm{p}(\xi - \xi')\right) I_0(k_\mathrm{p} r_<) K_0(k_\mathrm{p} r_>)\frac{n_\mathrm{b}(r', \xi')}{n_\mathrm{p}} \tag{1.58}$$

where $r_<$ ($r_>$) is the smaller (larger) of r and r'.

In such a linear case, the transverse electric field E_r and azimuthal magnetic field B_θ are related to E_z according to the Panofsky-Wenzel theorem [70, 75] by

$$\frac{\partial E_z}{\partial r} = \frac{\partial\left(E_r - B_\theta\right)}{\partial\left(z - ct\right)}. \tag{1.59}$$

The assumption of linear wakefields does usually not hold for the experiments presented in this thesis. In this case, a solution for the plasma perturbation can only be found in the case of a non-evolving driver and in 1D.

The Poisson equation for the normalized vector potential $\phi = e\Phi/m_\mathrm{e}c^2$ is [70, 76–78]

$$\frac{1}{k_p^2}\frac{\partial^2\phi}{\partial \xi^2} = \gamma_p^2\left\{\beta_p\left[1 - \frac{\gamma_\perp^2}{\gamma_p^2\left(1 + \phi\right)^2}\right]^{-1/2} - 1\right\} + \frac{n_\mathrm{b}}{n_\mathrm{p}} \tag{1.60}$$

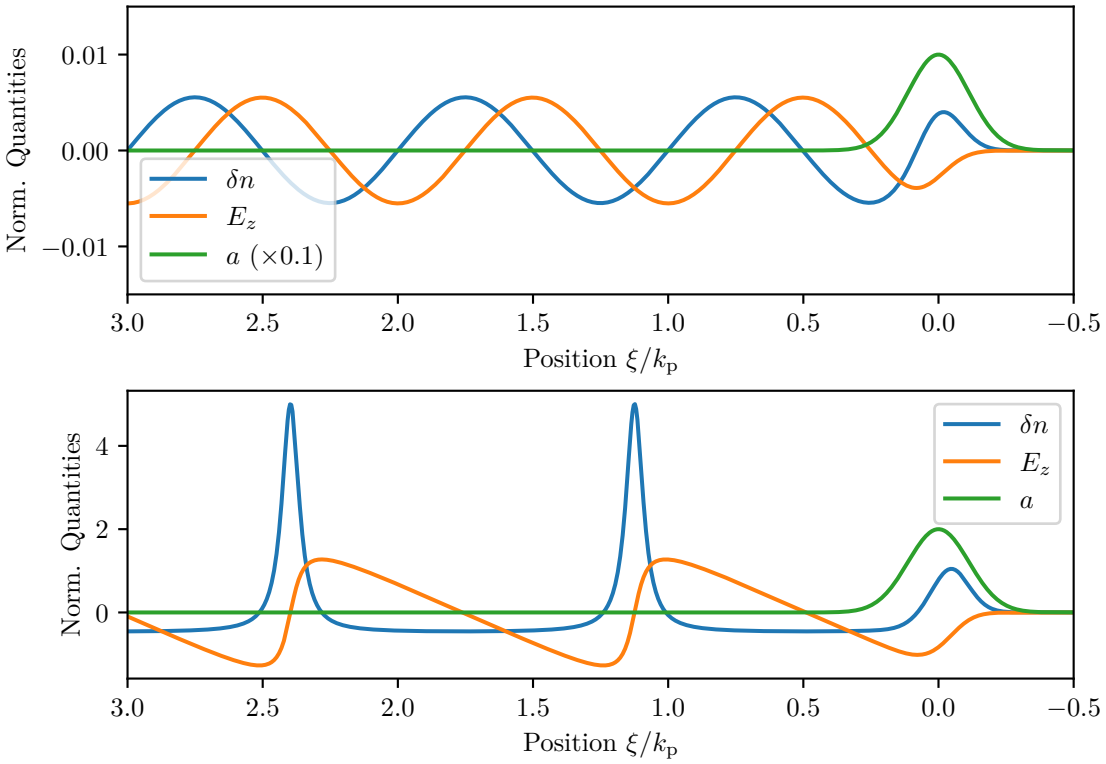

Figure 1.3: Solutions of the density perturbation δn, and the electric field E_z for a laser driver with the vector potential a. In the upper plot, the peak vector potential is $a_0 = 0.1$ and the corresponding wakefield is linear. In the lower plot, the vector potential is $a_0 = 2$, which leads to a non-linear wakefield with sharp density peaks and slightly elongated wavelength.

where $\gamma_\perp^2 = 1 + a^2$, $\beta = v/c$ and the gamma factor $\gamma_\mathrm{p}^2 = \omega_0^2/\omega_p^2$ corresponding to the phase velocity of the plasma wave. For highly under-dense plasma with $\gamma_\mathrm{p}^2 \gg 1$, this simplifies to

$$\frac{1}{k_p^2}\frac{\partial^2\phi}{\partial\xi^2} = \left[\frac{1+a^2}{2(1+\phi)^2} - \frac{1}{2}\right] + \frac{n_\mathrm{b}}{n_\mathrm{p}}. \tag{1.61}$$

which usually requires a numerical treatment. The vector potential can then be used to calculate the density and longitudinal electric field

$$\frac{n}{n_0} = \frac{\gamma_\perp^2 + (1+\phi)^2}{2\,(1+\phi)^2} \tag{1.62}$$

$$\frac{E_z}{E_0} = -c\frac{\partial\phi}{\partial\xi}. \tag{1.63}$$

Solutions for linear and nonlinear wakefields are shown in Figure 1.3

1.5 Acceleration Limits

There are mainly three limits of the achievable energy gain in a plasma stage. Firstly, the diffraction of a laser or divergence of a particle driver. This leads to an increase in size according to

$$w(z) = w_0\sqrt{1+\frac{z^2}{z_\mathrm{R}^2}} \tag{1.64}$$

$$\sigma_r(z) = \sigma_{r_0}\sqrt{1+\frac{z^2}{\beta_0^2}}. \tag{1.65}$$

around their focus (at $z = 0$), which leads to a decrease in peak vector potential a and density n_b and correspondingly a decrease in drive strength. The beta function for drivers used in PWFA is typically at least one order of magnitude higher than the Rayleigh length of LWFA drive lasers, such that particle drivers stay confined much longer [56].

However, in both cases, if the driver is sufficiently strong, it will experience a focusing in the plasma and the length of acceleration can be increased significantly. If a laser pulse exceeds a certain threshold power it undergoes relativistic self-guiding and overcomes diffraction, which is [79]

$$W_\mathrm{cr} \gtrsim 17.4\left(\frac{\omega_0}{\omega_p}\right)^2 \mathrm{GW}. \tag{1.66}$$

Above this threshold, the laser will stay confined over long distances. With typically $\lambda_\mathrm{L} = 800\,\mathrm{nm}$ and plasma densities of $1\times10^{18}\,\mathrm{cm}^{-3}$, the threshold power W_cr is on the order of 10 TW. Furthermore, both types of driver undergo self-channeling [80], which comes from the focusing effect of the induced plasma wave.

The second limiting process is that the accelerated witness bunch may have a higher velocity than the driver and outrun it. This is mostly a problem for laser drivers, as they propagate with the group velocity $v/c = \sqrt{1-(\omega_\mathrm{p}\omega_0)}$, which is typically around 0.997 and thus less than a witness bunch after a moderate acceleration of few tens of MeV. Thus, eventually the witness will overtake the laser and propagate into the front half of the bubble with decelerating fields. The length over which this takes place is called *dephasing length* L_d. In a 1D case, it is given by [81]

$$L_d = \frac{\lambda_p^3}{2\lambda_0^2}\cdot\begin{cases} 1 & \text{for} \quad a_0^2 \ll 1 \\ \dfrac{\sqrt{2}}{\pi}a_0 & \text{for} \quad a_0^2 \gg 1 \end{cases} \tag{1.67}$$

For electron drivers that usually have velocities much closer to the speed of light, the dephasing length is usually not a limiting factor.

The third limitation is the energy loss of the driver. The length over which the it lost

half of its energy is called *depletion length* L_{dp}. For a laser driver, one can find [82]

$$L_{dp,l} = \frac{\lambda_p^3}{\lambda_0^2} \cdot \begin{cases} \dfrac{2}{a_0^2} & \text{for} \quad a_0^2 \ll 1 \\ \dfrac{\sqrt{2}}{\pi} a_0 & \text{for} \quad a_0^2 \gg 1 \end{cases} \tag{1.68}$$

For the regime $a_0 \sim 1$ the depletion and dephasing lengths are similar $L_d \approx L_{dp}$[70]. For a point-like particle driver, the depletion length is [83]

$$L_{\mathrm{dp,b}} = \frac{E_{\mathrm{b}}}{N_{\mathrm{b}} e^2 W} \tag{1.69}$$

where E_{b} and N_{b} are the driver energy and number of particles, respectively. The factor W is the wake amplitude per charge. This leads to the maximum energy gain [83, 84]

$$R = \Delta E_{\mathrm{w}} \leq E_{\mathrm{b}} \left(2 - \frac{N_{\mathrm{w}}}{N_{\mathrm{b}}}\right) \tag{1.70}$$

which is maximum for $N_{\mathrm{w}} = 0$ (i. e., with zero particles in the witness), where the energy gain can be up to twice the particle energy of the driver. For drivers with asymmetric density profiles the maximum energy gain can be higher [83, 85, 86].

All of these limits only hold for a single plasma acceleration stage. In principle, a witness bunch can be accelerated in multiple stages. However, this approach adds further challenges like the electron beam transport between the acceleration stages and the in-coupling of fresh drivers. Apart from the promise of higher beam qualities, the hybrid acceleration scheme may also overcome the limits of LWFA [1] to some extent.

1.6 Summary

Plasma is able to shield charge perturbations by displacing electrons and ions. On short timescales, a charge perturbation leads to an oscillation of plasma particles with the plasma frequency $\omega_{\mathrm{p}} = \sqrt{e^2 n_0 / m_{\mathrm{e}} \epsilon_0}$. Laser pulses and relativistic electron bunches can create such a charge separation and subsequent plasma oscillation with their ponderomotive and space-charge force. As these are moving, the spatial dependence of the oscillation phase manifests itself in a plasma wave. The phase velocity of this plasma wave is equal to the (group) velocity of the driver, which is in both cases close to the speed of light. Certain regions of the plasma wave have electric fields that act focusing as well as accelerating (in the direction of the driver) for electrons. As an accelerated electron as well as the plasma wave structure itself moves with a velocity close to the speed of light, the accelerated electrons can stay in the accelerating and focusing region of the plasma wave for as long as the driver can sustain it. This is limited mostly by three processes: diffraction, dephasing and depletion. While LWFAs practically suffer from dephasing and, to a lesser extent, diffraction, the driver depletion is the ultimate limit for both an LWFA and PWFA stage. The hybrid scheme may be used to overcome the LWFA limits to some extent, although the promise of higher beam qualities is more important for near-term applications.

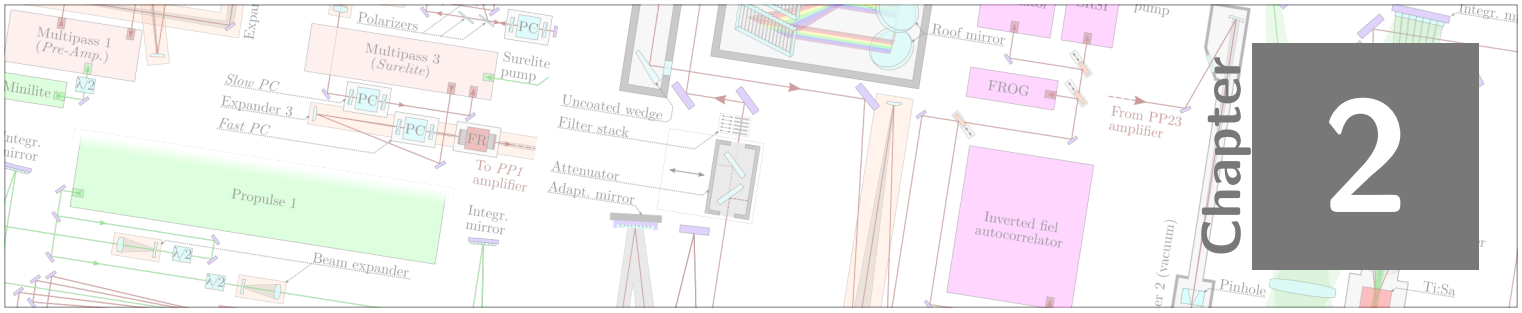

Experimental Setup

— Where did I put the 3 mm screwdriver again?

Hybrid plasma wakefield acceleration requires two general components: a powerful laser system that delivers the necessary energy for the acceleration process, and the accelerator itself. The experiments in this thesis were performed at the Laboratory for Extreme Photonics (LEX) at the Ludwig-Maximilians-Universität in Garching, Germany, which hosted the Advanced Titan:Sapphire Laser System *ATLAS 300*. The ATLAS 300 delivered laser pulses with femtosecond duration and peak powers on a 100 TW-scale. These pulses not only provided the energy to drive the plasma accelerator, but also optical diagnostics and other optical accelerator components. The second major component is the accelerator. It consists of two plasma wakefield acceleration stages, the first of which is driven by the ATLAS 300, and the second one by the laser-accelerated electron beam. Figure 2.1 shows an overview of the experimental area with the ATLAS 300 and the accelerator.

This chapter will give an overview of the general working principle and the main components of the ATLAS 300 and the accelerator. It is assumed that the reader is familiar with basic concepts of short-pulse laser systems and plasma wakefield acceleration.

2.1 The Advanced Titan:Sapphire Laser System 300

The ATLAS was relocated from the Max-Planck-Institute for Quantum Optics (MPQ) to LEX in 2012, and simultaneously upgraded with a new amplifier from an 80 TW to a 300 TW system. The infrastructural and functional changes required a major redesign of the laser layout and basically all components downstream of the new amplifier (including the whole accelerator setup). An in-depth description of the ATLAS 300 and its performance can be found in the master's thesis of B. Günther[87]. This section will

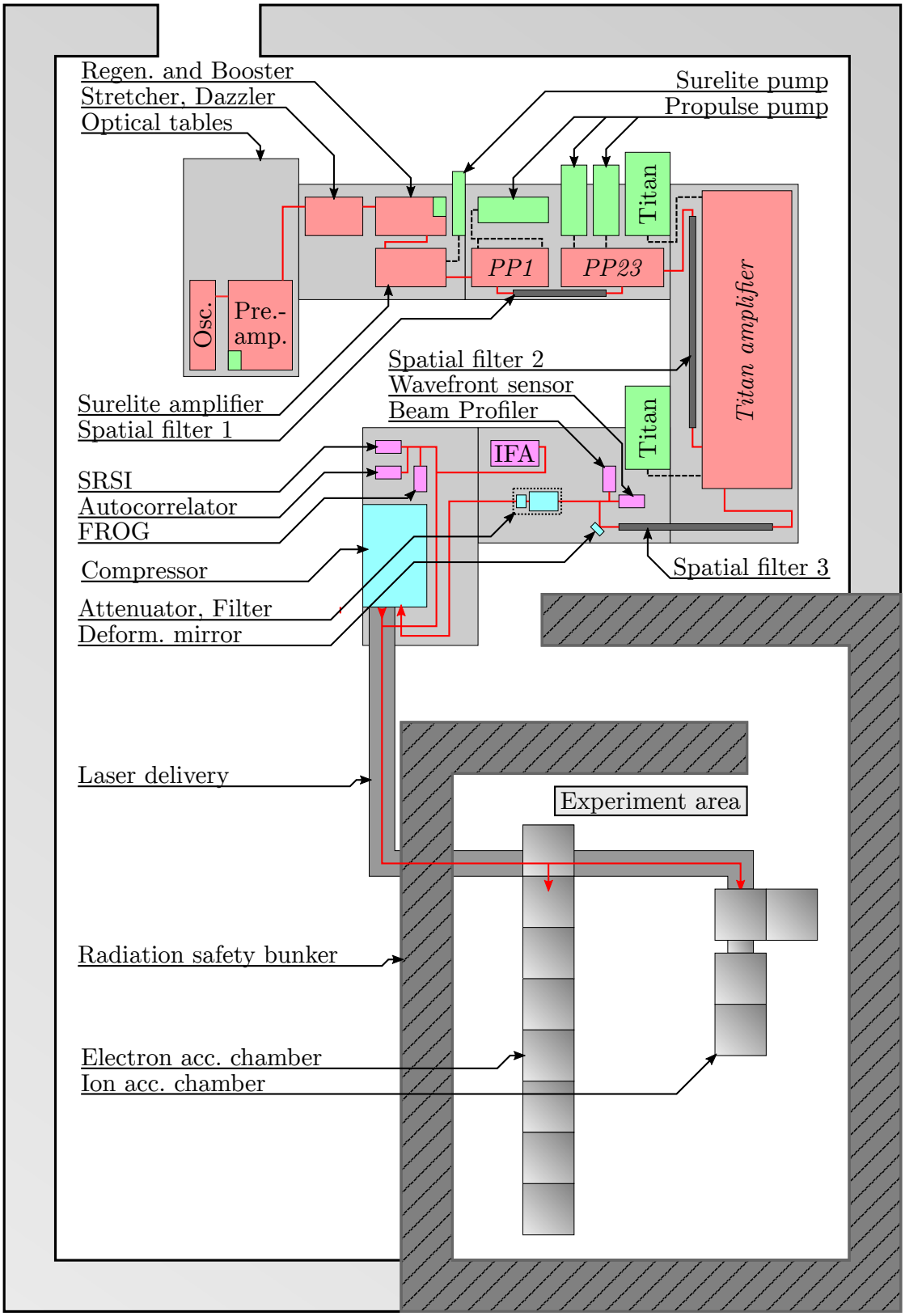

Figure 2.1: Overview of the LEX laser and experiment area.

give a mostly qualitative introduction to the main components of the laser system and how it is used to drive the accelerator.

The ATLAS 300 is a state-of-the-art Titanium:Sapphire laser system that is based on the Chirped Pulse Amplification (CPA)[35] technique. The scheme of the laser chain is shown in Figure 2.2. The first component is an optical resonator, from now on referred to as the *Oscillator*, that delivers pulses with nanojoule energy and femtosecond duration. These pulses are subsequently stretched in time by about five orders of magnitude to approximately half a nanosecond. In several amplification stages, the energy is boosted to the 10 J level, after which the pulse duration is re-compressed down to 30 fs.

The following sections describe the most important components of the laser system, from the pulse generation to the final temporal compression, in more detail.

2.1.1 Frontend and Stretcher

Figure 2.3 shows a sketch of the first part of the laser chain, from now on referred to as the *frontend*. Here, laser pulses on the millijoule-level are generated and spectrally/temporally shaped for further amplification.

The oscillator delivers 70 MHz pulse trains with sub-10 fs FWHM pulse length and 100 nm FWHM spectral bandwidth. As the following part of the laser chain works with 10 Hz, the repetition rate is reduced with a Pockels cell (*Pulse Picker*). The pulse is then slightly expanded with a reflective Galilean telescope (*Expander 1*) and pre-chirped in a glass block to a duration of 4 ps.

The first amplification stage (*Pre-Amplifier*) is a multipass amplifier pumped by a flash-lamp Nd:Yag laser (*Minilite*), which boosts the energy by five orders of magnitude to 1 mJ. This high amount of amplification results in a decrease in temporal contrast, which can have detrimental effects on the acceleration process. A saturable absorber is used for compensation, which improves the overall contrast by approximately one order of magnitude.

The pulse is then expanded a second time with a reflective Galilean telescope (*Expander 2*) and chirped in an Öffner type grating stretcher to 400 ps FWHM duration. This will eventually be compensated by the grating compressor in the end of the laser chain, but slight misadjustments and optical components that introduce further dispersion (like Ti:Sa crystals) require fine-tuning of the compression. This is achieved by pre-compensating the dispersion with a commercial acousto-optic modulator (*AOM*, *Dazzler*).Thereafter, a Pockels cell is used to further clean the contrast.

The stretcher and the AOM have combined losses of about two orders of magnitude, which leads to a remaining pulse energy of a few microjoules. This is compensated by a regenerative amplifier and a multipass amplifier (*Booster*). The main purpose of using a regenerative amplifier, however, is a cleaning of the beam profile and the ability for spectral shaping by including another AOM (*Mazzler*) that acts as an adaptive spectral filter. This is important, as the subsequent amplification leads to gain narrowing and a red-shift (due to the chirp) that needs to be compensated. The AOM filter settings are optimized in a closed loop, where the spectrum (ideally) in the end of the laser chain serves as a feedback. In practice, it can be dangerous to first align and amplify the whole

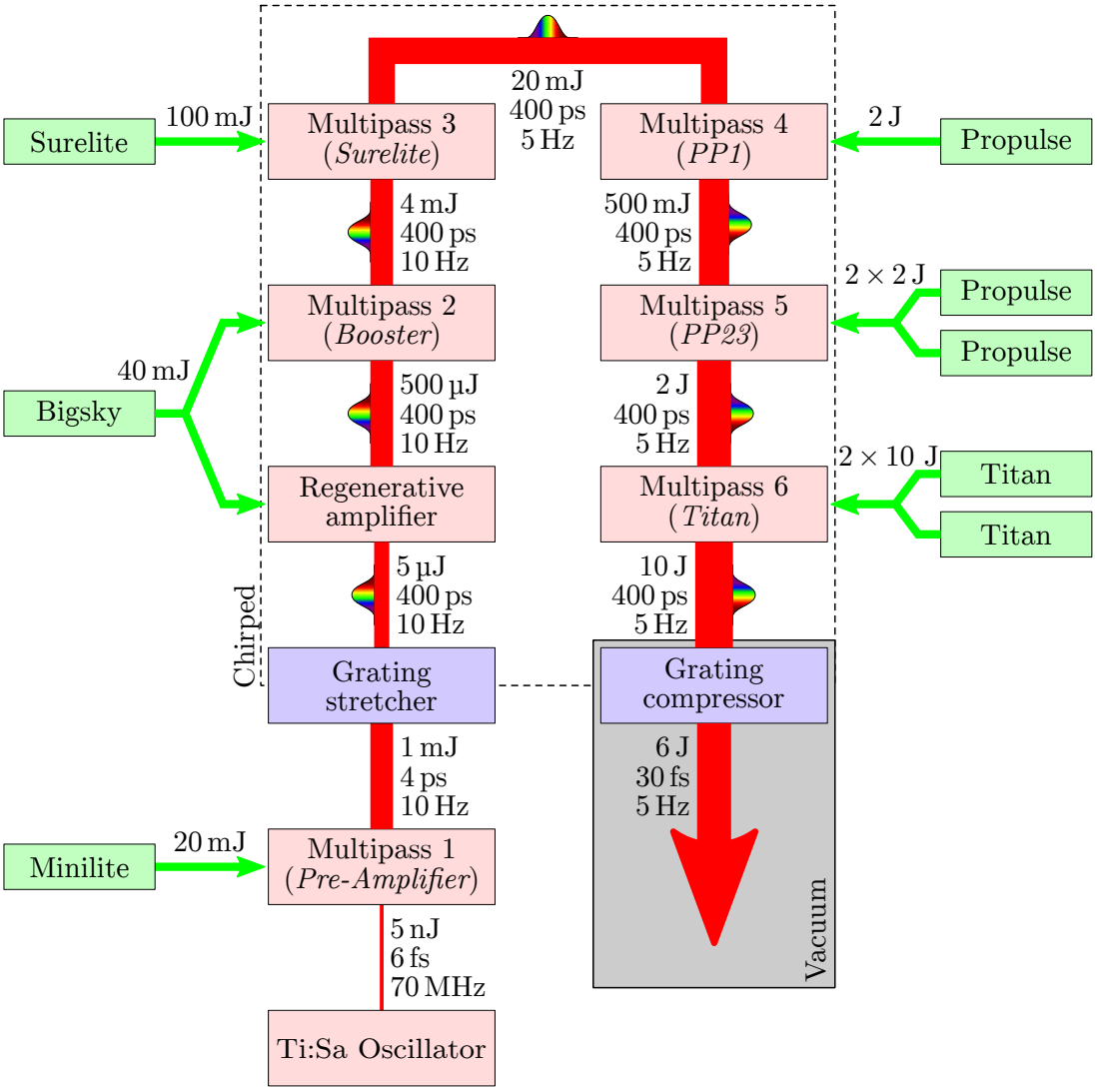

Figure 2.2: CPA scheme of the ATLAS 300.

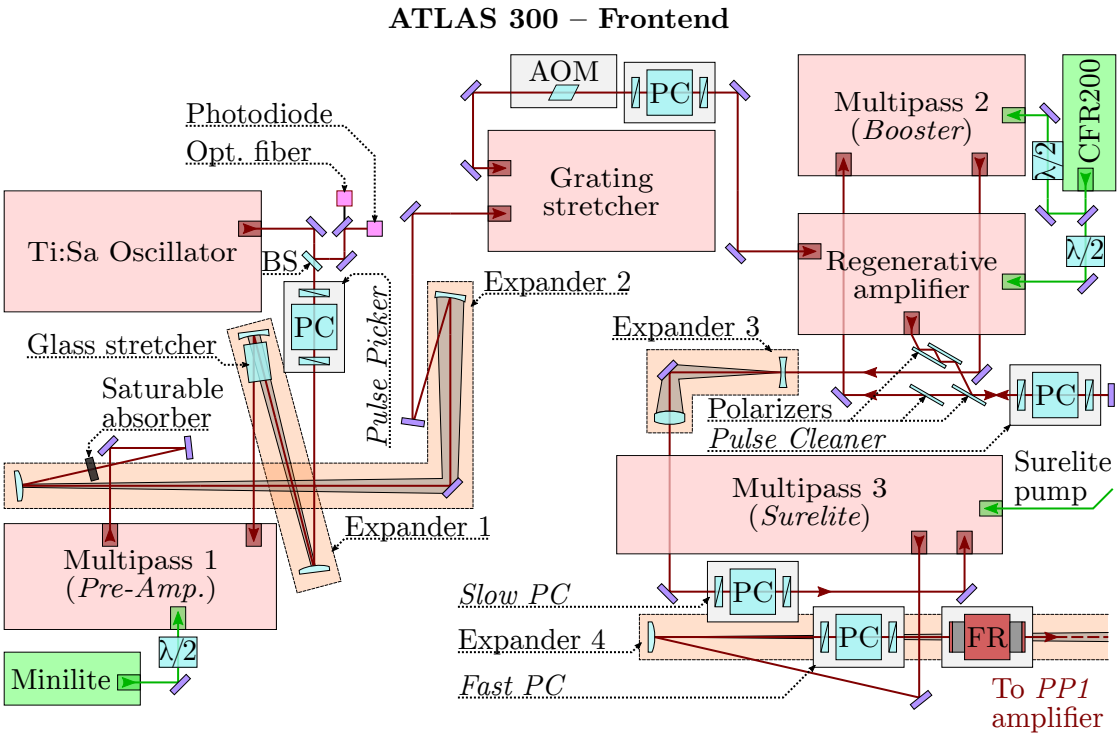

Figure 2.3: Schematic layout of the ATLAS 300 Frontend.

chain and do the spectral shaping afterwards, as uncompensated gain-narrowing leads to an increased intensity in the chirped beam, which may result in damages of optical components. So, we chose an intermediate solution and use the spectrum after the frontend as a feedback. As the manufacturer software that controls the AOM generally tries to converge to a flat spectrum, this causes a problem, as it cannot take into account the red-shift of the subsequent amplifiers. I thus implemented a pre-processing of the acquired spectrum to make the spectral filter converging towards a slightly blue-shifted spectrum, which will pre-compensated the subsequent red-shift. This was achieved by numerically red-shifting the spectrum by an amount that is close to the red-shift of the amplifiers. With this method, the resulting spectrum in the end of the laser chain is usually already reasonably flat. The filter settings can then be fine-tuned by feeding the spectrum after compression to the AOM.

After the resonator cavity of the regenerative amplifier, the pulse is cleaned with a set of reflective polarizers and a Pockels cell (*Pulse Cleaner*) to suppress pre-pulses that the cavity generates. The energy is boosted with a second multipass amplifier (*Booster*) to about 4 mJ. Both the Booster and the regenerative amplifier are pumped by a single, commercial flash-lamp Nd:Yag laser (*CFR200*).

The pulse is then expanded with a transmissive Galilean telescope (*Expander 3*) and cleaned with another Pockels cell (*Slow PC*) towards the third amplifier (*Surelite*). The latter is pumped by a commercial flash-lamp laser, which boosts the pulse energy to

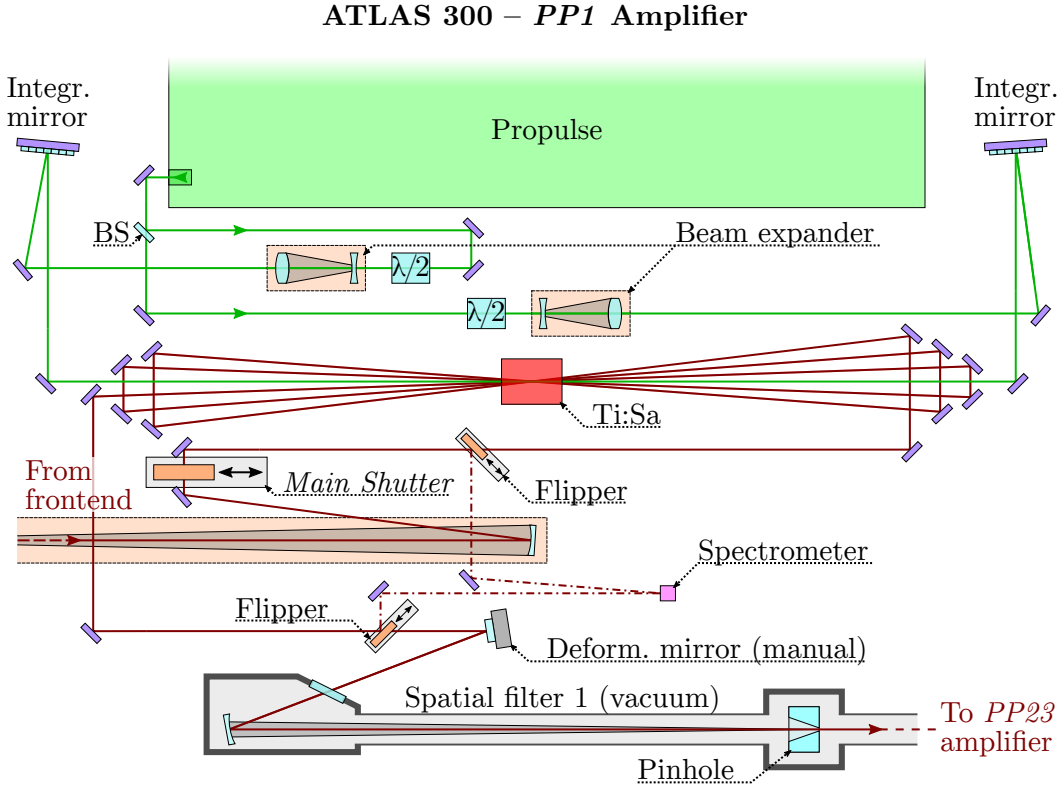

Figure 2.4: Schematic layout of the ATLAS 300 *PP1* amplifier.

20 mJ. A Pockels cell (*Fast PC*) with a particularly fast rise time of ∼300 ps is used to cut not only the remaining energy of pre-pulses from the oscillator and regenerative amplifier cavities, but also a part of the Amplified Spontaneous Emission (ASE) pedestal. It is adjusted such that it slightly cuts into the red part of the spectrum (i. e., the leading edge of the chirped pulse), so that it opens as late as possible while still allowing the main pulse to pass through. It is furthermore used to reduce the repetition rate from 10 Hz to 5 Hz.

In order to protect the system from back-reflection, e. g., if a solid target in the experimental area or some other obstacle is hit under a shallow angle, a Faraday rotator (*FR*) is placed behind the Fast Pockels Cell to block back-reflected beams and protect the frontend.

2.1.2 Power Amplifiers

The three power amplifiers after the frontend boost the energy to the final 10 J level. They are all custom multipass amplifiers pumped by commercial flash-lamp Nd:Yag lasers.

Before this first power amplifier, the beam is expanded to 1 cm diameter (*Expander 4*). A fast shutter, referred to as the *Main Shutter*, is used to select individual pulses

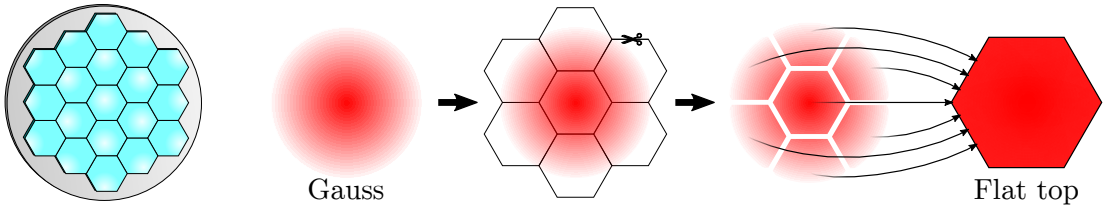

(a) Sketch. (b) Simplified homogenization principle.

Figure 2.5: Sketch and working principle of an integrating mirror that is used to homogenize the pump laser on the crystal. The mirror consists of several hexagonal plane mirrors mounted on a spherical substrate, such that their individual reflections overlap in the crystal, i. e., their centers are tangential to a common sphere. In a simplified picture, the input beam is cut into hexagonal pieces which are overlapped, as shown in (b). This creates an almost flat-top profile from an initially non-homogeneous profile like a Gaussian. Noticeably, the flat-top profile in (b) is the actual overlap of the seven pieces (normalized and scaled in size).

to pass into the amplifier chain. This can be done on a pulse-to-pulse basis and with arbitrary repetition rate up to the full 5 Hz. It is the main shutter that is used to deliver individual laser pulses requested by the accelerator.

The first power amplifier (see Figure 2.4), in the following referred to as *PP1*, amplifies the pulse energy by two orders of magnitude to 500 mJ. It is a 5-pass amplifier pumped by an Amplitude PROPULSE+ laser with 2 J energy. In order to create a uniform longitudinal inversion profile in the Ti:Sa crystal, the pump beam is split into two beams that pump the crystal from both sides. Additionally, integrating mirrors are used to create a uniform transverse inversion profile and prevent damages from possible hot-spots in the pump beam. Figure 2.5 shows a sketch and the working principle of the integrating mirrors that are used in the ATLAS system. They homogenize the output beam of the pump lasers from a Gauss-like profile to an almost (hexagonal) flat-top profile by overlapping spatial segments of the beam in the crystal. To prevent an imprint of the hexagonal pump profile on the seed beam, the two pump beams (that pump the crystal from both sides) are rotated with respect to each other, such that the inversion profile is a dodecagon, and its size is set to be slightly larger than the seed beam. The two pump beams can furthermore be individually adjusted in polarization to optimize their energy deposition in the crystal.

After the PP1 amplifier, the beam is sent through a spatial filter (*Spatial filter 1*), which consists of a long vacuum chamber in which the beam is focused through a pinhole. In this case, the pinhole is a 1 cm long glass tube with a cone-like hole in the center. The pinholes used here have a relatively large inner diameter of up to 1 mm (after several hours of operation), and are mainly used to protect from back-reflection and from high-frequency modulations that can be caused by damaged optics. The spatial filters are furthermore used as relay-imaging beam expanders. As spherical mirrors are used for

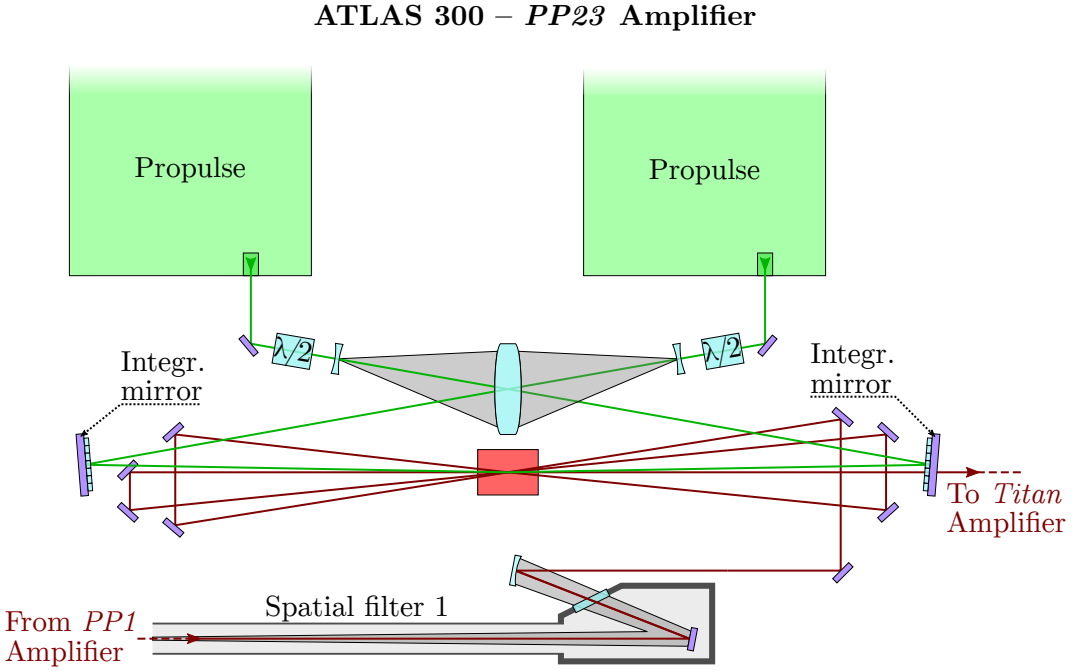

Figure 2.6: Layout of the ATLAS 300 *PP23* amplifier.

focusing and collimation, they create a small amount of astigmatism, which is (pre-) compensated with a manual deformable mirror.

The second power amplifier (see Figure 2.6), referred to as *PP23*, is similar to the PP1, but pumped with twice the energy (from two pump lasers). It boosts the energy to a level of 2 J.

The last power amplifier is the *Titan* amplifier (see Figure 2.7). The beam coming from the PP23 amplifier is again cleaned and expanded in a spatial filter with a glass pinhole. The Titan amplifier is different from the PP1 and PP23 amplifiers in the sense that the Ti:Sa crystal is cryo-cooled to −150 °C for better thermal conductivity, which is necessary because the crystal has a larger size of 50 mm × 50 mm and has a much higher heat load. In order to prevent buildup of condensation, it is enclosed in a vacuum chamber and evacuated with a turbo-molecular pump. The cryo-cooler and its helium compressor create heavy vibrations that would lead to a significant jitter in position of the laser focus in the accelerator, so the whole cryo system was mechanically decoupled from the optical table as much as possible.

After the amplifier, the beam is filtered and expanded in a spatial filter (*Spatial Filter 3*) to its final size of 10 cm FWHM diameter. The beam has an almost top-hat profile due to the homogeneous inversion profiled in the amplifier crystals that are achieved with the integrating mirrors in the pump beams. This way, the usable area on the following optics like mirrors and compressor gratings can be used in an efficient way.

A fiber-coupled alignment laser with 800 nm wavelength and 100 mW can be coupled in before the Titan amplifier. It is collinear with the ATLAS beam for aligning the

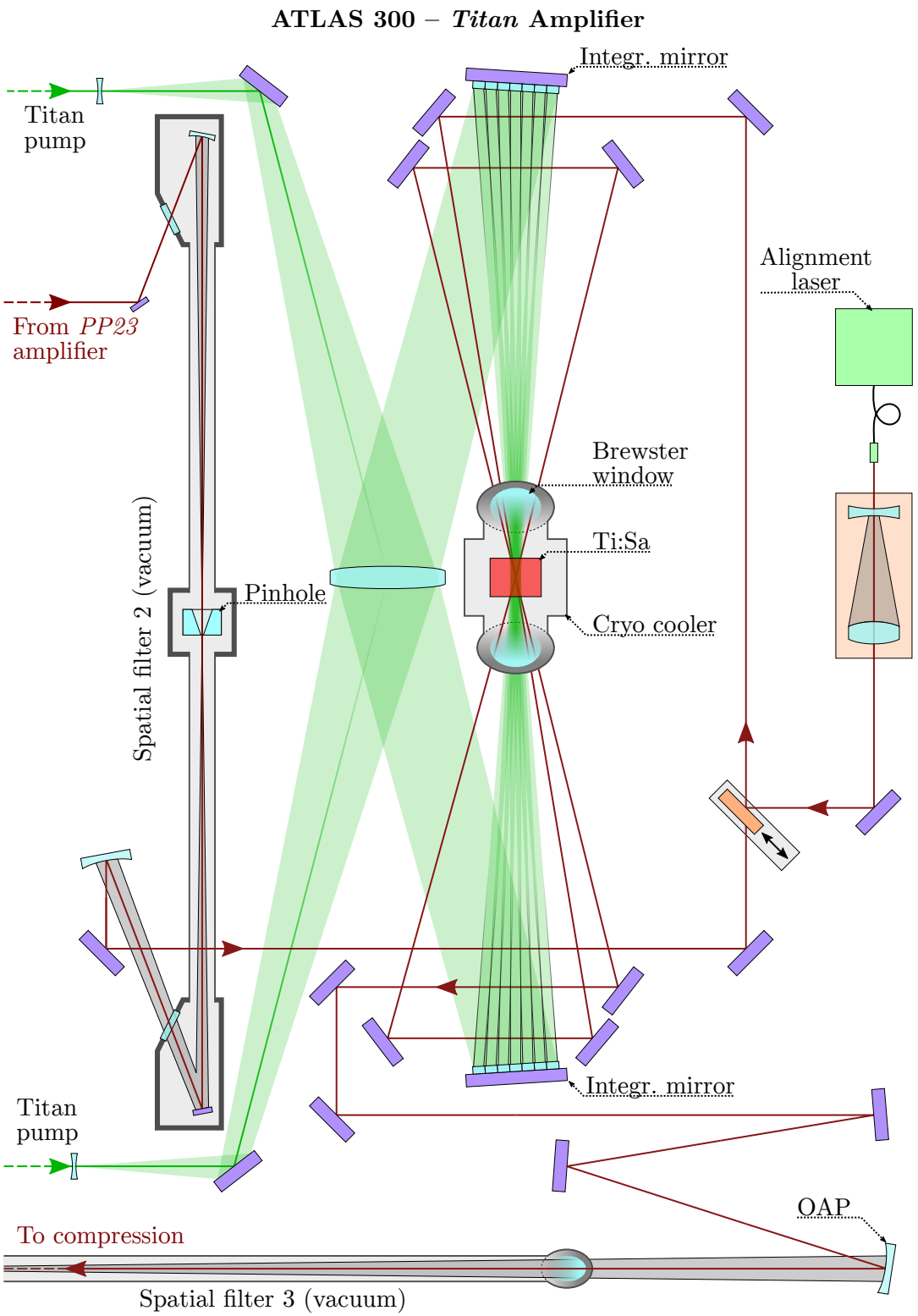

Figure 2.7: Layout of the ATLAS 300 *Titan* amplifier.

optical path towards the experiments without the risk of damaging equipment.

2.1.3 Compression and Diagnostics

After the beam exits the Spatial Filter 3 and before it is re-collimated to its final size with an off-axis-parabola (OAP), a deformable mirror is used to optimize the wavefront and compensate aberrations, e. g., from curved mirrors and imperfect optics. A wavefront sensor is used to measure the wavefront on the deformable mirror surface by imaging the transmission through a partially transmissive mirror with a correspondingly adjusted Kepler telescope. The wavefront sensor and the deformable mirror run in an automated closed loop during the alignment and beam optimization phases.

Another part of the leakage through the partially transmissive mirror is telescoped down to a camera to monitor the beam profile and detect upstream damages that can propagate and damage downstream optics.

The *attenuator* can be used to reduce the laser energy by about six orders of magnitude (ND6), which is essential for optimizing the focal spot in the experiment. It consists of an Aluminum enclosure with two 99.9 % reflective mirrors (dielectric) under approximately 45° angle to the incident beam (see Figure 2.8), where the output beam is the transmission through both mirrors. As each mirror introduces a beam offset, they are oriented such that their individually introduced offsets cancel out. The transmitted wavefront quality of both mirrors has been measured with a 633 nm interferometer to be better than $\lambda/8$ peak-to-valley (PtV). The whole attenuator can be moved into the beam path with a pneumatic cylinder. A pneumatically controllable filter stack after the attenuator can further reduce the beam energy with a total of three orders of magnitude split among four individual filters (ND1, ND1, ND0.7 and ND0.3).

The beam is then temporally compressed in a grating compressor that consists of four optical gratings and a roof mirror (see Figure 2.8). As the grating compressor cannot compensate for all orders of spectral phase that the beam acquires throughout the laser chain, it is adjusted to mostly compensate the second (i. e., the chirp) and third order of the spectral phase that the stretcher and the transmissive optical components introduce, while the AOM in the frontend is used to fine-tune the compression to below 30 fs. Grating compressors furthermore have losses due to energy going into other than the intended diffraction orders, and the transmission of the ATLAS 300 compressor was measured to be approximately 80 %, but the beam transport to the experiment degrades the overall transmission to approximately 60 % because of deteriorated mirror coatings.

After the compression, a mirror (*Diagnostic mirror*) can be inserted to deflect the beam to a diagnostics setup. An uncoated wedge is used to attenuate the beam by another order of magnitude before it leaves the vacuum chamber. A telescope reduces the beam size down to ∼5 mm diameter, and the beam can be guided to different diagnostics by a combination of flippable mirrors. Mainly four diagnostics were used, two that measure the pulse duration on femtosecond scale, one that measures the temporal contrast and one that measures the pulse front tilt.

The first diagnostic is a commercial autocorrelator (Amplitude Sequoia) that measures the temporal contrast on a nanosecond scale. This is important, because a bad contrast

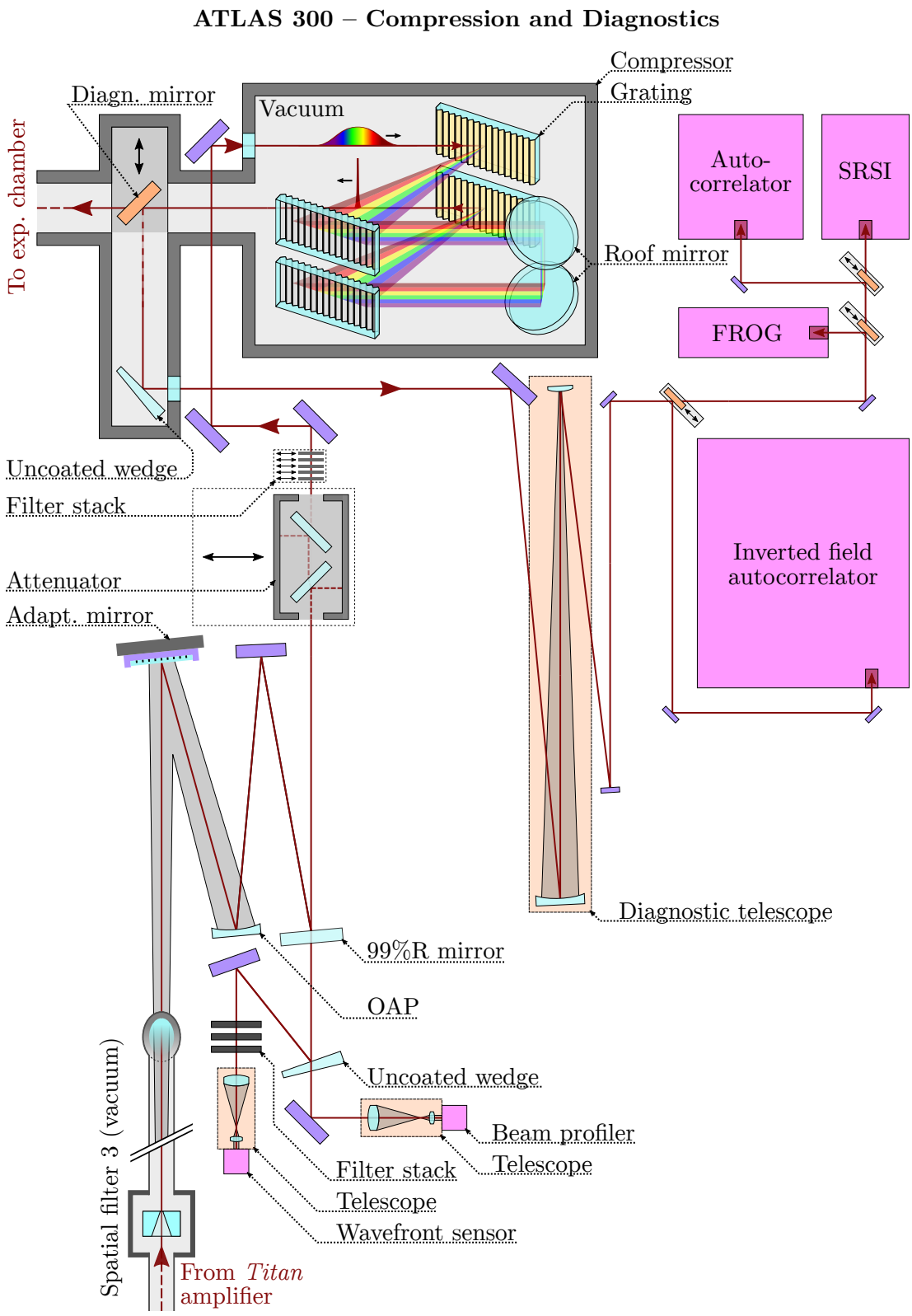

Figure 2.8: Layout of the ATLAS 300 compression and diagnostics.

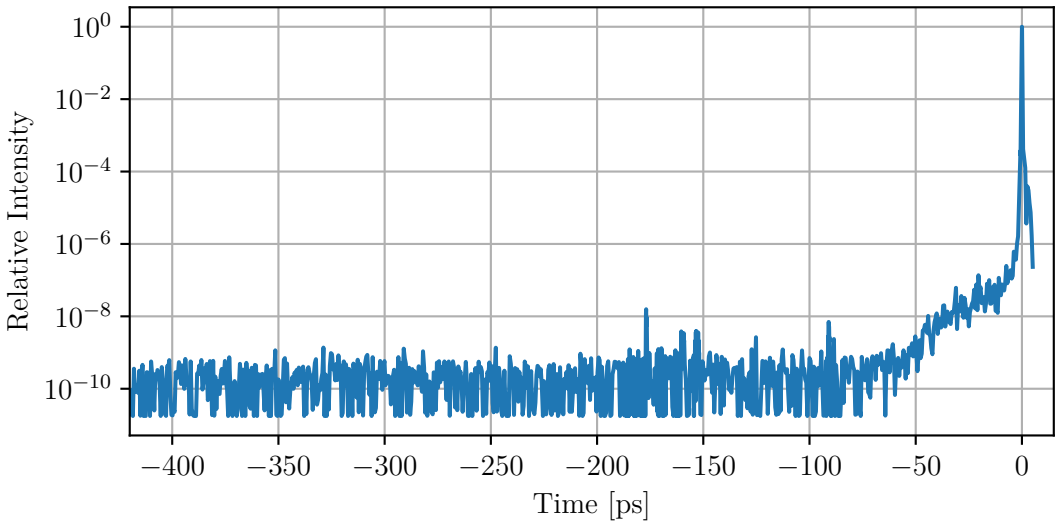

Figure 2.9: Typical temporal contrast of the ATLAS 300. The contrast >100 ps before the main pulse is approximately at a level of 10^{-9}. Several pre-pulses approach a level of 10^{-8} and one pre-pulse is slightly exceeding it (see the peak at −180 ps and smaller peaks at later times). The higher intensity at shorter times is the ASE pedestal that the Pockels cells are not able to block.

(specifically pre-pulses) can be problematic for a plasma accelerator, especially for ion-acceleration experiments. Figure 2.9 shows a typical ATLAS 300 autocorrelation trace with a contrast of 10^{-9} at >100 ps before the main pulse, and a pre-pulse slightly exceeding the 10^{-8}-level at −180 ps relative to the laser peak. The contrast was carefully and exhaustively optimized with the addition of a saturable absorber in the frontend, delays of Pockels cells and amplifier pumps, and by modifying the regenerative amplifier cavity. In order to further reduce the contrast, a cross-polarized wave generation (XPW) setup was included in the frontend, which was not used for the measurements in this thesis, though.

The compression on a femtosecond scale was measured with two different commercial diagnostics, one device based on frequency-resolved optical gating [88] (in the following referred to as *FROG*) and one device based on self-referenced spectral interferometry [89] (in the following referred to as *SRSI*). In our case, the FROG was used to optimize the compression manually with either moving the compressor gratings (usually necessary only when the laser layout was fundamentally changed) and with the AOM. Once the compression was reasonably good, the SRSI was used for further optimization of the AOM.

The SRSI (Fastlite Wizzler) measures the spectral phase and gives a feedback to the AOM in a closed loop. Figure 2.10 shows a typical measurement of the SRSI before and after the optimization.

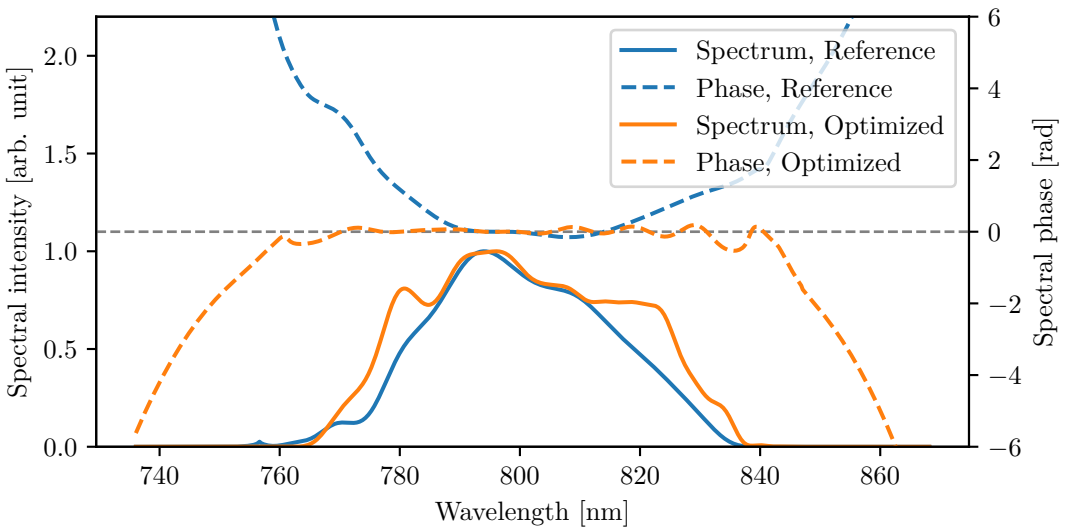

Figure 2.10: Typical spectral phase acquired with the SRSI before and after closed-loop optimization of the AOM. According to the SRSI analysis, the initial pulse has 45.5 fs (28.9 fs bandwidth-limit) duration and a second order phase of 450 fs^2. After the AOM optimization, the spectral phase is almost constant over the width of the spectrum, and the duration is reduced to 28.2 fs (28.0 fs bandwidth-limit). Here, the AOM also changes slightly the overall spectrum, which results in the difference in bandwidth-limited pulse duration before and after the optimization.

.

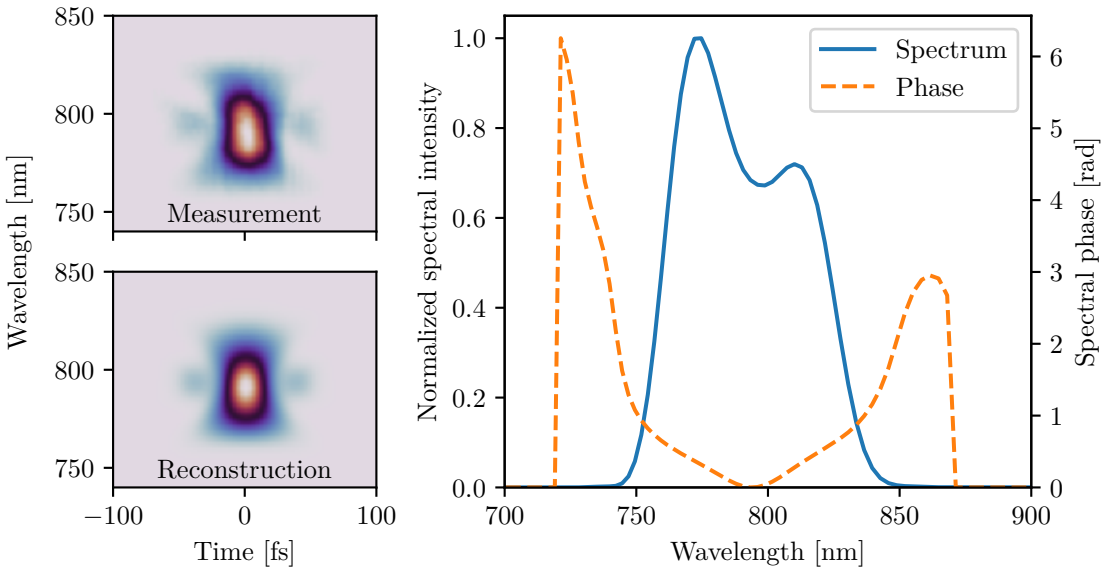

Figure 2.11: Typical FROG trace after optimization with the closed loop between SRSI and the AOM. The left side shows the experimentally acquired and the reconstructed FROG traces, the right side shows the retrieved spectrum and the spectral phase. The retrieved pulse duration is 24.1 fs.

The FROG (Swamp Optics Grenouille) measures a spectrogram from which the spectral phase can be reconstructed by iterative optimization of numerically generated spectrograms. Figure 2.11 shows a typical spectrogram along with the reconstruction and spectral phase of the ATLAS 300. It was acquired after the optimization with the SRSI-AOM-loop, and because of a mismatch of internal FROG and SRSI dispersion it exhibits a second order spectral phase (chirp). The chirp is later optimized with the electron yield in the accelerator.

The fourth diagnostic is a custom built inverted field autocorrelator[90] (*IFA*) that measures the pulse front tilt. Grating compressors, stretchers and various transmissive optics can introduce spatio-temporal couplings, which lead to e. g. angular dispersion and correspondingly a pulse-front tilt[90, 91]. This causes a decrease in achievable intensity and nonlinear effects during the excitation of plasma waves in the accelerator[92, 93]. The IFA measurement is used to iteratively adjust the orientation of the compressor gratings to remove the pulse front tilt.

After the optimization of the beam properties like energy, duration, wavefront, contrast and pulse front tilt, the beam is guided through the laser beam delivery (*LBD*) vacuum pipes to the accelerator in the radiation safety bunker.

I contributed to a large extent to rebuilding the ATLAS after the relocation to LEX and adapting it to the experimental needs. I was furthermore strongly involved in the daily operation and maintenance.

2.2 Overview of the Accelerator

The 8 m long vacuum chamber shown in Figure 2.12 contains the major part of the acceleration setup on the inside and outside. There are four main parts of the acceleration setup that was used in this work: the gas targets, electron diagnostics, a laser to pre-ionize the target, and a few-cycle probe beam.

The hybrid acceleration scheme requires a combination of two acceleration stages, for which supersonic gas jets with shock-front injectors are used here. The first target represents the LWFA stage, which is driven by the ATLAS 300 beam and generates the high-charge drive beam for PWFA stage in the second target. The setup further incorporates a foil to block the laser between the LWFA and PWFA stage, such that the interaction in the PWFA stage can be decoupled from the spent LWFA drive laser. Both targets and the foil are mounted on a hexapod that allows translating and tilting, e. g., for fine-adjustment of the target position relative to the laser focus.

Electron beam diagnostics are used to measure properties like the energy spectrum and the divergence. These mainly rely on magnetic fields to deflect electrons, and scintillating screens that generate visible light from electrons passing through them.

The transverse, few-cycle probe beam (in the following referred to as *probe*) is used to retrieve shadowgrams of plasma density modulations in the LWFA/PWFA interaction. This particularly allows to visualize the density modulations of generated plasma waves, which relies heavily on the ultra-short duration of the probe. In order to generate the probe, a small part of the LWFA drive laser is picked off, spectrally broadened, and compressed from the initial 30 fs to below 10 fs.

Another part of the LWFA drive laser is picked off and used to pre-ionize the PWFA gas target, in the following referred to as the *ionizer*. This is necessary in the cases where the LWFA drive laser is blocked by the foil, such that ionization of the gas would otherwise need to be facilitated by the LWFA-generated electron beam itself.

The following sections will describe the main components of these four parts, while many additional functional parts unfortunately need to be omitted in the scope of this thesis.

2.2.1 Gas Targets

The type of targets that were used for the hybrid experiments are custom designs of supersonic *de Laval nozzles* by K. Schmid[94] and M. Hüther[95]. One major advantage of this type of target is the ability to use the shock-front injection scheme [96] to produce ultra-high charge beams with small divergence. In the context of this work, we were able to produce electron beams of unprecedented quality, with charges of up to 1 nC divergences below 1 mrad FWHM divergence.

The nozzles are individually supplied with H_2 gas from controllable electro-pneumatic pressure regulators (Tescom ER3000 and ER5000). The conversion of backing pressure to gas jet density at the nozzle outlet depends strongly on the nozzle type. The pressures that were used in this work were usually in the range of 2 bar to 20 bar for reaching

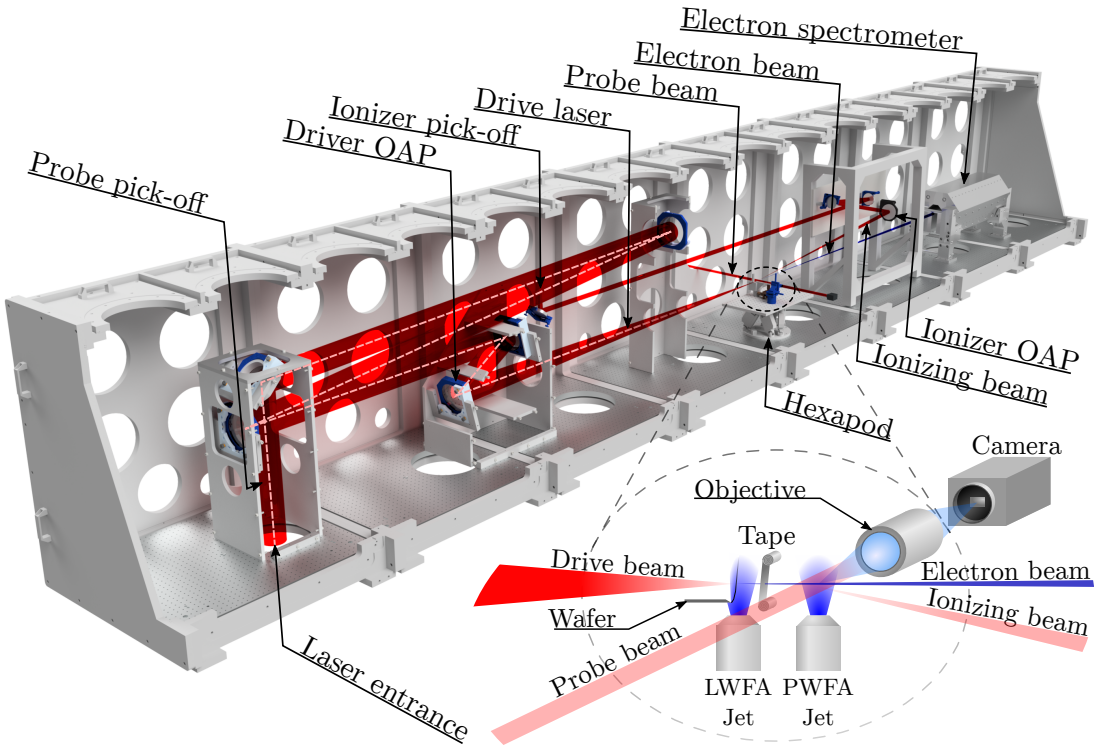

Figure 2.12: Layout of the experiment vacuum chamber (selected components only). The beam enters the vacuum chamber on the left (*Laser entrance*) from the laser beam delivery (LBD) below. The drive beam is folded to compensate for the additional delay of the probe beam, before it is focused by the off-axis parabolic mirror (*Driver OAP*) into the target (see the zoomed sketch). Two parts of the drive beam are picked off for an optical probe and an ionizer beam. The probe beam is picked off right after the beam enters the vacuum chamber (*probe pick-off*) and then reflected out of the chamber (see Figure 2.24 for more information). The ionizer beam is folded via a mirror on a translation stage onto an off-axis parabolic mirror (*Ionizer OAP*), which focuses under 173° with respect to the drive laser into the PWFA target.

Nozzle	Orifice diameter d_o [mm]	Throat diameter d_t [mm]	Opening angle	Diameter Ratio ϵ	Mach number M (H_2)
P5	5	0.61	7.4°	8.2	6.34
P7	7	0.86	9.6°	8.14	6.32
Laval 1000	1	0.33	7.13°	3	3.8
Laval 1500	1.5	0.5	7.13°	3	3.8
Laval 3000	3	1	7.13°	3	3.8

Table 2.1: Overview of the Nozzles used in this work. They were designed by M. Hüther [95] and K. Schmid [94], and the mechanical dimensions are taken from their corresponding works. The ideal Mach number for H_2 gas was calculated with equation 2.2.

plasma densities in the order of $1 \times 10^{18}\,\mathrm{cm}^{-3}$. Each nozzle is operated with a fast valve (Parker) and opened for usually 2 ms before the arrival of the ATLAS 300 laser.

De Laval nozzles are devices that were initially designed for steam turbines[97] and later adapted to various other fields including rocket and jet engines. Their key feature is that they allow to create supersonic gas jets with an almost homogeneous density plateau. They consist of a convergent part that chokes the gas at a throat, followed by a divergent part where the gas expands and reaches supersonic velocities. Figure 2.13 shows a sketch of the cross section of a De Laval nozzle. The gas accelerates in the convergent part to keep the mass flow constant, and the Mach number reaches $M_t = 1$ at the position of the throat (as long as the ratio of inlet and throat pressure is reasonably high)[98].When the gas subsequently flows through the divergent part, the pressure leads to an expansion and further acceleration to supersonic velocities $M > 1$. An important parameter defining the properties of the gas jet is the ratio ϵ of the nozzle orifice area A_o to the throat area A_t (the section with minimum diameter)

$$\epsilon = \frac{A_o}{A_t} = \left(\frac{d_o}{d_t}\right)^2 \tag{2.1}$$

with the diameters d_o and d_t corresponding to the areas A_o and A_t. These are connected to the Mach number at the nozzle orifice M_o by[98]

$$\epsilon = \frac{M_t}{M_o}\sqrt{\left\{\frac{1 + M_o^2(k-1)/2}{1 + M_t^2(k-1)/2}\right\}^{\frac{k+1}{k-1}}} \tag{2.2}$$

where $M_t = 1$. This means, for a given ϵ there are two different solutions for the Mach number M_o, as shown in Figure 2.14, as for each ϵ one operation mode with subsonic and one with supersonic flow exists.

The nozzles that are used in this work are the *P5* and *P7* nozzles designed by M. Hüther [95] and the *Laval 1000*, *Laval 1500* and *Laval 3000* nozzles by K. Schmid [94]. Their properties, including the Mach number for H_2 gas, can be found in Table 2.1.

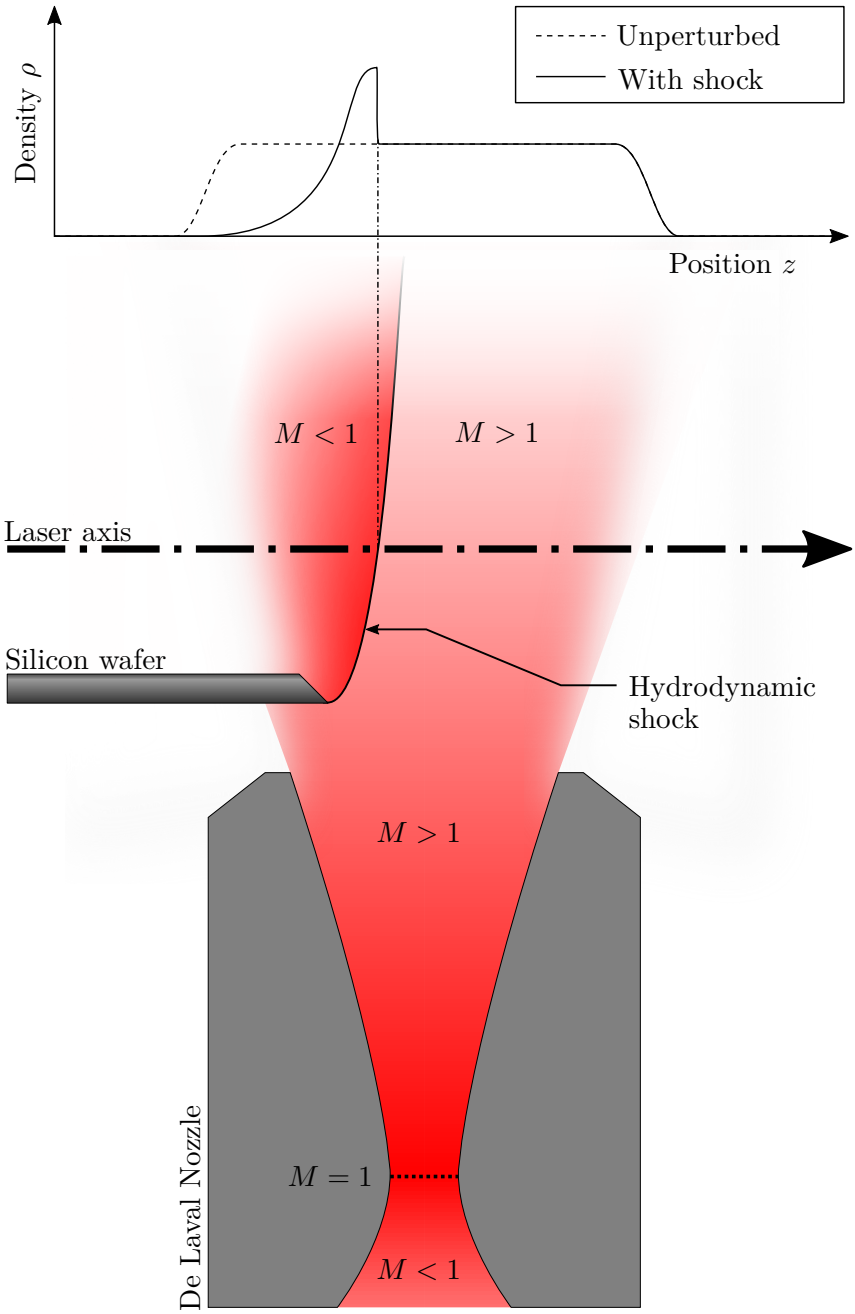

Figure 2.13: Sketch of a de Laval nozzle with hydrodynamic shock created by a silicon wafer. The graph shows the schematic density profile at the height of the laser axis with and without the silicon wafer. The nature of the De Laval nozzle is that (with sufficiently high backing pressure) the mach number at the throat becomes $M = 1$ and further accelerates upstream to $M > 1$ such that the jet is supersonic. This leads to the formation of a hydrodynamic supersonic shock with a sharp density transition (shock front) that can be exploited for electron injection in the acceleration process.

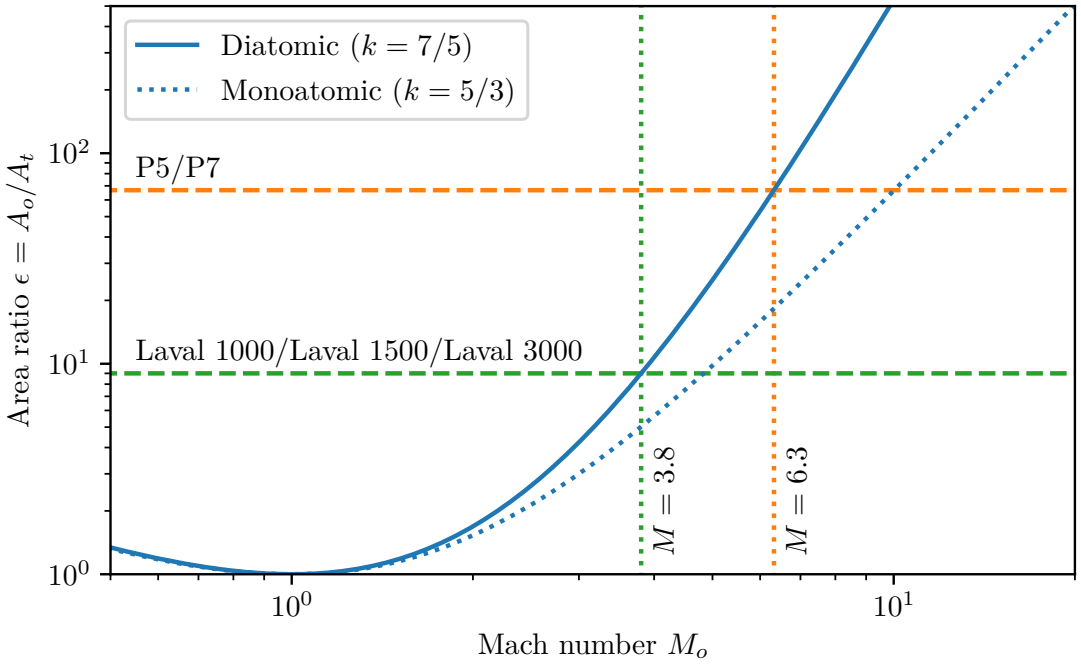

Figure 2.14: Ratio ϵ of nozzle orifice to throat area as a function of the Mach number at the orifice M_o for mono- and diatomic gases. The area ratios are plotted with dashed lines for the P5 and P7 nozzles (orange) and the Laval 1000, Laval 1500 and Laval 3000 nozzles (green). The corresponding Mach numbers for diatomic H_2 gas are marked with dotted lines.

These nozzles generate gas jets with high Mach numbers, which allows creating hydrodynamic shocks by introducing obstacles into the flow. These shocks can be used to facilitate controlled electron injection into the plasma wave[96]. Usually, razor blades or similar sharp edges are used as obstacles. In this work, the sharp edge of a 500 µm thick mono-crystalline (100) silicon wafer is used, that is broken along the (111) surface to create a 54.7°(= $\arctan\sqrt{2}$) angle with respect to the (100) plane. This edge is thus inherently straight and sharp. A rendering of such a wafer is shown in Figure 2.15. Another advantage is the high rigidity of the silicon that results in little deflection and jitter when impacted by the supersonic gas jet.

The sharp edge that creates the supersonic shock needs to be aligned such that it is as perpendicular as possible to the drive laser axis to minimize the lateral tilt of the shock front, as it leads to diffraction (i. e., steering) of the laser beam in the LWFA process. Figure 2.16 shows a misaligned shock-front in a shadowgram, which appears oval instead of line-like.

The density profiles of the gas jets were characterized in situ with interferometry of the ionization channel (see the thesis of Wildgruber[99] for a detailed description and further information). It was furthermore verified with shadowgraphic measurements of

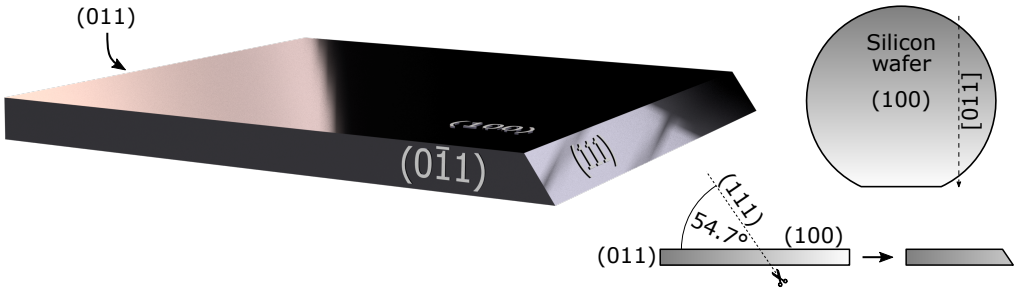

Figure 2.15: Rendering and schematic view of the crystal planes of a (100) Silicon wafer broken along the (111) surface in the Miller Index Notation. Note, the [011] index in square brackets denotes the vector perpendicular to the (011) plane.

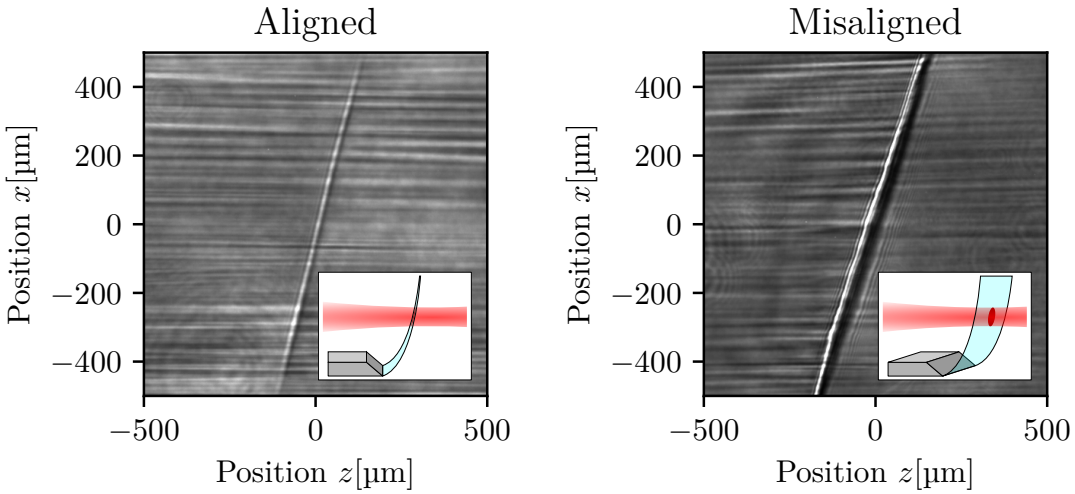

Figure 2.16: Shadowgrams of the shock-front, respectively for a wafer that is aligned and misaligned to the LWFA drive laser axis (assuming the probe is well perpendicularly aligned). The aligned wafer shows an almost line-like shock, while the misaligned wafer produces an oval shape in the shadowgram due to the projection in the probe axis.

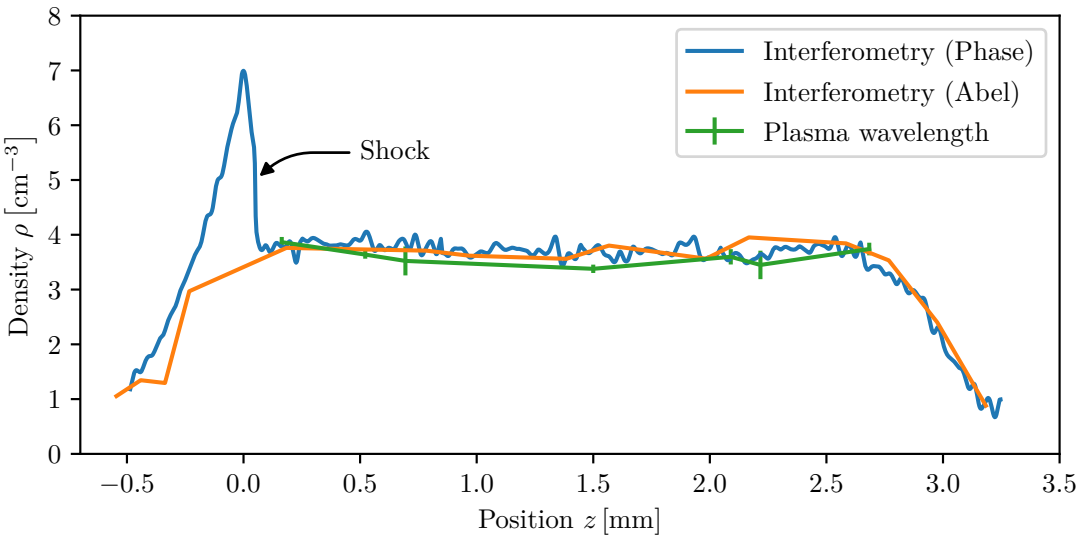

Figure 2.17: Plasma density profile of the gas jet from the *P5* nozzle on an axis 2 mm above the orifice. The density profile is reconstructed from interferometric measurements via an Abel transformation (orange) and the integrated phase scaled to the Abel-transformed density (blue) via a constant conversion factor. Also, the density is calculated from measuring the wavelength of plasma waves (green) in various positions of the jet (66 samples), under the assumption of a linear plasma wave.

the plasma wavelength. Figure 2.17 shows the density profile of the P5 nozzle with a shock-front. Here, the laser axis is 2.5 mm above the nozzle outlet and 1.8 mm above a silicon wafer that creates the shock front. The interferometric measurement relies on Abel inversion of the measured phase shift of the probe, which yields the density profile of the ionization channel under the assumption of radial symmetry. However, the reconstruction with the Abel inversion shows a significant amount of artifacts manifesting in increasing density towards the boundaries of the ionization channel, which is likely caused by the assumption of radial symmetry not being valid. Another problem with this assumption is, that it is not possible to reconstruct the density in the vicinity of the shock, as it is usually vertically tilted to the LWFA drive laser and thus not rotationally symmetric (see the aligned case of Figure 2.16). Reconstruction via a full tomography (without the assumption of radial symmetry) would allow to resolve non-symmetric features, but this is not feasible in our setup.

Another approach is to use the probe phase shift directly as a measure of the density. This way, also a closer vicinity around the shock can be resolved. The refractive index of the plasma results in an absolute/integrated phase shift of[99]

$$\Delta\Phi(y,z) = -\frac{\omega}{2cn_{\mathrm{cr}}}\int n_e(x,y,z)dx \tag{2.3}$$

with respect to the propagation through vacuum or gas. Here, x is the dimension along which the probe propagates (lateral to the LWFA drive laser), and y is the vertical dimension. The variable n_{cr} denotes the critical density with respect to the wavelength ω of the probe, and n_e is the plasma electron density. The plasma density $n_e = \alpha\tilde{n}_e$ can be thought of as a combination of the unionized electron density $\tilde{n}_e$ and the ionization ratio α. Here, $\alpha = \alpha(x,y,z)$ is generally a function of all spatial dimensions. For the Abel inversion it was assumed that α is radially symmetric at each z, which may not be true if the drive laser is not perfectly round. If one assumes that the ionization channel is fully ionized and has sharp boundaries, and that $\tilde{n}_e$ does not change along x (i. e., the diameter of the ionization channel is small compared to the size of the jet), the integration over x simplifies to a multiplication of n_e with the length of the ionized region l_x along x

$$\Delta\Phi(y,z) \approx -\frac{\omega}{2cn_{\mathrm{cr}}}n_e(x=0,y,z)l_x(y). \tag{2.4}$$

Here, we are mainly interested in the density profile along the LWFA drive laser axis ($y = 0$), i. e., in the vertical center of the ionization column. In our measurements, the parameter l_x was unfortunately inaccessible. In case the ionization channel was round, l_x can be measured from l_y in the shadowgrams or interferograms, but the artifacts in the Abel inversion suggest that this is not valid. As the size of the ionization column is mostly defined by the outer, low-intensity part of the laser beam profile, it is changing only slightly over the Rayleigh length. So, if the density can be measured by other means at one or several points in the gas jet, the phase shift $\Delta\Phi$ can be used to infer l_x at these points and interpolate/extrapolate over the full jet length. This then allows to resolve even rapid changes in the density n_e, e. g., in the vicinity of the shock.

Figure 2.17 shows the density profile inferred with this method. Here, the density retrieved by the Abel inversion within the plateau was used to calculate l_x, which was assumed to be constant over the length of the jet. The justification of this assumption can be found in [100] (Figure 2C) and the thesis of L. Wildgruber [99] (Figure 4.5), where the transverse size of the channel stays almost constant over the length of the jet. As the absolute value of the density might still be wrong because the results from the Abel inversion were used, we cross-checked the density with shadowgraphic measurements of the plasma wavelength. Here, we assumed that after several wave periods the wavelength is equal to the cold plasma wavelength. This is a good approximation, as Ding *et al.* showed that the nonlinear plasma wavelength only differs by up to 13 % from the cold plasma wavelength [100] in our parameter range. Figure 2.17 also shows that these densities are in very good agreement with the interferometric measurement to a level of 10 %. Here, 66 shadowgrams with plasma waves were analyzed at seven different positions. The wavelengths were calculated by using a numerical autocorrelation that yields the periodicity.

2.2.2 Laser Blocking Foil

The use of two closely separated acceleration stages sometimes requires to block the laser in between. In particular, in our studies it was necessary to verify that plasma waves in the PWFA stage were not driven by the remaining LWFA drive laser. This can be achieved by placing a thin foil between both acceleration stages. Even for fully depleted laser pulses the intensity so close to the target will be high enough to ignite a plasma on the surface, which will quickly rise above the critical density and act as a plasma mirror. The electrons, on the other hand, have sufficiently high momenta to pass through the foil. However, there are detrimental effects that cause the electron beam quality to degrade, mainly in terms of divergence (or emittance).

In the context of this work, a *Video-Home-System* (VHS) tape was chosen as a foil for mechanical and availability reasons. It is a 15 µm-thick Mylar foil (polyethylene terephthalate) with 12.7 mm width and several tens of meters of length. The downside of using VHS tape is that it has a metal oxide coating that deposits on nearby optics when exposed to the laser radiation. This was particularly problematic for the shadowgraphy objective (c. f. 2.2.4), because the oxide layer coated the entrance pupil and resulted in heavy distortions of the shadowgrams within several tens of shots. Non-coated Mylar is recommended for future studies.

There are mainly three mechanical requirements for the foil and its mount. Firstly, the necessary increase in LWFA/PWFA stage separation to accommodate the foil needs to be as small as possible in order to minimize the electron beam size in the PWFA stage. Secondly, the tape needs to be kept under tension to reduce the fluctuation in position, as this will manifest itself in a jitter in transverse beam size in the PWFA stage. Thirdly, the laser creates holes in the foil of approximately ∼1 mm diameter, so the foil needs to be moved to an undamaged region for each shot.

These requirements made it necessary to design a custom tape mount, which is shown in Figure 2.18. The mount body was printed with a 3D stereolitographic Digital Light

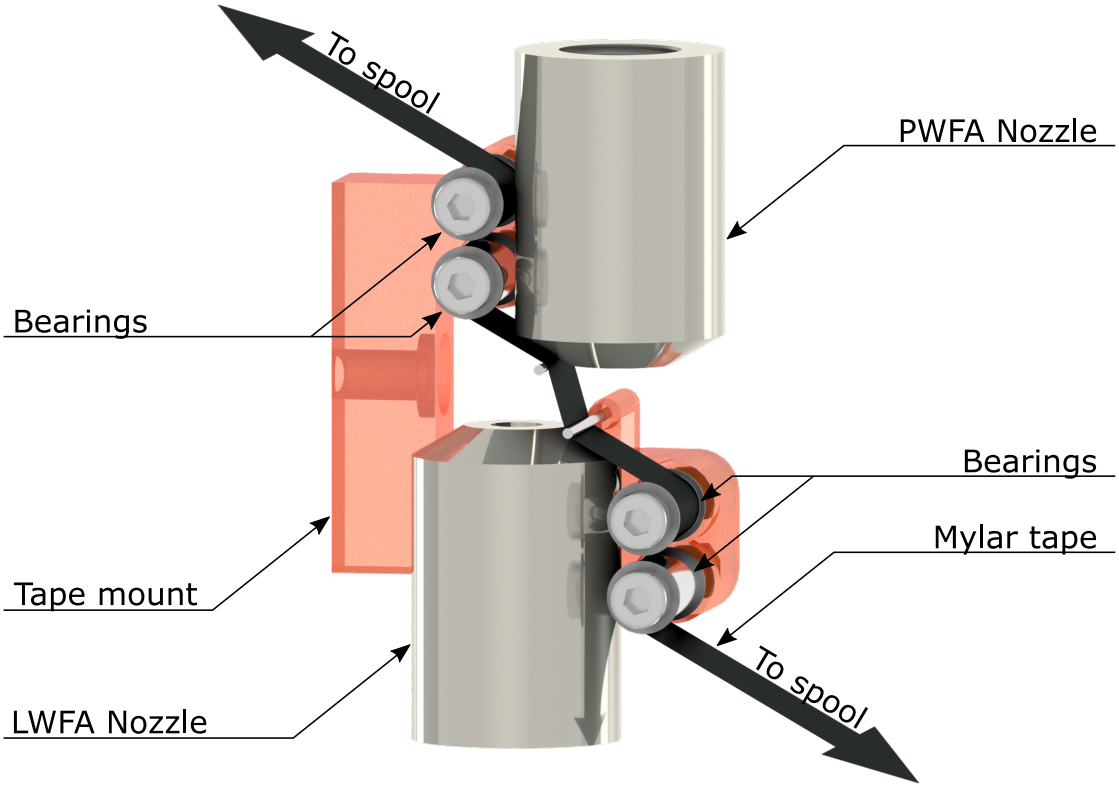

Figure 2.18: Rendering of the foil mount with the LWFA (left) and PWFA nozzles (right). The orange solid was 3D printed from resin.

Processing (DLP) printer from resin, and assembled with bearings to rigidly guide the tape between the nozzles while allowing the tape to be moved along its length. The tape was wound up on two spools in ∼10 cm distance from the targets, which allows to accommodate fresh tape for a virtually unlimited amount of shots until the vacuum chamber needs to be opened for replacing the tape. The spools were attached to DC motors with gear reduction that are controlled by a custom electronic circuit. The foil was kept under tension by running the motor that winds up slightly faster than the motor unwinding. After each shot, a computer signaled the controller to move the foil by several millimeters to a fresh spot.

Figure 2.19 shows the effect of the foil placed ∼3 mm behind the end of the LWFA gas jet (the position where no plasma is visible in the shadowgram any more). The energy and charge of the electron beam changed only slightly from (173 ± 15) MeV and (331 ± 57) pC to (180 ± 18) MeV and (311 ± 69) pC, while the divergence increased from (1.2 ± 0.5) mrad to (2.4 ± 0.6) mrad by a factor of two (from 20 consecutive shots each).

There are mainly three mechanisms that influence the electron beam when propagating through the foil. Firstly, the electrons scatter on the foil atoms via multiple Coulomb scattering. Secondly, the laser accelerates electrons from the foil surface through the foil that undergo current filamentation instabilities (CFI) and generate strong magnetic fields that scatter the trailing electron beam. Thirdly, when the electron beam impinges on the foil surface, it collides with the near-field coherent transition radiation[101] (NF-CTR), which are basically its own reflected self-fields.

The rms scattering angle of multiple Coulomb scattering can be approximated by[102]

$$\theta_{\mathrm{rms}} = \sqrt{\langle\theta^2\rangle} = 13.6z\frac{1}{\beta}\frac{1}{p\,[\mathrm{MeV/c}]}\sqrt{\frac{X}{X_0}}\left[1 + 0.088\log_{10}\frac{X}{X_0}\right] \tag{2.5}$$

where $z = 1$ is the charge state of electrons, X the length of the material, X_0 the radiation length of the material, $\beta = v/c$ the ratio of velocity to the speed of light and p the momentum. Mylar has a radiation length of $X_0 = 28.54$ cm [103], which leads to a scattering angle of $\theta_{\mathrm{rms}} = 62$ µrad for a 100 MeV electron beam. This is well below the typical natural divergence of 1 mrad that we achieved in our studies, so the increase of divergence due to multiple Coulomb scattering is small.

The influence of the collision with the near-field coherent transition radiation (NF-CTR), which is basically the reflected self fields, can be modeled under some assumptions and simplifications. Corde *et al.*[104] derived a formula for the transverse kick of the beam electrons under the assumption of pancake-like Gaussian drivers and the self-fields being perfectly reflected by the foil surface. For an electron at the longitudinal bunch center $\xi = 0$ and radius $r \lesssim \sigma_r$ close to the center, the transverse kick can be calculated with [104]

$$\Delta p_r \approx -\frac{e^2 N r}{8\pi\epsilon_0 c\sigma_r^2} \tag{2.6}$$

where N is the electron density. As the change in momentum scales linearly with the radius, the foil surface focuses the electron beam, and the focal length can be calculated with $f \approx -rp_z/\Delta p_r$. Under certain parameters, as shown in Figure 2.20, this kick can

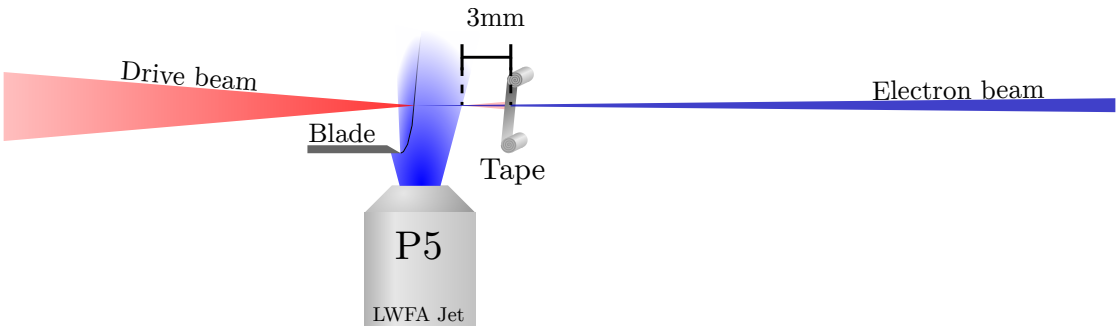

(a) Sketch of the setup.

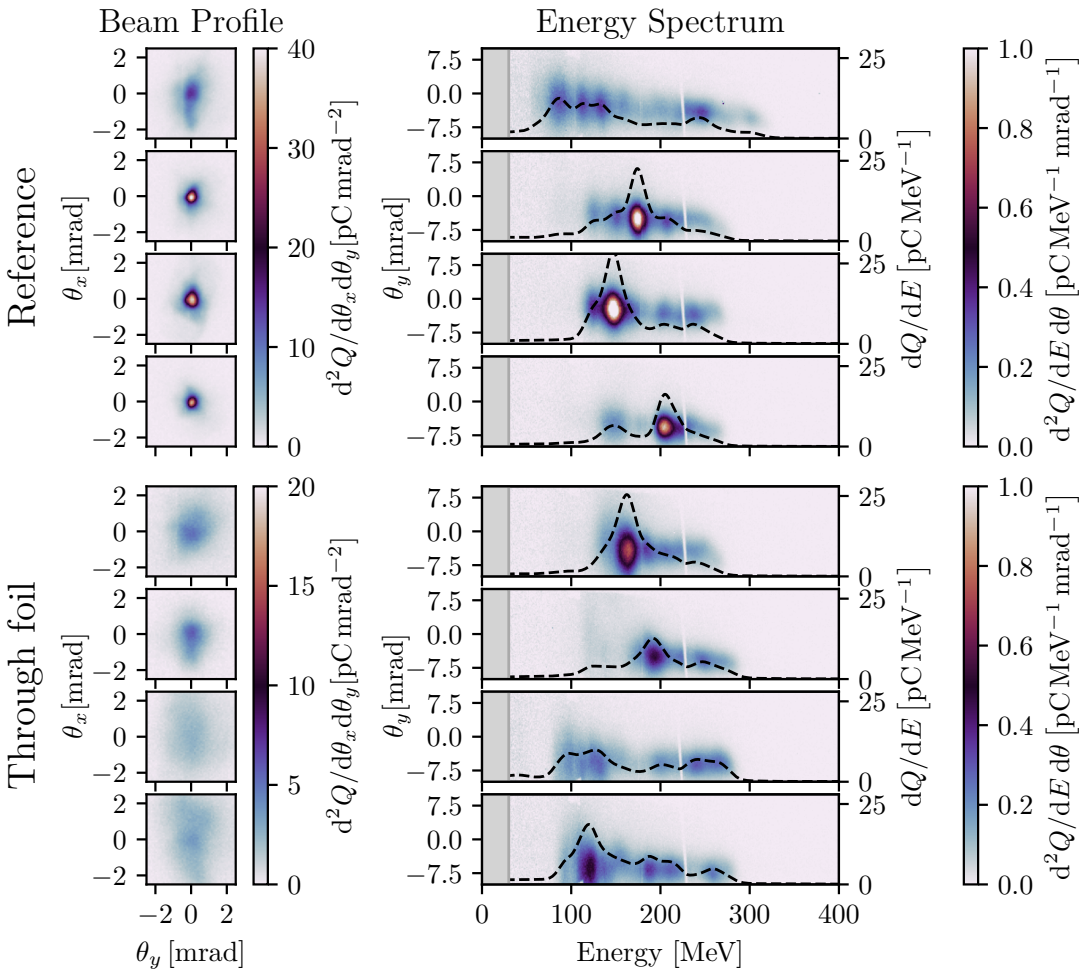

(b) Electron beam divergence and spectrum with and without the foil.

Figure 2.19: Influence of the foil on the electron beam divergence and spectrum. Shown here are exemplarily four representative shots each for the case without (reference) and with the foil in the beam path. While the spectrum is only slightly changed, the divergence is increased by a factor of ~ 2. Note, that the divergence monitor increases the divergence of the beam, such that it appears to be larger in the spectrometer.

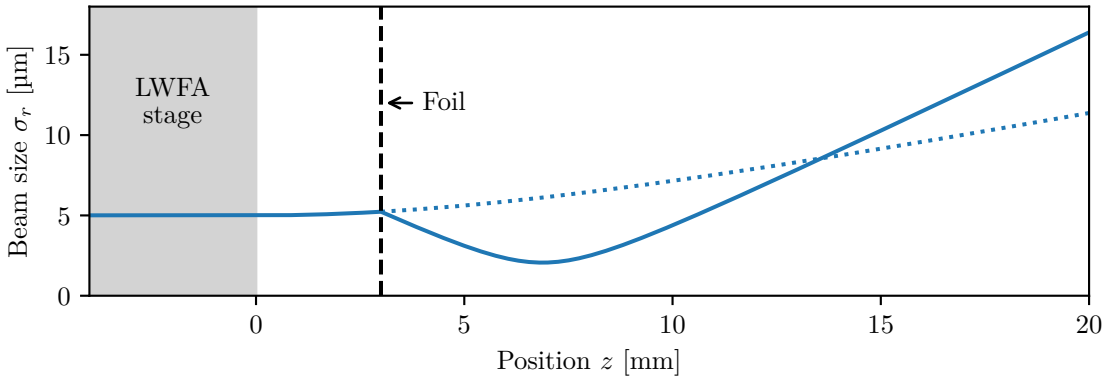

Figure 2.20: Influence of the beam collision with the NR-CTR. The solid line shows the beam propagation with the foil in 3 mm distance from the end of the LWFA stage, and the dotted line shows the beam propagation without the foil. Here, the beam transport is calculated with beam optics, and the foil is assumed to be a thin lens with focal length according to the model in [104]. The electron beam is assumed to be initially at its waist with transverse size of $\sigma_r = 5\,\mu\text{m}$ rms, emittance of $\epsilon = 1\,\text{mm mrad}$, kinetic particle energy of 200 MeV and charge of 300 pC. The divergence changes from 1.2 mrad FWHM to 2.9 mrad by the foil.

result in an over-focusing and overall increase of divergence. Here, the foil is assumed to be 3 mm behind the end of the LWFA stage, the beam propagation is modeled with particle beam optics (see e. g. [105]) and the focusing properties according to [104]. A longitudinally central slice of an ideal monochromatic electron beam with 200 MeV, normalized emittance of 1 mm mrad and 300 pC was considered. It is focused from initial 5 µm rms to ∼2 µm rms, where the divergence increases from 1.2 mrad by a factor of 2.4 to 2.9 mrad. Due to the large bandwidth and the varying focusing strength over the length of the bunch, the overall focus will be washed out. However, this effect can still lead to an overall focusing as in [101] and might even be beneficial for the hybrid accelerator.

The influence of the CFI-generated fields is more difficult to estimate, as it is sensitive to the laser parameters at the foil surface, which are not accessible with the diagnostics that were used in our studies. Furthermore, the highly nonlinear laser-plasma interaction makes it difficult to estimate the laser properties by other means. Similar to the collision with the NF-CTR fields, the effect on the divergence increases with the distance to the LWFA stage.

One conclusion is that the divergence is mainly changed by scattering on CFI-generated magnetic fields and/or the collision with the beam self-fields. Even though it is difficult to calculate their individual contributions, they have in common that the magnitude depends on the distance of the foil to the target. The increase in divergence we observe is in good agreement with the work of Raj *et al.* [106].

In the future, blocking the laser might become even more relevant as it is required to

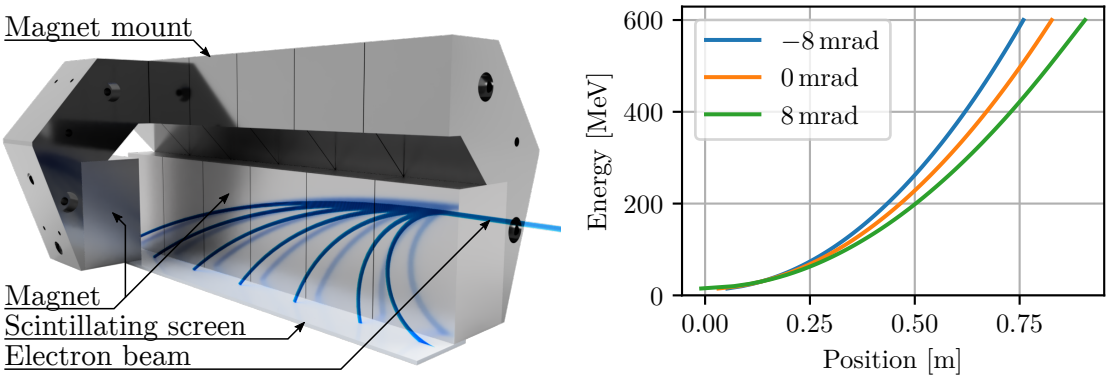

(a) Rendering.

(b) Energy calibration

Figure 2.21: Rendering (a) and energy calibration (b) of the electron spectrometer. The rendering shows the six individual magnets (five of which cut in half for better visibility), the scintillating screen and the trajectories for particles with different energies. The calibration (b) shows the incidence points on the scintillating screen of particles with energies up to 600 MeV and different pointing angles.

utilize advanced injection schemes for ultra-low emittance beam generation that rely on selective ionization of the background gas in the PWFA stage like Trojan Horse [44, 107] and WII [43, 46].

2.2.3 Electron Spectrometer and Pointing Screen

The *electron spectrometer* is the device that measures the energy distribution of the electron beam. This is achieved by propagating it through magnetic fields of a dipole magnet, which forces electrons onto circular trajectories with radii depending on their kinetic energy. This essentially converts momentum into a spatial separation, which can then be measured with scintillators. The spectrometer mainly consists of dipole magnets in a mounting fixture, and a scintillating screen placed below. Figure 2.21a shows a rendering of the spectrometer, along with sketched particle trajectories for different kinetic energies. The scintillating screen locally emits green light when hit by an electron, so the beam profile on the screen can be retrieved with a camera.

The spatial distribution of the electron beam on the scintillating screen can be converted to an energy distribution with analytic models or particle-tracking simulations. The magnetic field of the spectrometer magnet is oriented horizontally and perpendicularly to the laser axis. It deflects the beam electrons such that they propagate along circles with the Larmor radius

$$r_g = \frac{\gamma m_e v_e}{e B_\perp} \approx \frac{\gamma m_e c}{e B_\perp} \tag{2.7}$$

where $B_\perp$ is the magnetic field of the spectrometer magnet, and $v_e \approx c$ under the

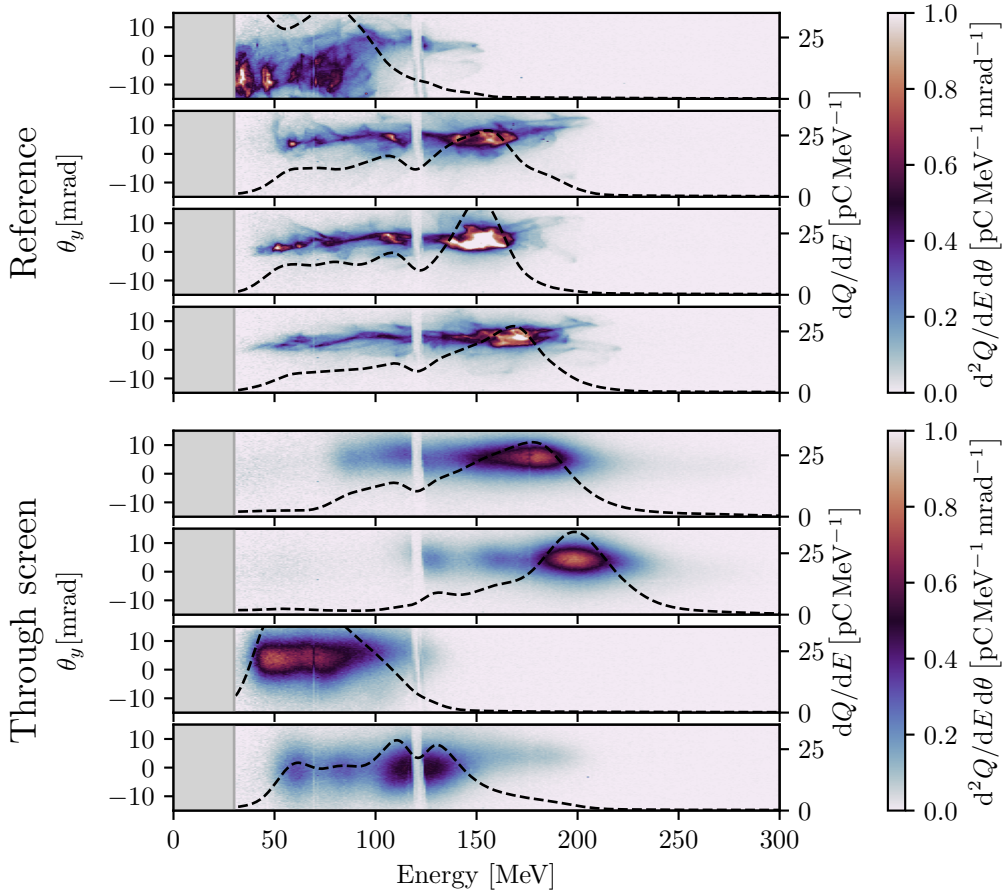

Figure 2.22: Influence of the pointing/divergence screen on the spectrometer signal. Shown are exemplarily four representative shows.

approximation of relativistic velocities. With this, the point of incidence of an electron at the scintillating screen can be calculated. However, imperfections in the magnetic field and edge fields make it suitable to use numerical approaches. Here, particle tracking simulations were used to map the energy to the screen position. Furthermore, the electron beam usually has a pointing jitter, which also needs to be considered. Figure 2.21b shows how the incidence of the electrons into the spectrometer and the energy translates to a position on the scintillating screen. Here, it was assumed that the beam always originates at the position of the target but has a variable vertical angle to the ideal laser axis, which results in a correlated angle and position deviation into the spectrometer. For an energy of 500 MeV, a beam pointing of 8 mrad results in an incorrectly measured deviation of approximately 100 MeV to the ideal pointing. Therefore, it is important to closely monitor and log the beam pointing to correct this error on a shot-to-shot basis.

For that reason, a pointing/divergence monitor was integrated into the setup, which consists of another scintillating screen in the direct electron beam path. It is located

20 cm upstream of the electron spectrometer and can be moved into the beam path with a motorized flipper. Unfortunately, it leads to a scattering of the electron beam, consequently washes out the signal in the spectrometer. Figure 2.22 shows exemplarily the influence of the pointing/divergence monitor on the spectrum. Even though the fine details are washed out, the overall shape of the spectrum is almost preserved.

The scintillating screens (Kodak BioMAX MS) in the spectrometer and the pointing/divergence monitor were calibrated in emitted photons per charge by Kurz [108, 109] with a conventional linear accelerator (Electron Linac for beams with high Brilliance and low Emittance, ELBE, at the Helmholtz-Zentrum Dresden-Rossendorf, HZDR). In order to remove the necessity of measuring/calculating the absolute photon yield from the screen to the camera chip, a reference light source in form of a gaseous tritium light source (GTLS) was attached to the scintillating screen to calibrate the photon yield. This allows to calculate the electron beam charge per pixel by dividing it to the total pixel counts of the GTLS and applying a conversion factor calibrated with the linear accelerator.

2.2.4 Few-Cycle Shadowgraphy

One of the essential diagnostics in this work is few-cycle shadowgraphy. It allows visualizing inhomogeneities of the plasma that happen even at relativistic speeds. This includes, in particular, plasma waves that are otherwise only accessible indirectly.

Shadowgraphy is a well-known tool for measuring volumetric fluctuations in refractive index, e. g., from density perturbations of gasses and fluids, and is frequently used for flow visualization. For plasma, the refractive index depends on the electron density (see equation 1.49). Light that propagates through inhomogeneous media thereby locally accumulates different phase shifts. These manifest themselves in an intensity variation after propagation, which can easily be observed with a camera. There are additionally techniques like interferometry and wavefront sensors that make the phase accessible, but they have less resolution and/or require more complicated setups or expensive equipment.

The basic principle of the shadowgraphy setup is to transversely probe the plasma. For that, the probe laser beam is propagated along the lateral direction of the LWFA drive laser through the interaction region. The probe will then accumulate locally varying phase shifts that lead to changes in the intensity profile, after several tens of micrometers, which we will refer to as *virtual image*. This virtual image is imaged with a magnifying optical system onto a camera.

In plasma acceleration, the extent over which the plasma is perturbed usually has a transverse size on the scale of the driver size. Assuming a simplified case where the perturbations can be considered as a thin slab (like a thin-lens approximation in optics), and the changes in intensity within the slab can be neglected. In this approximation, the slab with thickness $\Delta_y \ll d$ is assumed to be short to the distance d of the slab to the virtual image. The intensity distribution $I(x, z, y = d)$ in the virtual image can then

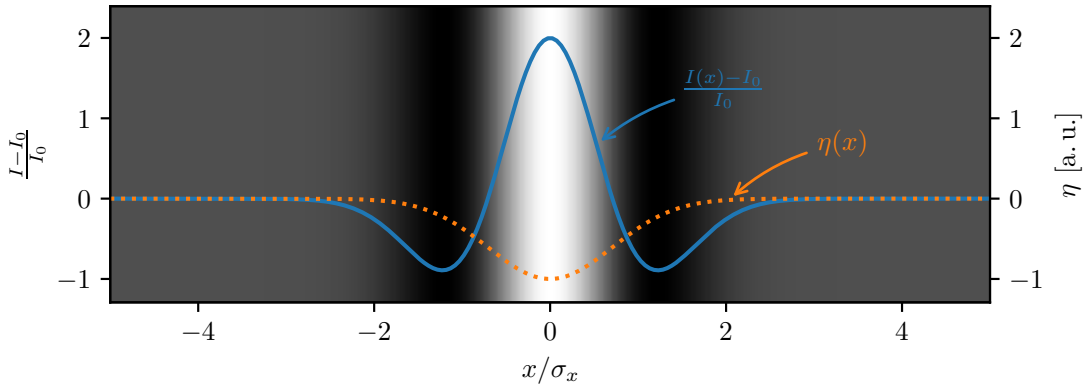

Figure 2.23: Shadow of a Gaussian refractive index distribution $\eta = e^{-x^2/\sigma_x^2}$ (dashed) with length $\Delta y = 1$. The blue line and the background shows the relative intensity from Eq. 2.9. The Gaussian refractive index focuses the incoming plane wave in its vicinity, resulting in an increased intensity in the center, whereas the regions from where the light is focused towards the center appear darker.

be calculated with[110]

$$\frac{I(x,z) - I_0}{I_0} = -d\left(\frac{\mathrm{d}^2}{\mathrm{d}x^2} + \frac{\mathrm{d}^2}{\mathrm{d}z^2}\right)\int_0^{\Delta y} dy\eta(x,y,z) \tag{2.8}$$

where I_0 is the initial (homogeneous) intensity before the slab, x and z are the coordinates transverse to the probe beam, and η is the refractive index. The change in intensity is thus given by the second transverse derivative of the projected refractive index. The coordinate system here was chosen such that it is compatible with the coordinate system of the accelerator, where the probe beam propagates along the y axis (lateral to the LWFA laser axis).

Consider a simple case where the sample is a thin slab with a Gaussian refractive index $\eta(x,y,z) = \eta(x) = e^{-x^2}$ ($\partial_y\eta = \partial_z\eta = 0$). Such a Gaussian refractive index comes from a Gaussian density variation under the assumption of small perturbations $n \ll n_{\mathrm{cr}}$ with respect to the critical density n_{cr}. Then, the intensity distribution becomes

$$\frac{I(x,y) - I_0}{I_0} = -2d\Delta y\left(1 - 2x^2\right)e^{-x^2} \tag{2.9}$$

which is illustrated in Figure 2.23. A negative density perturbation leads to a negative refractive index perturbation and thus an increase in intensity, i. e., it acts focusing and, in a simple picture, shifts intensity from the wings towards the center.

There is a key problem with capturing fast processes like the propagation of plasma waves, in the same way that capturing fast objects is demanding in photography. Usually, the exposure time t_{s} of the camera is reduced such that the object only moves by a

negligible distance $\Delta x = vt_s$ during the exposure. The achievable resolution of the acquired picture is given by this distance. Considering plasma waves with velocities $v \approx c$ and a wavelength of $\lambda_\mathrm{p} = 15\,\mu\mathrm{m}$, the maximum acceptable movement during exposure $\Delta x_\mathrm{max} = \lambda_\mathrm{p}/2$ may be defined as half a plasma wavelength. This results in a maximum exposure time of $t_\mathrm{s,max} = 25\,\mathrm{fs}$, which is far beyond the capabilities of conventional cameras. Few-cycle shadowgraphy solves this problem by shifting the requirement from the camera to the illumination. In other words, the exposure time of the camera can be kept at moderate levels, while now the illumination needs to be switched on and off on a femtosecond time scale, e. g., by using femtosecond lasers.

Shadowgraphy of plasma waves was first demonstrated by Buck *et al.*[57] by using part of the LWFA drive laser as illumination. In their case, it was already on a sub-10-fs duration, so it could directly be used as a probe beam. For the ATLAS (and for many other Ti:Sa systems) the pulse duration is closer to 30 fs, so it is not short enough to resolve details of the plasma wave. Sävert *et al.*[111] demonstrated that it is possible to still use such Ti:Sa pulses as probe beams by compressing them in a hollow-core fiber (HCF) compressor to below 10 fs.

Figure 2.24 shows the layout of the shadowgraphy and probe generation setup, which is based on the one used by Sävert *et al.*[111]. It was mainly built by H. Ding [112], L. Wildgruber and F. Daiber, and a detailed description can be found in [99, 100, 112, 113]. Here we will only outline the basic working principle.

A 1/2 inch elliptic mirror is used to pick off a small part of the LWFA drive laser for the probe generation. The pulse energy of approximately 100 mJ is reduced by using the reflection of an uncoated wedge, an ND filter, and an iris to 500 µJ, which is necessary for optimum operation of the spectral broadening in the HCF. It also requires a well-compressed pulse in the first place, so pre-compression is necessary to compensate for non-ideal compression of the LWFA driver and transmissive optics like the vacuum window. This is done by set of chirped mirror pairs and an adjustable wedge pair.

A spherical mirror focuses the pulse via two mirrors into the 120 µm-core-radius and ∼1 m-long HCF. It is located in a sealed tube with Argon at 500 mbar pressure and Brewster windows on both sides. The propagation of the laser through the fiber leads to self-phase-modulation (SPM), which results in spectral broadening. In our case, the spectrum after broadening was spanning approximately 400 nm to 1000 nm, which corresponds to a bandwidth-limited pulse length of sub-10 fs, hence the term *few-cycle*. The output of the HCF is divergent, so a spherical mirror is used to re-collimate and set the beam diameter to approximately 10 mm. As the SPM broadening results in a chirp, the pulse needs to be compressed, which is achieved by another compression stage consisting of chirped mirrors and a wedge pair. Flip mirrors can direct the beam before and after each compression stage into a FROG to measure the pulse duration. The few-cycle pulse can then be used to probe the interaction in the LWFA and PWFA stage.

In order to capture the interaction in the right moment, the delay between the probe and the LWFA drive laser (and the inherently synchronized PWFA electron driver) needs to be matched and adjustable on a femtosecond scale. The coarse synchronization is achieved by delaying the LWFA drive laser with folding mirrors inside of the vacuum chamber to approximately match the probe delay on a 10 cm-scale, and then adjusting

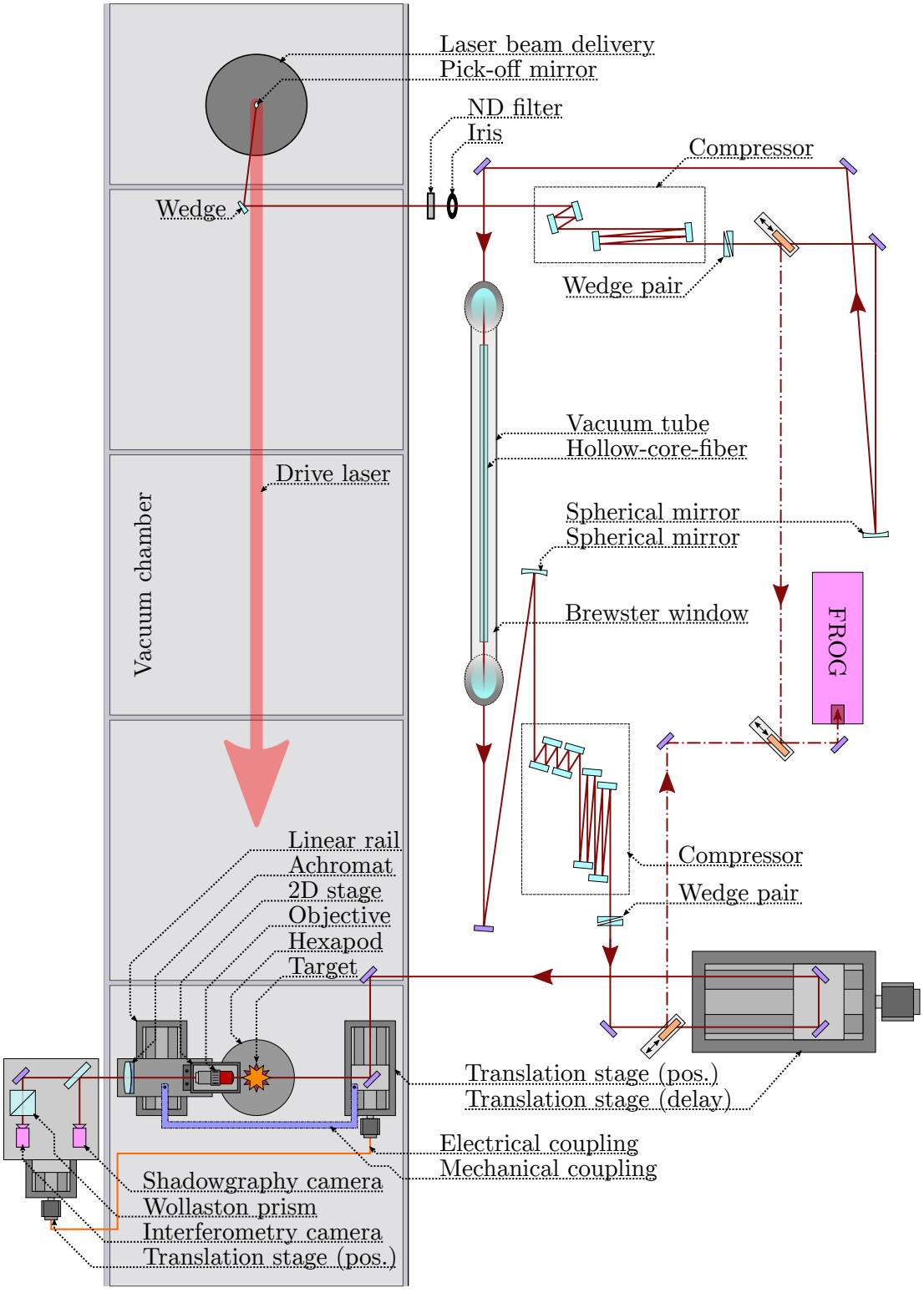

Figure 2.24: Schematic layout of the few-cycle probe generation and the shadowgraphy diagnostic.

the path of the probe to match the drive laser delay on a few-centimeter scale. A motorized optical delay stage is used to fine-adjust the delay with femtosecond resolution and nanosecond range.

The probe is then sent perpendicularly through the interaction, and subsequently imaged with an optical setup consisting of a microscope objective and an $f = 20\,\mathrm{cm}$ achromatic spherical lens to a camera. The objective is infinity corrected with $5\times$ magnification (assuming a 20 cm tube lens), has a numerical aperture of 0.14 (14 µm depth of field) and it is optimized for near-infrared. With a working distance of 3.75 cm it is sufficiently far away from the LWFA/PWFA interaction to not become damaged.

Since the LWFA and PWFA stage are up to several centimeters apart, the whole imaging setup and the first mirror before the interaction was made movable with translation stages (as shown in Figure 2.24). This way, the shadowgraphy can be moved over centimeter distances without changing the relative delay of the probe to the LWFA drive laser. The parts in vacuum and the parts in air are moved by two translation stages that were electronically coupled to move synchronously.

Generation of Synthetic Shadowgrams

In order to gain further insight into the processes in the LWFA and PWFA stage, particle-in-cell (PIC) simulations were performed. These allow access to the evolution of the plasma density, which in turn can be used to generate synthetic shadowgrams that the acquired shadowgrams can be compared to.

Previous studies on few-cycle shadowgraphy have used 3D-Cartesian PIC simulations with a separately initialized probe beam to simulate shadowgrams [114]. However, this approach becomes impractical for the large simulation windows required in our case. Instead, we generate synthetic shadowgrams from quasi-3D or radially symmetric 2D simulations in post-processing.

We use the electron distribution to calculate the phase shift of a plane monochromatic wave traveling perpendicularly through the moving plasma in a static approximation with the dispersion relation of a cold plasma. In the following, we choose $\boldsymbol{e}_z$ as the direction of the LWFA drive laser, $\boldsymbol{e}_y$ as the direction of the probe, and $\boldsymbol{e}_x$ as the vertical direction. In order to account for the movement of the quasi-static plasma wave, we numerically shift each density layer along the probe axis by the corresponding length it took the probe to reach this layer, such that the distribution appears to be moving with the speed of light as the probe propagates through it. Specifically, each $\boldsymbol{e}_{x|y}$ plane was shifted by $\Delta y = y - y_0$ in $\boldsymbol{e}_z$ direction, with y_0 being the center of the plasma wave.

While our results show good agreement with the shadowgrams observed in the experiment, it should be noted that there are a few limitations. First, it is only valid if the plasma wave is does not evolve significantly (in the co-moving frame) while the probe transverses it. This is usually the case in wakefield acceleration and for all situations treated in this study, but special cases such as wave evolution in steep density gradients would be an exception. Furthermore, the cold plasma approximation (i. e., the assumption that only the density variation is responsible for the change in refractive index) is strictly only valid for non-relativistic electrons. Especially within the plasma wave,

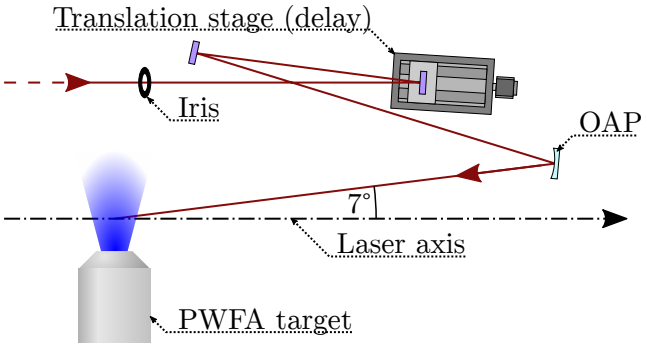

Figure 2.25: Sketch of the ionizer layout. The beam is reduced in energy by an iris, delayed via a motorized translation stage and focused with an off-axis parabolic mirror (OAP) under 7° to the counter-propagating LWFA drive laser. The left mirror and the OAP are motorized (not shown).

where even the non-trapped electrons can get relativistic, the diffraction can be overestimated due to the reduced refractive index of relativistic electrons. In the context of this work, the synthetic shadowgrams are not quantitatively compared to the experimentally acquired ones, and interpretations are not based on features that are strongly relying on the validity of these assumptions.

2.2.5 Ionizing Laser

Some of the experiments in this work require external ionization of the PWFA gas target when the LWFA drive laser is blocked by the foil. This is facilitated by the *ionizer* laser beam, which is derived from the LWFA drive laser. Figure 2.25 shows the layout of the optical setup (excluding a pick-off mirror and a motorized shutter). An iris was used to set the energy to 60 mJ by reducing the beam size to 10 mm diameter. The delay with respect to the LWFA drive laser was adjusted with a folding mirror on a motorized translation stage. An off-axis parabolic mirror focuses the beam into the PWFA stage under an angle of 173° to the LWFA drive laser. The focus was set to a position before the PWFA target in order to ionize over a large transverse area.

The delay between the ionizer and the LWFA drive laser was set such that the ionization happens after the LWFA-generated electron beam passes the foil, to reduce additional scattering from laser-induced processes like CFI[106], but before it arrives in the PWFA stage. The shadowgraphy is used to synchronize the LWFA drive laser, the ionizer and the probe. Figure 2.26 shows a shadowgram where the delays are set such that the ionization fronts of the LWFA driver and the ionizer are visible. Here, all three lasers are arriving approximately at the same time.

In other experiments, the ionizer beam had different functions, e. g., as a collider for optical injection and for X-ray generation via Thomson scattering, which are not a part of this thesis (see [62, 115, 116]).

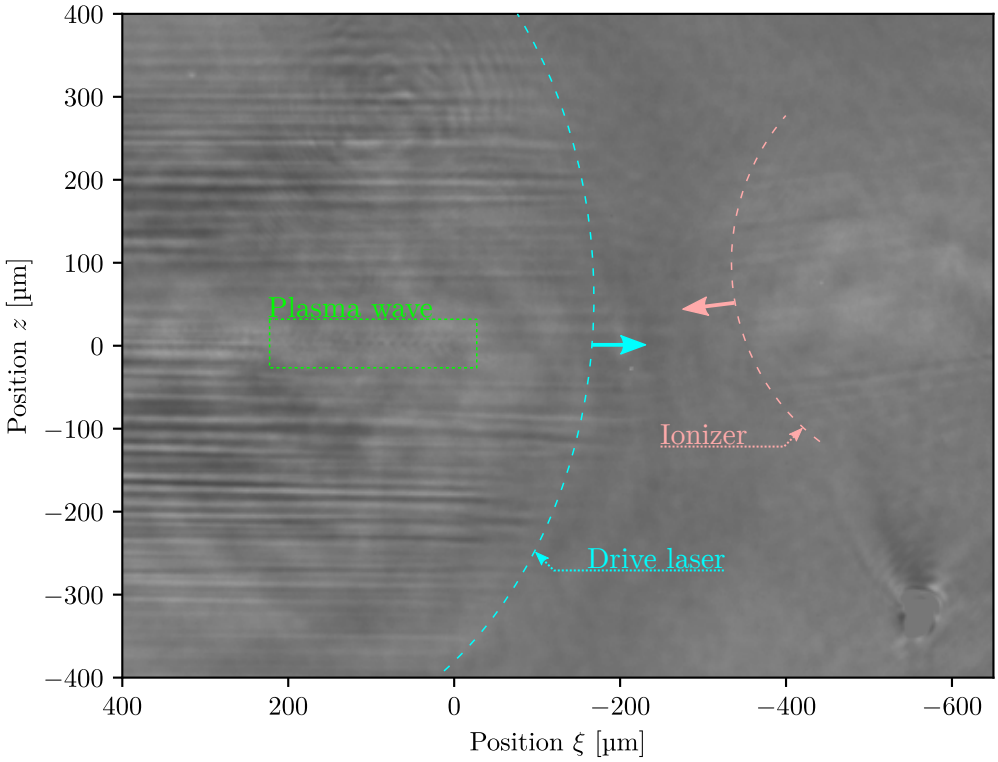

Figure 2.26: Shadowgram with synchronized LWFA driver, ionizer and probe. The dashed lines show the ionization fronts of the LWFA driver (cyan) and the ionizer (light red).

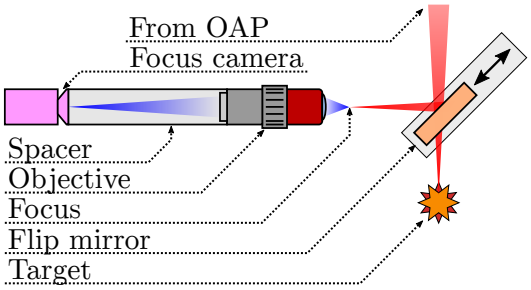

Figure 2.27: Sketch of the focus diagnostic. The LWFA drive laser comes from the top and is focused into the target in the bottom. When the flip mirror is moved in, the focus is guided towards the microscope objective, that images it onto the camera chip.

2.2.6 Laser Focus Diagnostic

The transverse intensity distribution of the drive laser focal spot has a significant influence on the performance of the LWFA process [117]. It is measured with an optical setup consisting of a 10× objective mounted with a ∼10 cm spacer on a camera, as shown in Figure 2.27. Instead of calculating the pixel size from the optical system, which is sensitive to errors, e. g., in the separation of the objective to the camera chip, it is calibrated by placing a grid mask with $d = 10\,\mathrm{mm}$ periodicity in the collimated beam before the focusing OAP. This creates diffraction orders at angles θ_m according to

$$d \sin \theta_m = m\lambda \tag{2.10}$$

with the laser wavelength $\lambda \approx 800\,\mathrm{nm}$ and the order m. With the focal length $f = 2.5\,\mathrm{m}$ of the parabolic mirror, the diffracted first order is in a distance of $l = f \arctan \theta_1 = 200\,\mu\mathrm{m}$ to the zeroth order. This length serves as a reference to calibrate the pixel size.

The focal spot is measured at nominal laser power with inserted attenuator and filters. The intensity distribution can be acquired over a range of six orders of magnitude by combining images from different filter settings with different levels of saturation. Here, the attenuator was adjusted such that in combination with a total filter of ND3, the intensity maximum is slightly below saturation. Three more images with ND2, ND1 and ND0 are then acquired, which are correspondingly saturated in the center of the beam. Figure 2.28 shows such a combined image with logarithmic and normal scale. Due to shot-to-shot fluctuations in the focal spot position, an algorithm was used to find the best overlap by maximizing the cross correlation of each image with the next higher filtered image.

The ATLAS 300 allows optimizing the focus by (pre-) compensating the wavefront with the adaptive mirror. This was done throughout the experiments to compensate for temperature drifts and other sources of perturbations. Figure 2.28 shows a typical focus after optimization. It is slightly elliptical because of an elliptical shape in the near field, and has a transverse size of 28 µm and 32 µm FWHM in both axes. The calculation

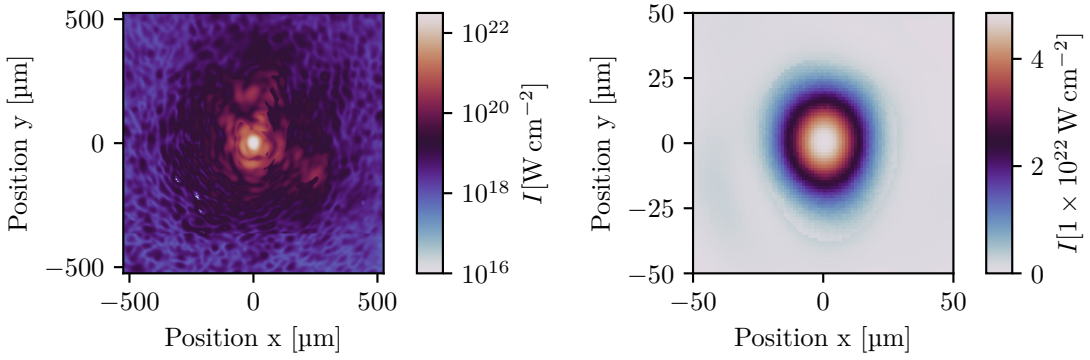

Figure 2.28: Typical vacuum focus after optimization with the adaptive mirror and focusing parabolic mirror orientation. The logarithmic plot on the left and the (non-logarithmic) plot on the right show the intensity in a wide area and in the close vicinity of the focus, respectively. The calculated intensity values assume a Gaussian pulse duration with 30 fs FWHM and a total energy of 2.5 J.

of peak intensity and power also require the knowledge of the total energy and pulse length. Assuming a pulse length of 30 fs and total energy of 2.5 J (as suggested by the measurement of the pulse energy of 6 J before compression and the measured transmission towards the target of ∼40 %), the peak intensity and peak power are 4.8×10^{18} W cm^{-2} and 80 TW, respectively. The ratio of energy contained within the first Airy disk is found to be 60 %.

Chapter 3

Plasma Waves Driven by Laser-Accelerated Electrons

— Is that a plasma wave or just dust?

Prior to the studies presented in this work, several experiments gathered evidence that LWFA-generated electron beams can drive plasma waves [59–61] with indirect observations. In a first step, we tried to verify this assumption with greatly improved LWFA performance and few-cycle shadowgraphy, that allows a direct observation of plasma waves. In a second step, we tried to achieve actual acceleration with the hybrid scheme.

In the following, we will discuss three individual experiments that show the most important observations and conclusions we drew from the transition from a pure LWFA towards a hybrid accelerator.

In a first experiment, we placed an additional gas jet a few millimeters downstream of the LWFA stage, such that it can provide the necessary plasma background for the PWFA process. This second target is from now on referred to as *PWFA stage*. Under certain configurations, we indeed observed plasma waves that appear to be electron-driven. One apparent flaw of this approach is the chance that a part of the remaining LWFA drive laser might re-focus and drive a plasma wave, which may be mistaken for an electron-driven one. However, especially the case where both types of waves are visible revealed a distinctive difference of laser- and electron-drivers.

We performed a second experiment to rigorously rule out any possible influence of the remaining laser and prove the unambiguous existence of plasma waves driven by LWFA-generated electron beams. This was achieved by blocking the laser between both stages with a foil.

In a third experiment, witness bunches were injected and accelerated in the electron-driven plasma waves. For this, we tuned the LWFA process to create a pair of two electron bunches by injecting into two subsequent cavities of the plasma wave. These were then used as a driver-witness-pair in the PWFA stage.

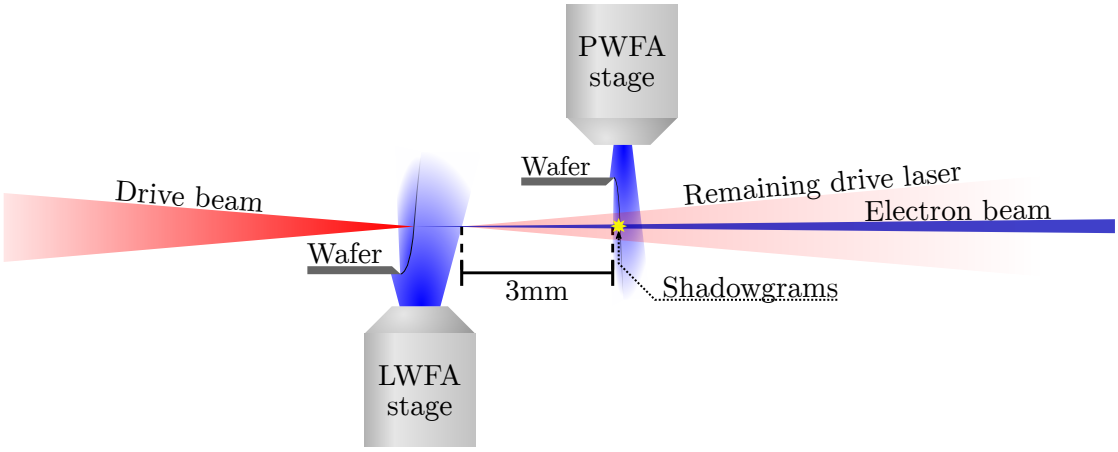

Figure 3.1: Sketch of the setup of the *first* experiment. The LWFA stage consists of the Laval 3000 nozzle with 3 mm orifice diameter, and the PWFA stage of the Laval 1000 nozzle with 1 mm orifice diameter. In order to have free sight with the probe (pointing into the observer plane in this sketch) and to achieve such a small separation, we placed both jets anti-parallel, i. e., the LWFA jet pointing upwards and PWFA jet downwards.

3.1 Observation of Double Plasma Waves

A relatively straightforward first step to verify whether the LWFA-generated driver is able to drive a plasma wave is to place a second gas target (i. e., the PWFA stage) downstream of the LWFA stage in a few millimeter distance. Both beams propagate freely through the vacuum gap, which results in an increase in beam sizes and consequently a reduction in drive strengths. Even though this is an unwanted effect for the electron beam, it may be a necessary one for the laser, as the intensity even after depletion in the LWFA stage might still be strong enough to drive a non-negligible plasma wave. At the exit of the LWFA stage, the typical electron beam divergences in our experiments are on the order of 1 mrad FWHM, whereas the divergence of the spent LWFA drive laser was found to be similar to the in-going beam that has a divergence of 40 mrad. Consequently, the laser diffracts much faster than the electron beam diverges, so the drive strength of the laser drops much faster than the one of the electron driver. However, the quantitative estimation of the drive strengths in the PWFA stage requires beam parameters like the emittance that are still inaccessible in our setup.

Figure 3.1 shows the sketch of the target configuration in which we observed plasma waves in the PWFA stage. Here, the LWFA stage consists of the Laval 3000 (see 2.2.1) supersonic nozzle with 3 mm orifice diameter in combination with a silicon wafer to facilitate shock-front injection. After careful optimization, we were able to generate electron beams with a charges of (381 ± 55) pC above 100 MeV, centered around (334 ± 33) MeV (weighted mean above 100 MeV) and with divergences of (0.48 ± 0.07) mrad FWHM. Here, the available laser energy was 5.0 J before compression, resulting in a peak

power of ∼70 TW. The interaction axis was set to 2 mm above the nozzle outlet, where a plasma density of $3.2 \times 10^{18}\,\mathrm{cm}^{-3}$ was inferred from shadowgraphic measurements.

The PWFA stage consists of the Laval 1000 supersonic nozzle with 1 mm orifice diameter. It is placed downstream of the LWFA stage with a vacuum gap of approximately 3 mm. Assuming an initial transverse and longitudinal electron beam size of 10 µm FWHM ($\sigma_{r_0} = \sigma_\xi \approx 4.2\,\mu\mathrm{m}$), the estimated size at the beginning of the PWFA stage is $\sigma_r = \sqrt{\sigma_{r_0}^2 + \sigma_{\mathrm{div}}^2} = 11\,\mu\mathrm{m}$. This results in a maximum bunch density of $n_b = 1.9 \times 10^{18}\,\mathrm{cm}^{-3}$. The PWFA stage was operated with a shock-front, which was supposed to facilitate injection into the beam-driven wakefield. Even though a low-energy peak appears in the spectrum as shown in Figure 3.2, the uncertainty of the influence of the spent LWFA drive laser as well as whether these electrons are injected in the PWFA stage or a decelerated part of the PWFA drive bunch do not allow a conclusive interpretation, and this part of the experiment is not relevant here. The peak density at the position of the observed plasma waves, which is close to the shock, was measured to be $1.9 \times 10^{19}\,\mathrm{cm}^{-3}$, and is therewith an order of magnitude higher than the estimated density of the electron beam. Still, the electron beam density may strongly increase due to self-focusing after some propagation.

Figure 3.2 shows the electron bunch parameters from the LWFA stage and the influence of the PWFA stage. As soon as the PWFA stage gas jet is enabled, there is a strong broadening of the electron spectrum towards low energies, which is in agreement with previous measurements by Chou [118], so the effects on the electron beam are consistent with what is expected from acting as a plasma wave driver. Also, there is a substantial decrease in charge detected by the spectrometer by almost 80 %. Throughout our measurements, we found a loss of driver-charge to be a common effect of the PWFA stage in almost every configuration. The reasons generally can be manifold and still need to be studied in detail. Here, it is likely a combination of an increase in divergence and strong energy depletion.

In this configuration, shadowgraphy indeed shows plasma waves in the PWFA stage. The reason why this particular configuration is so interesting is that it actually shows signatures of two individual plasma waves, as shown in Figure 3.3. Here, the apparent disadvantage of still having a possibly strong remaining LWFA drive laser is that each wave can potentially be driven by the LWFA-generated electron beam or the laser. Especially this uncertainty made one important observation possible: The shadowgrams show a conical diffraction feature trailing the upper plasma wave, but not the lower one. This means that there appears to be a difference in both plasma waves, and one obvious possible difference may be the kind of driver. We never observed such a feature in the LWFA stage, so this led to the assumption that the conical feature may be an indicator for particle-driven plasma waves. This interpretation can also explain the spatial separation, as previous experiments showed that the pointing of the laser and the electron beam from an LWFA stage are not necessarily collinear [92]. An in-depth discussion of this assumption and the mechanism leading to the formation of the diffraction feature will be given in chapter 4. As we will show, this observation eventually led to the studying of the ion dynamics, which is a fundamental process in PWFA that has not yet been

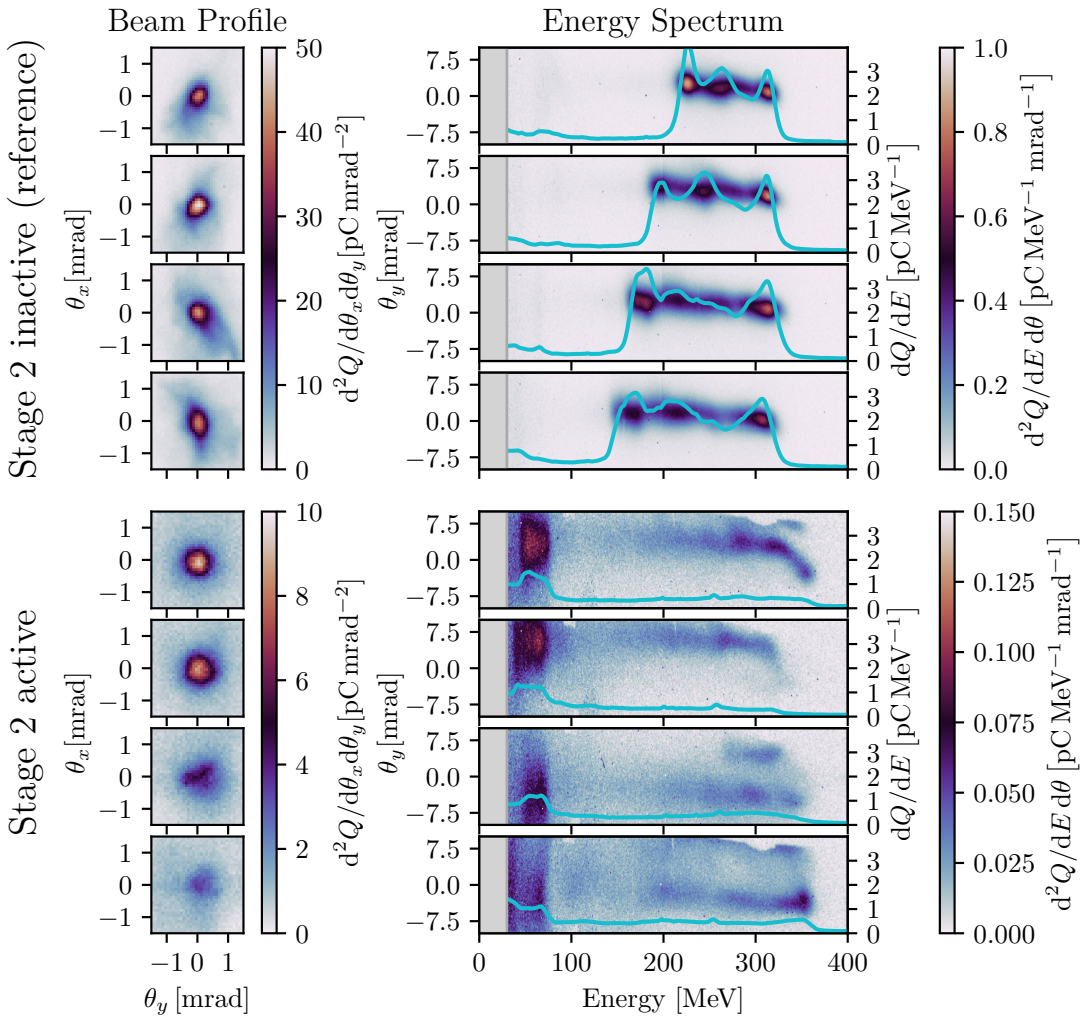

Figure 3.2: Spectrum of the electron beam with inactive (top) and active (bottom) PWFA stage. Shown here are four consecutive shots each. The apparent correlation of the energy spread in the reference case is a coincidence.

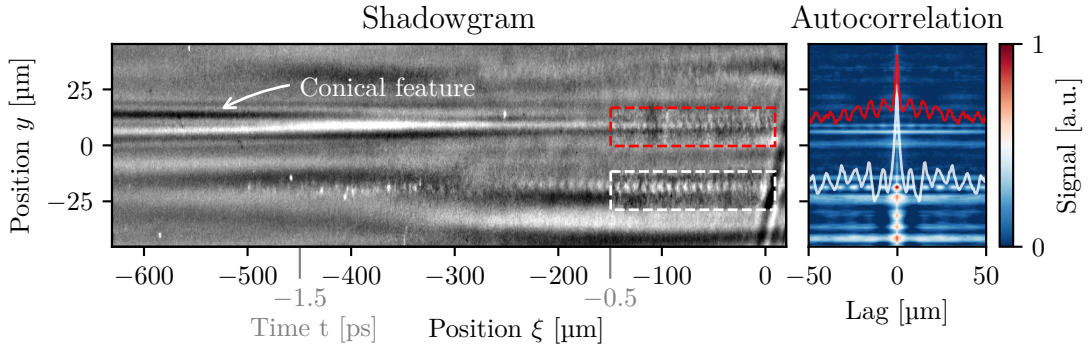

Figure 3.3: Shadowgram of the PWFA stage (left) with a particle- and laser-driven plasma wave (red and white boxes) and line-by-line autocorrelation (right) with lineouts at the positions of the plasma waves (red and white curve). The direction of propagation is to the right.

experimentally studied in conventional particle-driven wakefield accelerators itself.

In the following section, we will focus on eliminating the uncertainty of a possible influence of the spent LWFA drive laser.

3.2 Observation of Purely Particle-Driven Plasma Waves

The observation of the double plasma waves with the conical diffraction feature was already promising evidence for beam-driven plasma waves, but the available measurements do not permit an unambiguous identification of the type of driver at this point.

In order to prove that the LWFA-generated electrons can drive plasma waves, we carried out a *second* experiment where the influence of remaining laser can be ruled out. The most rigorous way to achieve this is blocking the laser between the LWFA and PWFA stage, e. g., with a thin foil that acts as a plasma mirror. This way of blocking of the spent LWFA drive laser, however, comes with several disadvantages. The first one is from a mechanical point of view. Having a foil between the jets will create additional constraints on the setup, such that – in our case – the stage separation needed to be increased. This will result in a longer vacuum propagation and consequently increased electron beam size, which in turn results in a decreased drive strength. The second reason is the increase in electron beam divergence due to scattering at the foil (see Section 2.2.2). Our measurements show that in this particular configuration the divergence of the electron beam is increased by a factor of ~ 2.5 when the foil is inserted into the beam path. This consequently also leads to a lower peak density and therefore lower drive strength. The third reason is that the gas of the PWFA stage is not ionized by the spent LWFA drive laser anymore, and now needs to be ionized either externally

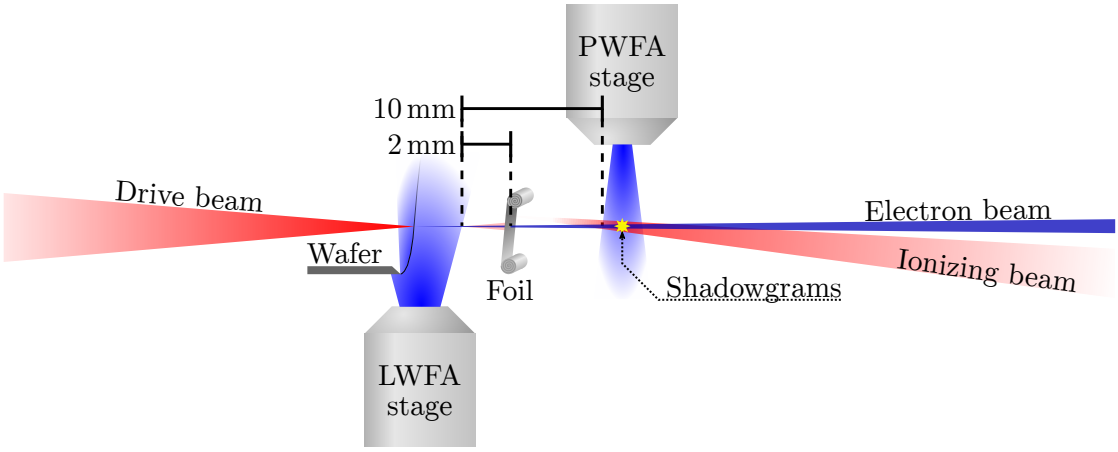

Figure 3.4: Sketch of the setup of the *second* experiment. The LWFA stage consists of the P5 nozzle with 5 mm orifice diameter, and the PWFA stage of the Laval 3000 nozzle with 3 mm orifice diameter.

or by the electron beam itself. Both of these cases are studied, and will from now on be referred to as the *pre-ionized* and *self-ionized* cases.

The (self-) ionization of the electron beam only occurs if the self-fields exceed the field ionization threshold. For atomic hydrogen, it is approximately $25\,\mathrm{GV\,m^{-1}}$ for an ionization rate of $1\,\%\,\mathrm{fs^{-1}}$. While the driver is strong enough to ionize hydrogen (as will be demonstrated later), the ionization process has a strong impact on the driver propagation and plasma wave generation. Consider an ultra-relativistic, radially symmetric beam. The Lorentz-boosted electrostatic fields will then be mainly transversal and vanishing on the symmetry axis due to its geometry. This means that the ionization directly on axis is suppressed, and the resulting annular ionization channel will lead to a reduced restoring force of the plasma electrons. Furthermore, there is no ionization at the front of the driver where the fields are below the ionization threshold, so the very front of the beam will not participate in the plasma wave generation.

In order to avoid these detrimental effects of self-ionization, the setup was extended with the ionizer beam for pre-ionizing the gas in the PWFA stage (c. f. Section 2.2.5). The focus of the ionizer was moved sufficiently far out of the PWFA target such that the ionization region is large and covers most of the interaction. The delay was set such that the gas is ionized several picoseconds before the electron beam arrives.

Figure 3.4 shows a sketch of the target configuration. Here, we incorporated the foil (c. f., Section 2.2.2) and the ionizer. Note, that the target configuration and correspondingly the LWFA and PWFA interaction is different from the first experiment. The electron beam divergence and spectrum after the PWFA stage in the self- and pre-ionized case, along with a reference shot (without foil and without PWFA stage) are shown in Figure 3.5. The reference shot has a charge of 892 pC at a mean energy of 170 MeV (each accounting for charges above 50 MeV). The divergence is found to be 1.8 mrad FWHM, which includes even the low energy part of the spectrum below 50 MeV. Here,

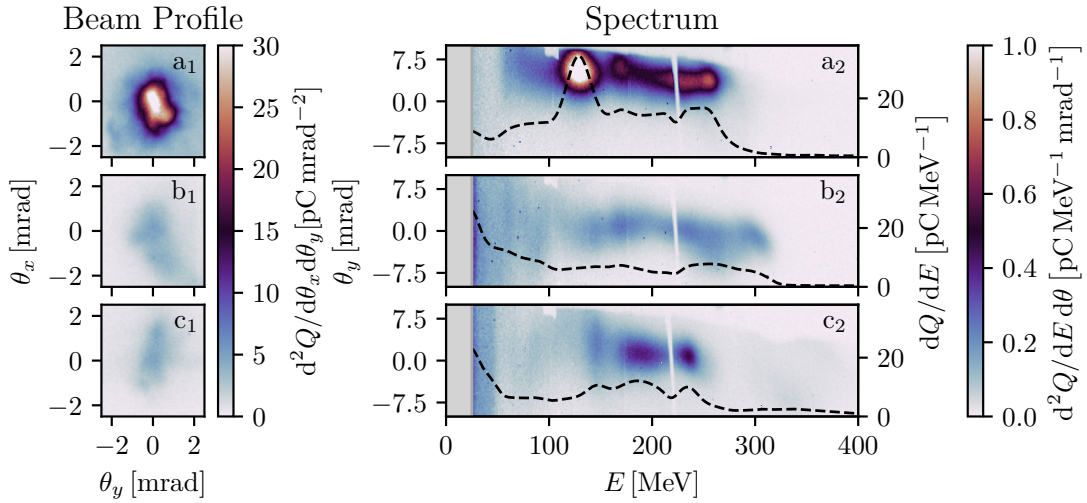

Figure 3.5: Electron beam profiles and pointing corrected spectra for the configuration in Figure 3.4. The divergence and spectrum in (a) show the LWFA reference without foil and without the PWFA stage, (b) shows the self-ionized case and (c) the pre-ionized case.

the P5 nozzle with 5 mm orifice diameter and 18 bar H_2 backing pressure was used. A plasma electron density of $2.9 \times 10^{18}\,\mathrm{cm}^{-3}$ was measured by analyzing the wavelength of plasma waves from shadowgrams. The foil was placed approximately 2 mm behind the exit of the jet. The PWFA stage consists of the Laval 3000 nozzle with 3 mm orifice. As soon as the foil is inserted and the PWFA stage is enabled, the charge drops to 470 pC while the mean energy remains almost constant at 180 MeV (each accounting for charges above 50 MeV), and the divergence increases slightly to 2.4 mrad for the self-ionized and pre-ionized cases.

Figure 3.6 shows three acquired shadowgrams in the center of the PWFA stage for the reference, the self- and the pre-ionized case. The reference (foil out and PWFA stage enabled) clearly shows the signature of a plasma wave in the area highlighted with the dashed rectangle. An autocorrelation over this area reveals the strong periodicity of the signal, which is equivalent to the averaged plasma wavelength. In this case, the wavelength is found to be $(13.2 \pm 0.2)\,\mu\mathrm{m}$, corresponding to a plasma density of $(6.4 \pm 0.2) \times 10^{18}\,\mathrm{cm}^{-3}$.

Once the foil is inserted and the LWFA drive laser is essentially blocked from the PWFA stage, the shadowgrams show horizontal diffraction features in the position where the plasma wave was previously observed in the reference case. As the LWFA drive laser is blocked by the foil, this features can only be attributed to the ionization channel of the electron beam. There is, however, no plasma wave visible, which is confirmed by the missing modulation in the autocorrelation. This allows the conclusion, that the electron beam exceeds the threshold of ionization, but that it does not drive a significant plasma wave. The diffraction features differ from the conical feature observed for the two plasma

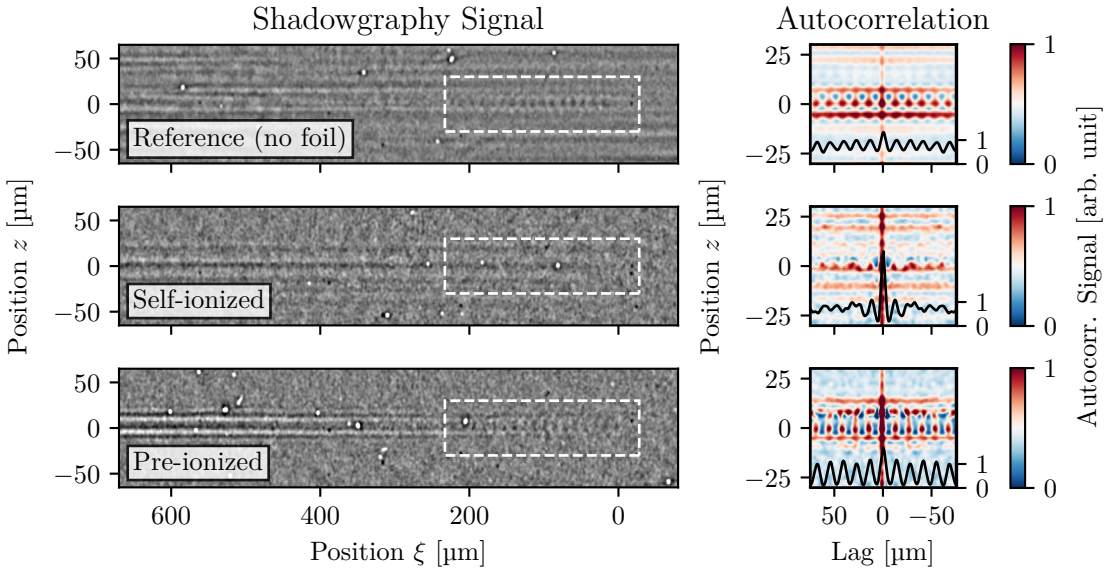

Figure 3.6: Shadowgrams of the PWFA stage for the self-ionized and pre-ionized case, and a reference case without foil. The reference shows a plasma wave which may or may not be driven by the electron beam. The self-ionized case shows ionization traces but no plasma wave. The pre-ionized case shows a plasma accompanied by a distinctive diffraction feature like the one observed in the first experiment.

waves in the previous experiment, as they are broader and not symmetric.

When the ionizer is enabled and the PWFA stage is ionized a few picoseconds before the electron beam arrives, the plasma wave re-appears in the shadowgram. This is confirmed by a strong modulation in the autocorrelation, from which a wavelength of $(13.6 \pm 0.3)\,\mu\text{m}$ can be inferred. This is in good agreement with the reference case. Not only the plasma wave is visible, but also the conical diffraction feature observed in the previous experiment.

In order to further verify our interpretation and understand the difference between the self- and pre-ionized case, we performed full 3D particle-in-cell simulations using OSIRIS 4.4 [119]. In order to reduce the computational cost, we only simulate the interaction in the PWFA stage. Therefore, we initialize the PWFA stage with either ionized or neutral hydrogen atoms with the measured density of $6.4 \times 10^{18}\,\text{cm}^{-3}$. The charge transmitted through the foil and PWFA stage consists to a large fraction of highly divergent and/or very low-energy electrons. For the modeling of the electron driver in the simulation, we thus only consider the energy interval of 100 MeV to 350 MeV, containing approximately 300 pC of charge. A beam size of $\sigma_r = 11.8\,\mu\text{m}$ at the beginning of the PWFA jet is geometrically estimated with the divergence of the reference shot and the divergence increase of the tape. The spatial momentum distribution is initialized with a temperature of 40 K and the correlation with the radius by the free drift towards the PWFA stage. The temporal bunch length is assumed to be 5 fs FWHM according to previous measurements [120].

The simulation is performed with a moving window with a size of $(x \times y \times \xi) = (60 \times 60 \times 20)k_p^{-3}$. A resolution of $\Delta x = \Delta y = \Delta\xi = 0.05k_p^{-1}$ is used, corresponding to approximately 0.1 µm for a plasma density of $6.4 \times 10^{18}\,\text{cm}^{-3}$. One macro-particle per cell is initialized for the electron beam and the plasma electrons each. Osiris employs a field ionization model [121] that is used in the self-ionization case, whereas in the pre-ionized case a fully ionized plasma is initialized.

Figure 3.7a shows the driver and background plasma density for the self- and pre-ionized case after 1.3 mm of propagation in the PWFA stage. In the case of self-ionization, the driver is not able to ionize in the center due to the rotational symmetry and the thus vanishing fields on the symmetry axis. There is a low-amplitude plasma oscillation visible, that may be regarded as a highly distorted plasma wave. In the case of pre-ionization, however, there is a low-amplitude plasma wave over the full size of the driver, along with a narrow, high-amplitude plasma wave in full blowout in the center. This comes from the tail of the bunch being focused in the low-amplitude plasma wave. The evolution of the driver throughout the PWFA stage is shown in Figure 3.7b. The divergence of the self-ionizing beam leads to a steady increase in size, whereas the driver in the pre-ionized plasma focuses for about one millimeter until the center of the beam eventually exceeds the background plasma density. From this point on, the high-density peak in the beam center drives a high-amplitude plasma wave.

Figure 3.8 shows a closer view of the driver. Comparing the second iteration (at $z = 650\,\mu\text{m}$) to the first one, the hollow part as well as the outer diameter of the channel becomes broader due to the beam constantly diverging and increasing in size. In the last iteration (at $z = 1300\,\mu\text{m}$), the overall shape of the ionization column is similar to the

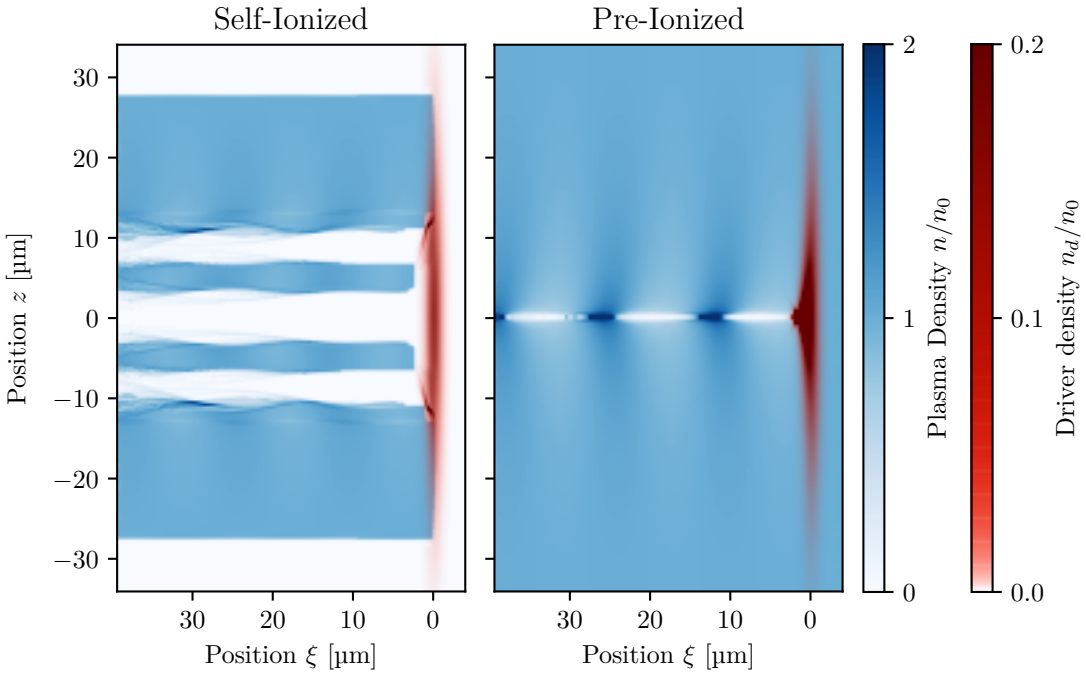

(a) Background plasma and driver density after 1.3 mm propagation in the PWFA stage. The self-ionized case leads to a complex ionization trace with a highly distorted plasma wave, whereas the pre-ionized case shows a low-amplitude plasma wave, which leads to ponderomotive self-focusing of the driver tail and a subsequent non-linear plasma wave in the center.

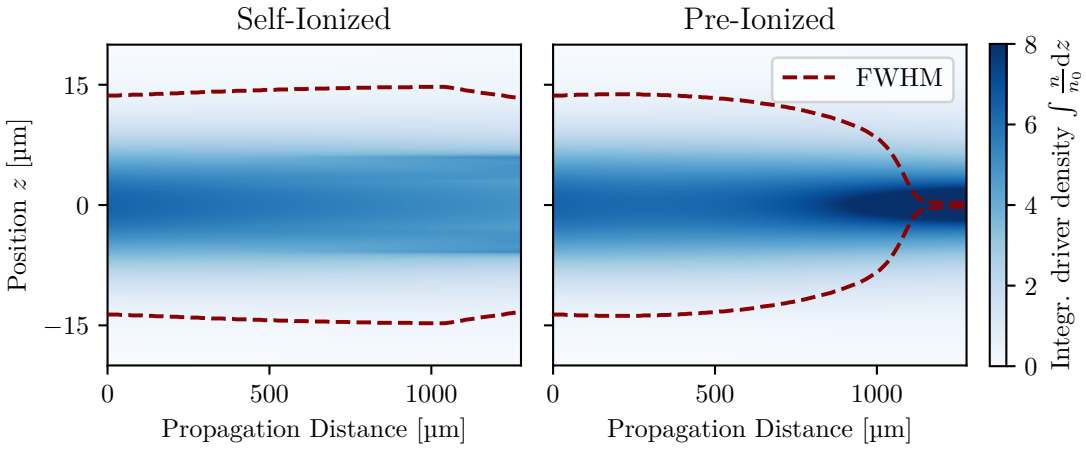

(b) Driver evolution in the PWFA stage for the self- and pre-ionized case. The plot shows the longitudinally integrated charge with respect to the propagation distance. In the self-ionized case, the driver does not change significantly, whereas in the pre-ionized case the driver self-focuses and exceeds the background plasma density after about 1 mm in its tail.

Figure 3.7: Simulation of the self- and pre-ionized case of the second experiment.

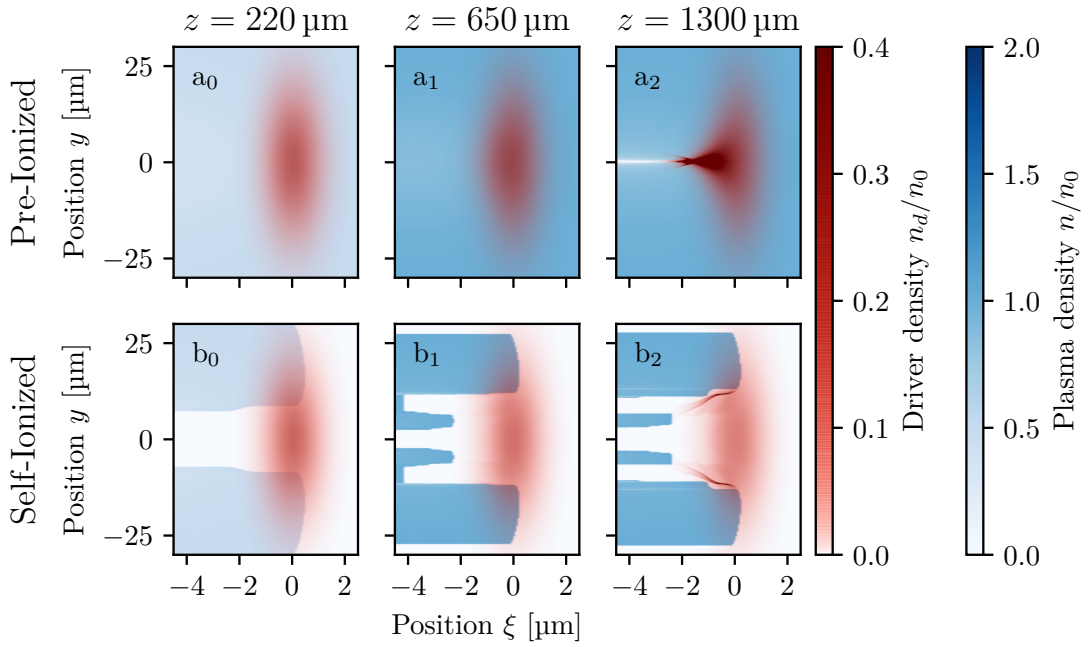

Figure 3.8: Driver and background plasma electron density after the propagation of 220 µm, 650 µm and 1300 µm in the self- and pre-ionized case.

previous one, but the beam shows local regions of increased density at approximately the rms radius due to the complex shape and evolution of the ionized region.

In conclusions, the simulations show that in the pre-ionized case the electron beam converges by ponderomotive self-focusing from the generation of an initially wide and low-amplitude plasma wave. After approximately 1 mm of propagation, this leads to a narrow and high-amplitude plasma wave driven by the strongly focused tail. They also show that the focusing force on the electron beam in the self-ionized case is not counteracting the natural divergence sufficiently. This is in very good agreement with the shadowgraphic observations.

This experiment is thereby the first demonstration of plasma waves driven by LWFA-accelerated electron beams, and is a first milestone. The next section will utilize such an electron-driven plasma wave to demonstrate acceleration of witness bunches.

3.3 Acceleration of Witness-Beams

We know from the previous experiment that the LWFA-generated electron beams can excite their own plasma waves. The next step towards the full hybrid scheme is to test whether we can use these plasma waves to trap and accelerate witness beams. For this, we carried out a *third* experiment that follows the proposed scheme of Hidding *et al.* [1]. Here, we generate pairs of electron beams in an LWFA stage by optimizing the injection

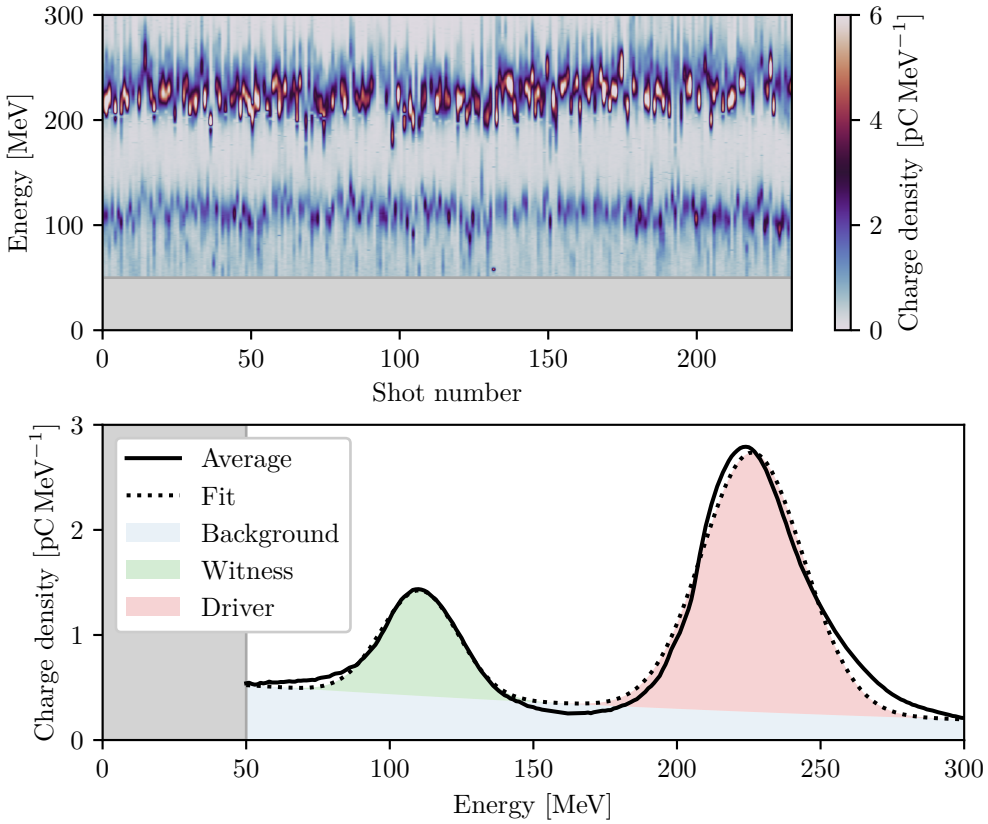

Figure 3.9: Driver/witness pair generation in the LWFA stage. The upper graph shows pointing-corrected spectra of 232 consecutive shots. The lower graph shows the averaged spectrum with a fitted sum of three Gauss functions. The blue, green and red areas show the parts of the fit that are attributed to the background, driver and witness, respectively.

mechanism to accelerate particles also in the second plasma wave cavity. These two beams are then propagated into the PWFA stage, where the leading beam from the first LWFA cavity drives a plasma wave, and the trailing beam from the second cavity takes the role of a witness. We measure the influence on the driver and witness energies at two different plasma densities in the PWFA stage, and thereby verify that the plasma wave is driven by the leading electron beam. We support this interpretation with the dependence of the acceleration with the driver charge, as well as with numeric simulations.

This is a proof-of-principle experiment that demonstrates two major concepts. First of all, we show the feasibility of accelerating electron beams in the PWFA stage, which is the first demonstration of electron acceleration with the hybrid scheme. Secondly, we show the feasibility of controlled injection of external witness beams into the PWFA with a high capture efficiency.

The first part of this experiment is the generation of the driver-witness pair in the LWFA

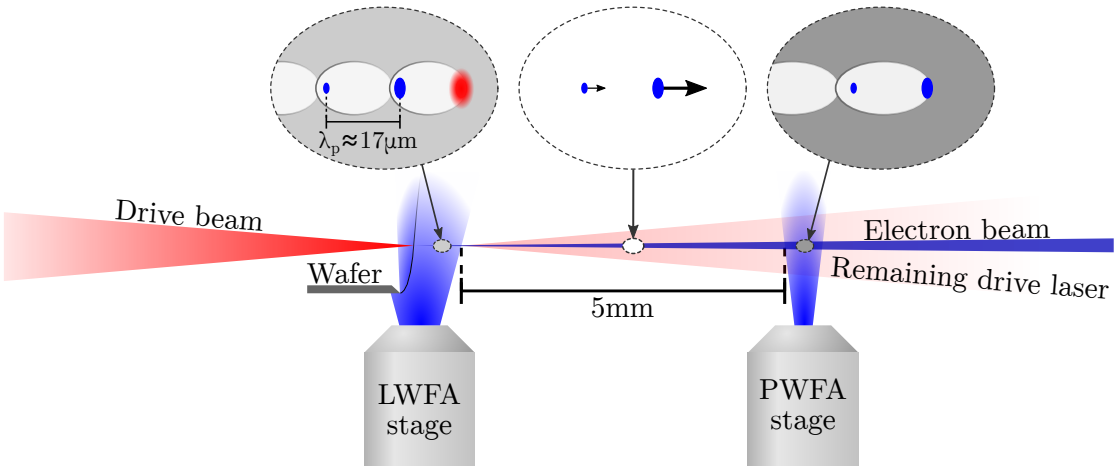

(a) Setup

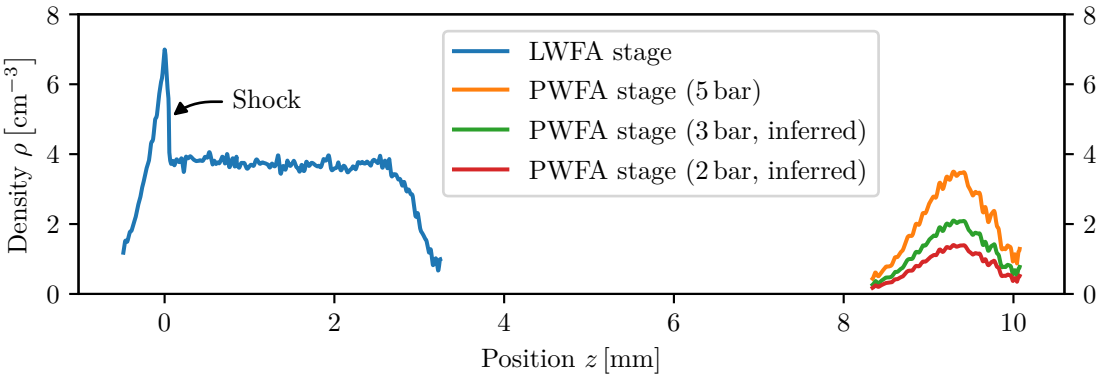

(b) Plasma electron density profile

Figure 3.10: Setup sketch and plasma density profile of the *third* experiment, in which a driver/witness pair is generated in the LWFA stage and used to drive and probe the PWFA interaction. The density profile was acquired from the interferometric phase shift (see Section 2.2.1). The measurement of the PWFA nozzle (orange) was performed at 5 bar (absolute) backing pressure, leading to a peak density of $3.5 \times 10^{18}\,\mathrm{cm}^{-3}$ density. The PWFA backing pressures used in this experiment are 2 bar (red) and 3 bar (green), and their peak densities are inferred from a linear scaling with the backing pressure.

stage. Like in the previous experiment, it consists of the P5 nozzle with a silicon wafer to facilitate shock-front injection, as shown in Figure 3.10a. It is operated with H_2 gas and 15 bar (absolute) backing pressure, resulting in an interferometrically measured electron plateau density of $3.8 \times 10^{18}\,\mathrm{cm}^{-3}$. With certain shock-front and laser focus positions, we were able to observe two distinct features in the electron spectrum at energies around 200 MeV to 250 MeV and 80 MeV to 130 MeV as shown in Figure 3.9. These high-energy and low-energy features can be attributed to the leading and trailing bunch, respectively, as will be supported later by numerical simulations. Their separation will approximately be the plasma wavelength of the density plateau, which is $\lambda_{p,\mathrm{LWFA}} = 17.3\,\mu\mathrm{m}$ in this case. In the following, we will refer to the leading bunch as *driver* and the trailing bunch as *witness*.

The LWFA stage generates an overall charge of (237 ± 43) pC in a range of 50 MeV to 300 MeV with a divergence of (1.4 ± 0.4) mrad FWHM. These are the combined beam parameters of the driver and witness, and some amount of charge that may or may not participate in the PWFA interaction. In order to quantify the individual driver and witness parameters, we assume that the spectrum consists of a sum of three Gaussian parts: the driver, the witness and a broadband background. The averaged spectrum along with fitted Gauss functions is shown in Figure 3.9. For the driver and witness parameters we only use the individual fitted Gauss functions and neglect the background. The Gauss fit of the driver corresponds to a charge of (109 ± 10) pC centered at (226 ± 1) MeV, whereas the Gauss fit of the witness corresponds to a charge of (34 ± 3) pC centered at (110 ± 1) MeV. Thus, the witness has approximately one third of the driver charge at half the energy.

This pair of driver-witness beam is afterwards propagated into the PWFA stage. In this experiment, we decided to remove the laser blocking foil, as especially the witness beam has a low energy and will therefore suffer strongly from the divergence increase. In order to reduce the influence of the spent LWFA drive laser, the separation of the PWFA stage was increased. Still, the laser is strong enough to ionize the PWFA stage, such that the ionizer was not used here. In the PWFA stage, the high-charge and high-energy driver may then excite a plasma wave that accelerates or decelerates the witness bunch depending on the phase it is located at. As the separation of both bunches is mostly given by the plasma wavelength in the LWFA plateau, a slightly lower density in the PWFA stage and thereby longer plasma wavelength will lead to the witness being located in the accelerating phase.

The PWFA stage consists of the Laval 1000 nozzle operated with H_2 gas. An interferometric density measurement at a backing pressure of $p_5 = 5$ bar (absolute) shows a peak density of $\rho_5 = 3.5 \times 10^{18}\,\mathrm{cm}^{-3}$. For the acceleration measurement, the PWFA stage was operated with two backing pressures of 2 bar and 3 bar, corresponding to peak densities of $1.4 \times 10^{18}\,\mathrm{cm}^{-3}$ and $2.1 \times 10^{18}\,\mathrm{cm}^{-3}$. This was inferred from the measured density at 5 bar by assuming a linear scaling with the backing pressure. These cases will be referred to as *low-density* and *high-density*, in the following. The corresponding plasma wavelengths are 28.2 µm and 23.4 µm, so the witness (with a separation of approximately 17 µm) can be expected to fit into the accelerating phase of the first cavity in both cases.

As soon as the PWFA stage is activated, there is a clear influence on the driver and

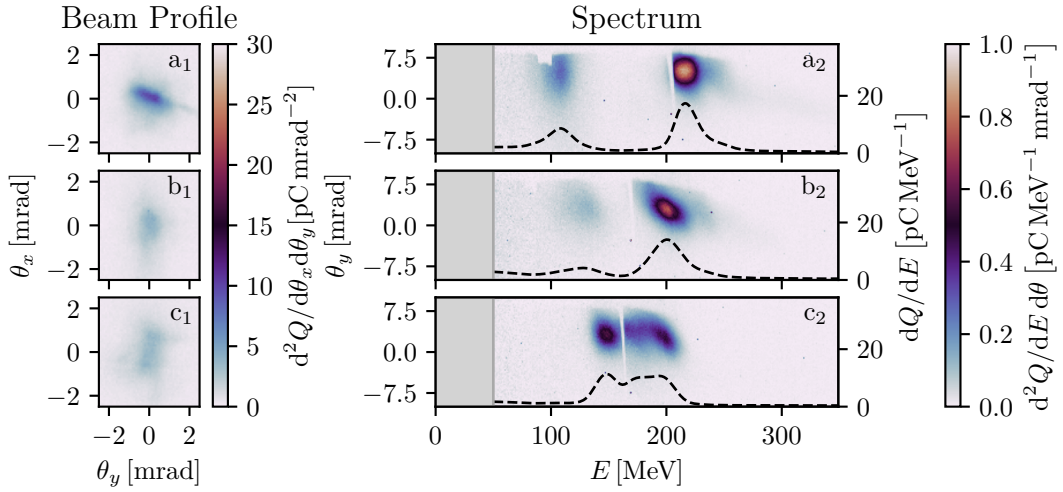

Figure 3.11: Influence of the PWFA stage on the divergence and spectrum in the *third* experiment. The top row shows the reference case, the middle row the low-density case and the bottom row the high-density case. The measurements presented here are the first acquired measurement of each case, respectively.

witness bunches. Figure 3.11 shows one beam profile and spectrum of each case. Both the low- and high-density cases show an energy loss of the driver and an energy gain of the witness. Furthermore, this effect appears to be stronger for the high-density case.

In total, we gathered data from approximately 200 shots for the reference and low-density case, and 50 shots for the high-density case. The averaged spectra are shown in Figure 3.12. Here, the difference between the high-density and low-density case is not a significant shift of the spectral peaks like between the reference and low-density case, but a broadening towards higher/lower energies. This is likely due to high shot-to-shot fluctuations in the PWFA process. As before, the averaged spectra were fitted with a sum of three Gauss functions that are assumed to represent the driver, witness and a background that does not participate in the PWFA interaction. Figure 3.13 shows the correlation between density and the energy gain of the witness and energy loss of the driver. It clearly shows that for higher plasma densities the witness experiences a higher acceleration and the driver a higher deceleration. The witness experiences an average energy gain of $(12 \pm 1)\,\mathrm{MeV}$ and $(19 \pm 1)\,\mathrm{MeV}$ within the PWFA stage for both cases, respectively. Considering an acceleration length of approximately 1 mm, this corresponds to accelerating fields in the range of $10\,\mathrm{GV\,m^{-1}}$ to $20\,\mathrm{GV\,m^{-1}}$.

Furthermore, the capture efficiency can be estimated by comparing the remaining charge in the witness after the acceleration in the PWFA stage to the reference case. Here, the charge drops from initially $(33.5 \pm 2.5)\,\mathrm{pC}$ to $(21.6 \pm 1.3)\,\mathrm{pC}$ and $(16.9 \pm 0.6)\,\mathrm{pC}$ in the low-density and high-density case, which corresponds to capture efficiencies of 65 % and 50 %, respectively.

In order to additionally verify the interpretation, start-to-end simulations from the be-

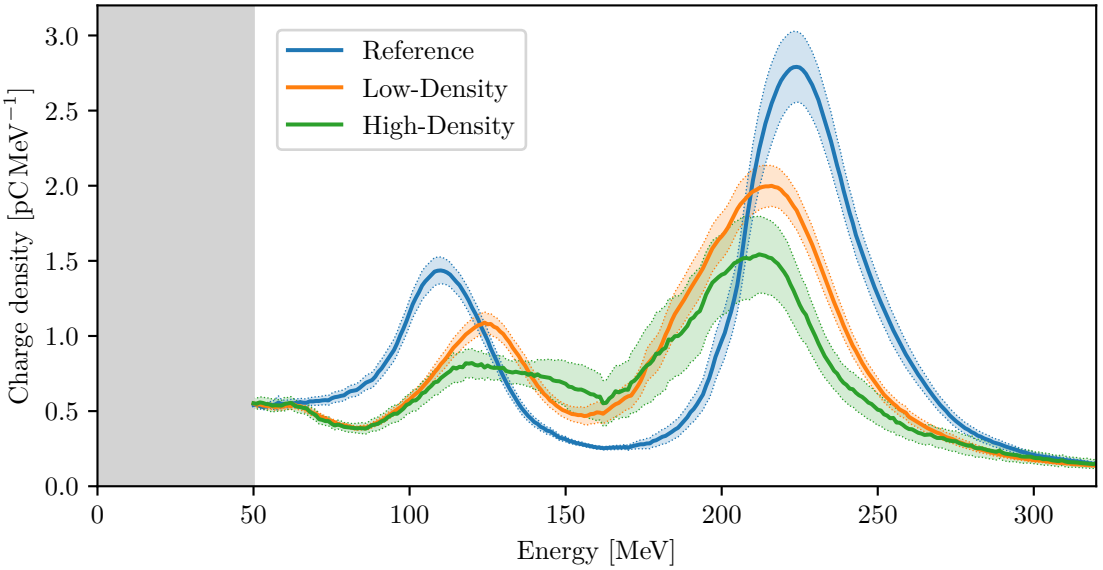

Figure 3.12: Mean spectra of the reference, low-density and high-density case with 95 % confidence interval. The low-density case shows a deceleration of the driver bunch (the high-energy peak) and acceleration of the witness bunch (the low-energy peak). In the high-density case, these broaden towards higher/lower energies and start overlapping.

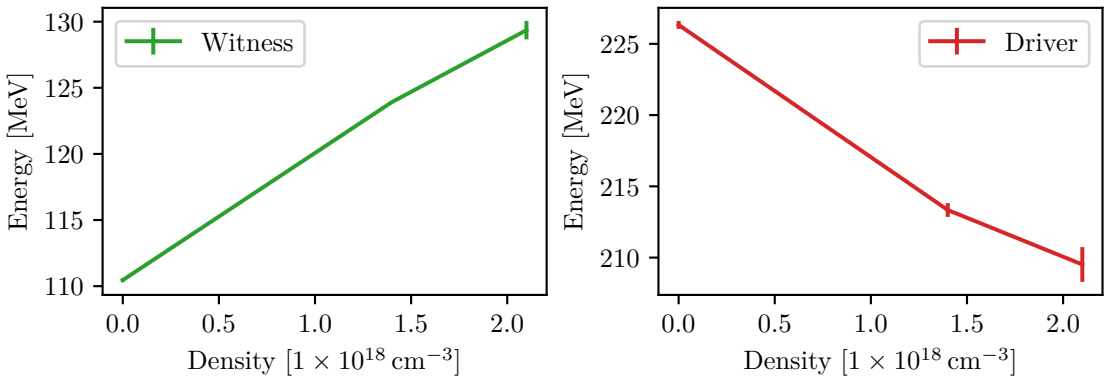

Figure 3.13: Averaged energy of the witness and driver with respect to the plasma electron density in the PWFA stage. The data at zero pressure is the reference case with the PWFA stage disabled, whereas the low-density and high-density case constitute the data points at a density of $1.4 \times 10^{18}\,\mathrm{cm}^{-3}$ and $2.1 \times 10^{18}\,\mathrm{cm}^{-3}$, respectively.

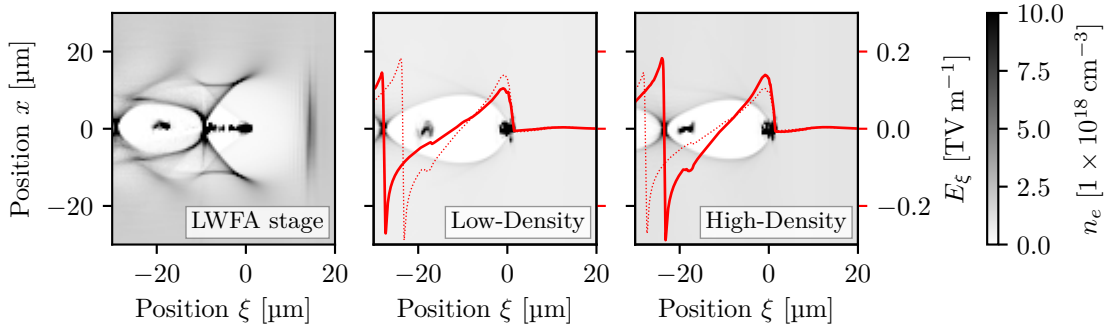

Figure 3.14: Plasma densities and longitudinal electric fields of PIC simulations in the LWFA stage and the PWFA stage in the low-density and high-density case. The dotted lines show the electric fields of the respective other case, for comparison.

ginning of the LWFA stage to the end of the PWFA stage were performed by J. Götzfried *et al.* [62]. Details on the numerical methods and further analysis can be found in [62], here we will only briefly discuss the overall behavior of the interaction. Figure 3.14 shows snapshots of the plasma density in the LWFA stage, and in the PWFA stage for the low-density and high-density case. The simulation generally reproduces the behavior we see in the experiment. Firstly, the shock-front injection in the LWFA stage leads to the trapping and acceleration also into the second cavity, which creates the driver-witness pair. Their separation of 17.5 µm is close to the LWFA stage plateau density. It also reproduces the observed spectrum, although the driver and witness energies are slightly higher than observed in the experiment. This is likely caused by over-estimating the drive laser strength, which however does not change the overall behavior significantly. The propagation towards the PWFA stage leads to a decrease in laser vector potential from $a_0 = 3.2$ at the exit of the LWFA nozzle to below 0.6 due to diffraction, and it does not re-focus significantly in the PWFA stage. Consequently, the middle and right panel of Figure 3.14 only shows a very weak electric field (red line) ahead of the drive electron bunch. In contrast, the drive bunch drives a strong plasma wave in full blowout, and in both cases the witness bunch is located in the accelerating phase. It also shows that the accelerating field strength in the low-density case is lower than in the high-density case mostly because the witness bunch is located closer to the center of the cavity.

The scaling of the witness acceleration to the driver charge further supports the interpretation of a PWFA process. For this, we sort the acquired spectra by charge, as shown in Figure 3.15. This already visually reveals a correlation between the total charge and the amount of deceleration of the driver beam. Further analysis also shows a clear correlation between the witness acceleration to the driver charge, as well as a correlation with the PWFA stage plasma density. Figure 3.16 shows the energies of the driver and witness spectral peaks with respect to the combined charge. Here, the combined charge is used, as the evaluation of the pure driver charge for the non-averaged shots is

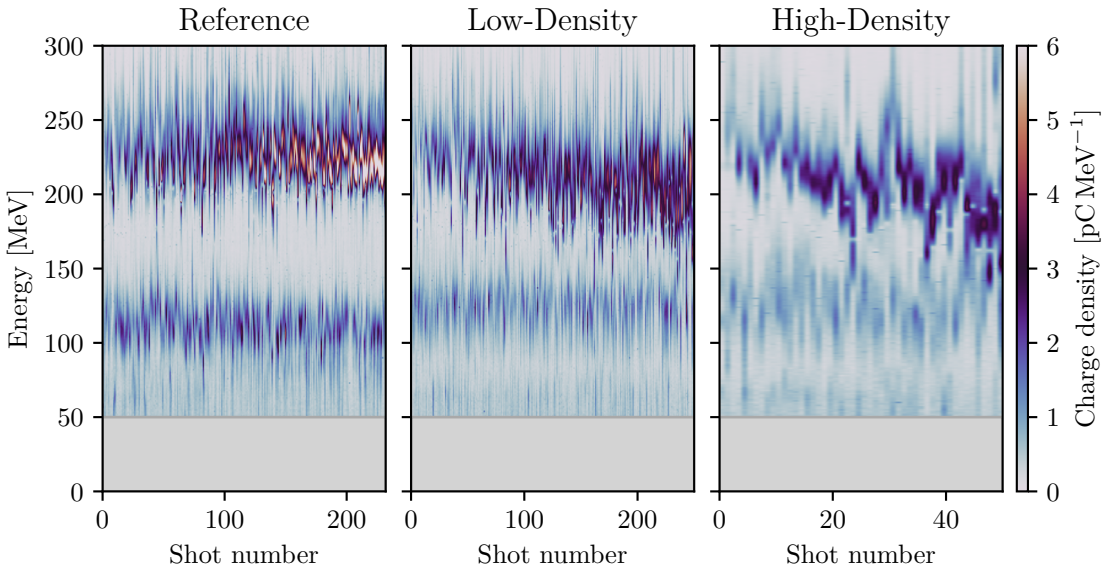

Figure 3.15: Individual spectra of the reference, low-density and high-density case. The spectra are sorted by the total charge to demonstrate the charge dependence.

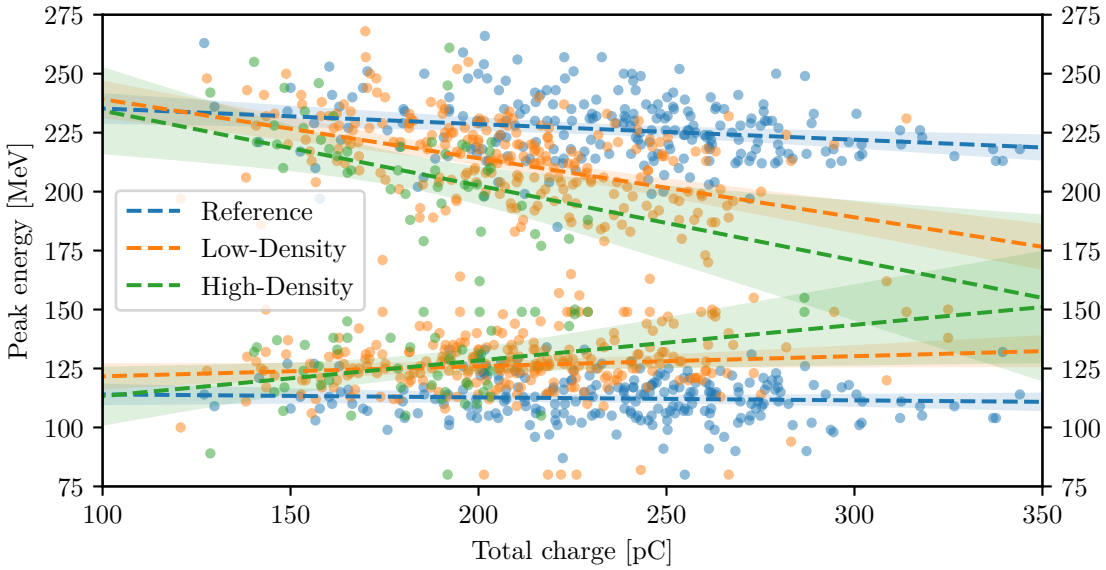

Figure 3.16: Charge dependence on the energy of the driver (high-energy) and witness (low-energy) spectral peaks for the reference, low-density and high-density case. The dashed lines show linear fits with the 95 % confidence interval. For increasing PWFA plasma densities, the driver experiences a stronger dependence of deceleration with respect to the charge, while the witness experiences a stronger acceleration for increasing charge.

significantly dependent on the methods used because of high shot-to-shot fluctuations. For the reference case, i. e., the pure LWFA beams without interaction in the PWFA stage, the driver energy decreases slightly with increasing charge, which is typical for beam-loading [62]. However, the witness energy is almost independent. As soon as the PWFA stage is activated, the driver energy significantly decreases for increasing charge, and now also the energy of the witness scales with the total beam charge. This scaling is expected for the PWFA mechanism, as a driver with higher charge drives a higher amplitude plasma wave and thus generates stronger accelerating fields.

3.4 Summary

In this chapter, we demonstrated the experimental steps leading towards the first proof-of-principle realization of a hybrid accelerator.

The goal of the first experiment is to use LWFA-generated electron bunches to drive plasma waves in a second plasma stage located few millimeters downstream of the LWFA stage. Here, the spent LWFA drive laser is still strong, so the electron beam as well as the laser might both drive plasma waves. Indeed, two waves with different signatures are observed with the few-cycle shadowgraphy. This led to a first evidence that the LWFA-generated electron bunches are capable of driving their own plasma waves, and the assumption that the laser- and electron-driven plasma waves may have different signatures in shadowgrams. This experiment also led to the observation and first study of the ion motion in a PWFA, as will be discussed in the next chapter.

The second experiment demonstrates for the first time unambiguously plasma waves driven by LWFA-generated electron bunches by ruling out any influence of the remaining LWFA drive laser. This proved that the electrons generated in an LWFA stage are able to drive their own plasma waves in independent plasma targets, which is a first major step towards the hybrid scheme.

The third experiment accomplished a second milestone towards the hybrid scheme by reaching two goals. We simultaneously demonstrate that external witness beams can be injected into the electron-driven plasma waves and subsequently accelerated with field strengths on the order of $10\,\mathrm{GV\,m^{-1}}$.

The results from the first and second experiment were published in Physical Review X [30]. The results of the third experiment were partially combined with a second proof-of-principle experiment from the Helmholtz-Zentrum Dresden-Rossendorf (HZDR) into a shared publication in Nature Communications [122], demonstrating the principal feasibility of the hybrid acceleration scheme, and partially with other data from LEX into a second article in Physical Review X [62].

In summary, our studies are major advancements from conventional laser-wakefield accelerators to the full hybrid acceleration scheme. This paves the way towards using advanced injection and acceleration schemes to possibly generate unprecedented electron beam qualities for a plethora of applications.

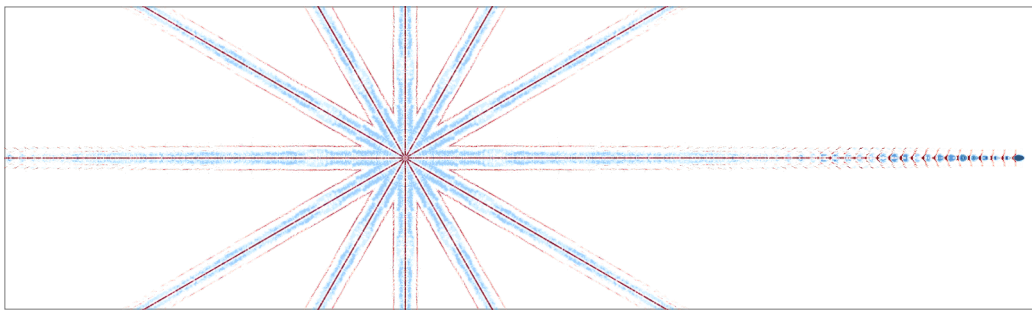

Chapter 4

Ion Dynamics of Particle-Driven Plasma Waves

— I think the probe wandered off again.

In our experiments, the shadowgrams of beam-driven plasma waves often showed a distinctive conical diffraction feature that was not present for laser drivers in the LWFA stage. To our knowledge, such an observation has not been reported for neither LWFA nor PWFA experiments at the time, and its origin was unclear at first. The slowly evolving shape hints towards the dynamics of plasma ions being crucial for its formation. This hypothesis is supported by analytical models and simulations, which show that the ion background interacts with the plasma wave and forms an annular channel with a density peak on axis, in the following referred to as an *ion channel*.

The dynamics of the plasma ions can have detrimental effects on the wakefield generation, e. g, for accelerators that use long driver beams in the self-modulation regime, or operate at high repetition rates. One example is the AWAKE project at CERN, which uses a long proton bunch that has a length of several tens of the plasma wavelength. In this case, the plasma wave is generated by the self-modulation instability, which leads to a growth in wave amplitude and a simultaneous micro-bunching of the driver from its front towards its tail. The ion motion leads to an early saturation of this process, as the ion channel distorts the plasma wave [49, 123]. To our knowledge, our experiments show the first experimental observation of the ion dynamics, and we thereby demonstrate that the hybrid acceleration scheme can be a valuable tool for fundamental PWFA research.

The first part of this chapter discusses the experimental observations of the conical diffraction feature and the reasoning why this must be attributed to the motion of plasma ions. These observations lead to the hypothesis that a strong ion channel formation is an indicator for beam-driven wakefields in hybrid experiments.

The second part outlines the analytical model for the ion channel formation by Vieira *et al.* [65], which is used to derive a direct connection between the shape of the driver and the force on the ion background in a simplified resonant case. This gives a simple and illustrative explanation of why the ion density forms this particular annular shape.

The third part discusses implications of the ion channel formation, e. g., on large-scale PFWA experiments, and ways to mitigate it. The fourth part analyzes the difference in ion channel formation for laser- and electron-driven plasma waves in hybrid experiments, which strengthens the hypothesis that the ion channel is an indicator for electron drivers.

4.1 First Observations of the Ion Channel Formation

In order to find the underlying mechanism that leads to the formation of the conical diffraction feature, we carried out a *fourth* experiment, where the setup was optimized to yield stable and high-contrast shadowgrams of the feature. A suitable configuration was found with a rather small nozzle separation and without a foil to block the laser (see Figure 4.1 for a sketch and the shadowgrams).

Here, the LWFA stage consists of the P5 nozzle with 5 mm orifice diameter, which is equipped with a shock-front injector. The PWFA stage is the Laval 1000 nozzle with a 1 mm orifice diameter. It is operated at an electron density of $6 \times 10^{18}\,\mathrm{cm}^{-3}$ and located with a vacuum gap of 3.5 mm downstream of the the LWFA stage. In this setup, the laser is not blocked by a foil, so its influence cannot generally be excluded. However, conservatively assuming that the laser size at the end of the first stage is equal to the vacuum focus of the F/25 focusing optics, the vacuum propagation of 3.5 mm results in a width of 170 µm and a corresponding decrease in a_0 of almost one order of magnitude. Taking depletion into account further decreases a_0. From this estimation, the laser is not expected to drive a strong wakefield.

Figure 4.2 shows the driver beam profile and spectrum of two reference shots of the LWFA stage. The total measured charge is slightly above 1 nC with a divergence of 0.6 mrad FWHM. The spectral charge density has a peak at 150 MeV, which encloses approximately 500 pC (in the interval from 100 MeV to 200 MeV). The shock-front injector was optimized for a high charge and low divergence in order to have a high charge density and thus drive strength in the PWFA stage. Assuming a bunch length of 1.5 µm FWHM (as found by previous measurements from Buck *et al.*[57]), the peak current is ∼100 kA. This results in a density of $n_b = 1.4 n_0$ at the beginning of the second stage for the measured plasma density $n_0 = 6 \times 10^{24}\,\mathrm{cm}^{-3}$. Such a highly dense driver can be expected to drive a strong plasma wave. The shadowgrams in Figure 4.1b-f of five consecutive shots indeed all show plasma waves as well as the conical diffraction features.

A close-up of the transverse modulation of the diffraction feature in Figure 4.3 reveals three dark and surrounding bright regions, which can yield insight into possible underlying plasma properties. Recalling the basic principles of shadowgraphy (c. f. Section 2.2.4),

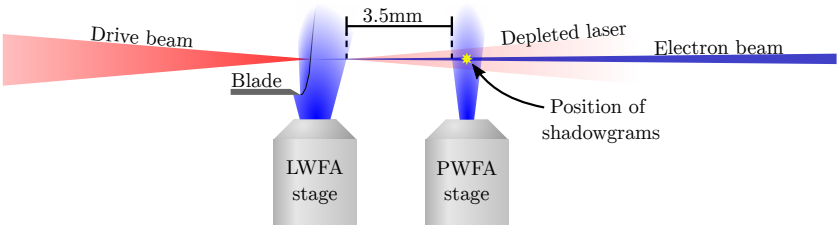

(a) Setup. The shadowgrams are taken in the center of the second stage (yellow star).

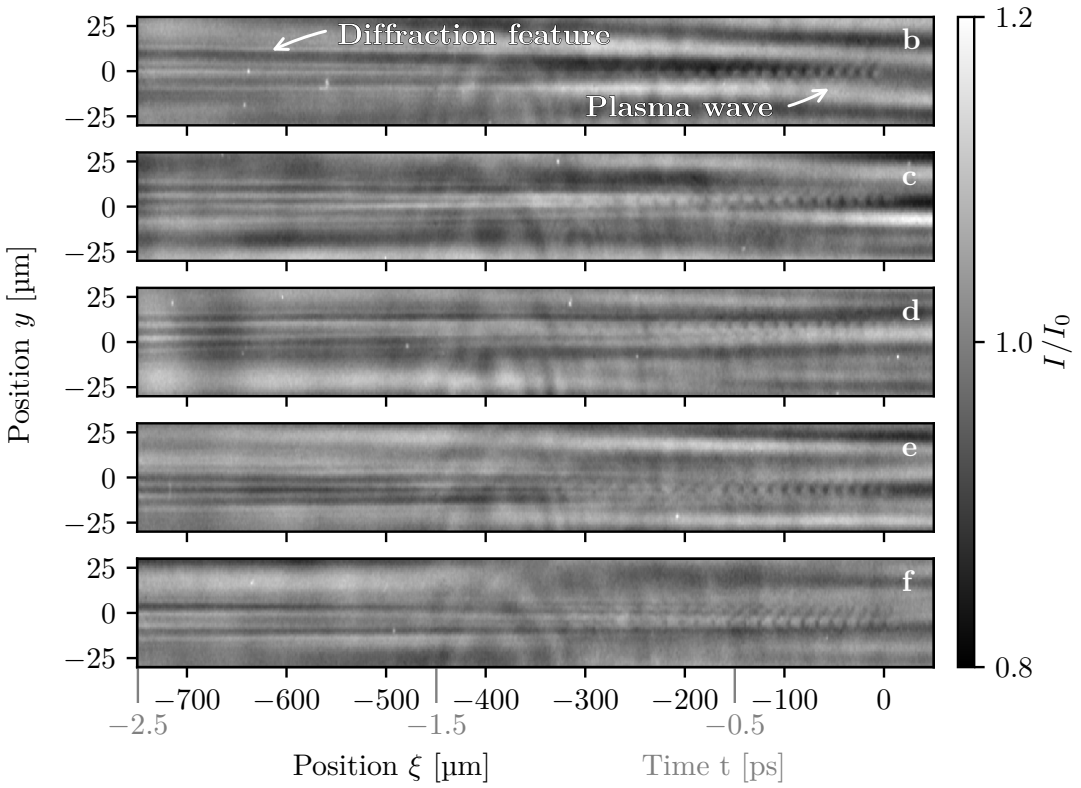

(b-f) Shadowgrams of five consecutive shots. The direction of propagation is to the right.

Figure 4.1: Setup of the *fourth* experiment consisting of the P5 nozzle with 5 mm orifice diameter and a shock-front injector as the LWFA stage, followed by the PWFA stage with the Laval 1000 nozzle with 1 mm orifice diameter. Both jets are separated with a vacuum gap of 3.5 mm. The shadowgrams (b-f) show plasma waves and diffraction features in the PWFA stage.

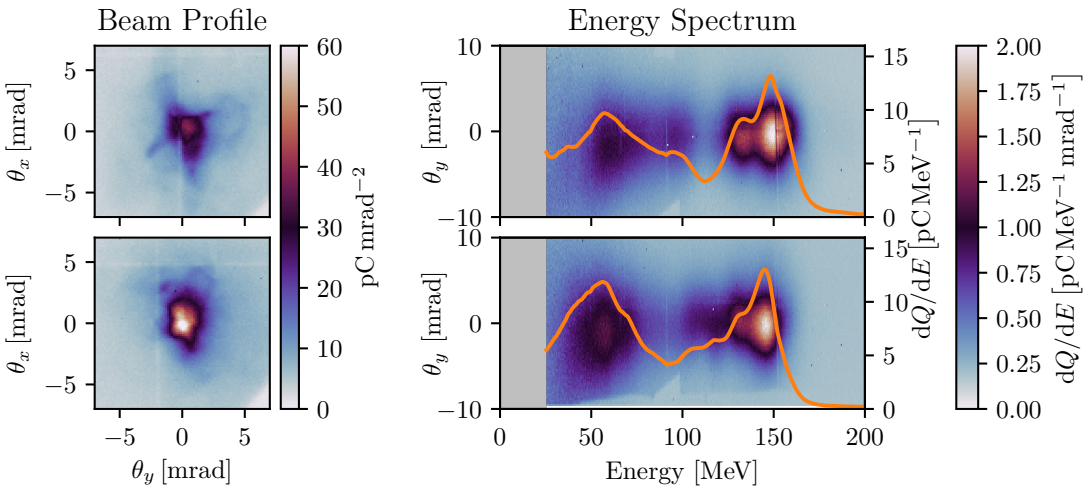

Figure 4.2: Reference driver profiles and spectra for shots in Figure 4.1 (with second stage disabled). (left) Beam profile from the pointing monitor. (right) Energy spectra. The gray shaded area in the spectrum is below the minimum energy of 25 MeV the spectrometer can measure. In both shots, the total charge is slightly above 1 nC, from which ∼500 pC are enclosed in the interval 100 MeV to 200 MeV of the high-energy-peak.

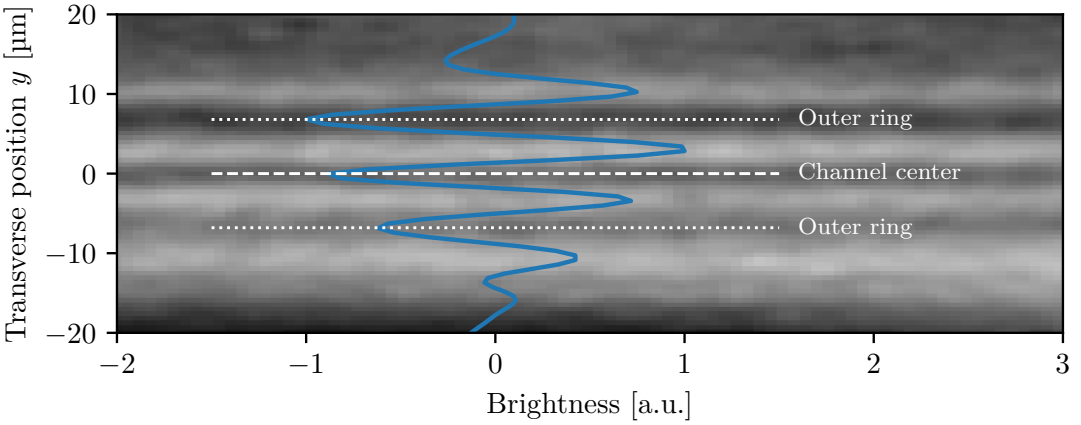

Figure 4.3: Transverse modulation of the ion channel in Figure 4.1b in the interval $-655\,\mu\text{m} < \xi < -600\,\mu\text{m}$. The blue curve shows the average brightness (pixel counts) in ξ (filtered and normalized). The shape appears to be symmetric with respect to the propagation axis with a minimum in the center (dashed line) and another one on each side (dotted line).

the probe laser is diffracted by density gradients of the electron species, so obviously the feature must originate from a modulation in the electron density. Furthermore, it can be assumed that this modulation is almost radially symmetric because of the geometry of the driver and background plasma. We will further assume that the plasma perturbation can be considered as a thin slice for the Probe beam in a very simplified picture, as in Section 2.2.4. Recalling also that in an image plane close to the perturbation regions of increased electron density result in dark regions with bright wings, a possible explanation might be that the diffraction feature is caused by a combination of three high electron density regions (in projection). Such a projection could be caused by an annular high-density ring with an additional peak on the symmetry axis. However, there may be many more possible modulations that led to such a diffraction feature. As a phase retrieval from the shadowgram is not simple and prone to artifacts from noise, we generate synthetic shadowgrams from numerical simulation (see Section 2.2.4) and compare these to the measurements.

A PIC simulation in OSIRIS 4.4 [119], consisting of just plasma and driver electron species, was initialized with the experimental parameters. The simulation window has a size of $(r \times z) = (45 \times 440) \cdot k_\mathrm{p}^{-2}$ at a resolution of $\Delta r = \Delta z = 0.033 k_\mathrm{p}^{-1}$, and four macro particles per cell. A synthetic shadowgram is generated from the simulation by virtually propagating a probe beam through the electron distribution in post-processing (see Section 2.2.4 for more information). Figure 4.4 shows the simulated electron density along with its synthetic shadowgram. The simulation clearly reproduces the plasma wave, however, there is no indication of the conical diffraction feature. This is due to the plasma ion response being neglected here, which is commonly done in PIC simulations to reduce the computational cost. This is often a valid approximation when only short distances to the driver, where the actual particle acceleration takes place, are considered. Here, the plasma is observed over a time-scale of many plasma periods, where the ion motion cannot be neglected any more.

As soon as the ions are treated as mobile in the simulation, the situation is different. Figure 4.5 shows the same simulation as in Figure 4.4 but with mobile ions. Now also the conical diffraction feature is clearly reproduced. The simulation reveals that the shape of the channel is formed by the ion background during the time where the electrons oscillate in the plasma wave. After the plasma wave breaks down, the electrons neutralize the ions and the distribution of the electron species becomes similar to the ion distribution. Thus, the channel becomes visible to the probe. Figure 4.5e shows the trajectories of selected ion macro-particles along with their radial momenta p_r. Ions close to the symmetry axis with $r \lesssim k_p^{-1}$ acquire a negative momentum and are thus accelerated towards the center, ions at higher radii $k_\mathrm{p}^{-1} \lesssim r \lesssim 4k_\mathrm{p}^{-1}$ acquire a positive momentum and are accelerated towards infinity, whereas ions far outside with $r \gtrsim 4k_\mathrm{p}^{-1}$ are almost not influenced. This focuses the ion trajectories for ions close to the symmetry axis towards the axis and ions further outside to a ring at $r \approx 4k_\mathrm{p}^{-1}$, which eventually leads to the observed ion channel.

The ions gain most of their momentum after the driver has passed, specifically while they are located within the plasma wave. This becomes clearly visible in Figure 4.5e for the ion macro-particle starting at $r = 2k_\mathrm{p}^{-1}$, which gains momentum throughout the whole interval $0\,\mu\mathrm{m} < \xi \lesssim 200\,\mu\mathrm{m}$ in which the plasma wave exists. This clearly rules

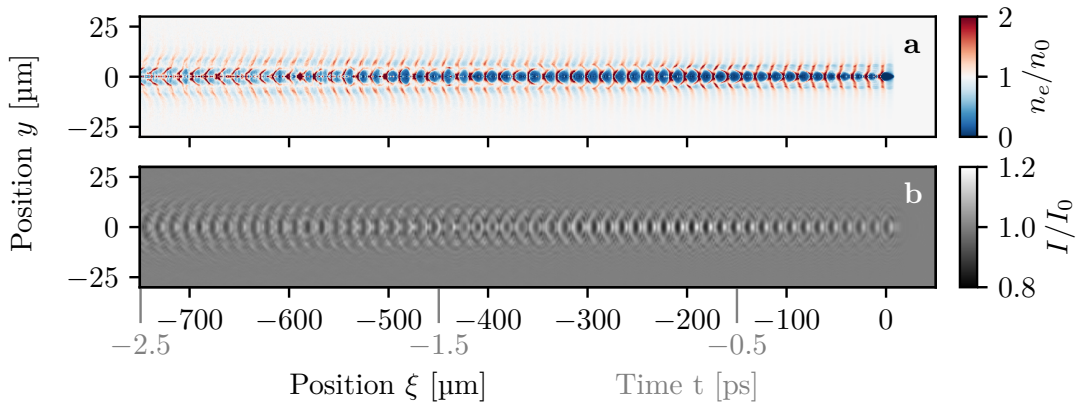

Figure 4.4: Radially symmetric PIC simulation with inferred driver and plasma parameters of the *fourth* experiment (Figure 4.1) with a static ion background. The modulation in the vertical center is the plasma wave.

out a direct Coulomb-interaction between the driver and the background ions being the cause of the channel formation. It should be noted, that this mechanism differs from common ion channel formation due to Coulomb explosion[124, 125]. While a Coulomb explosion leads to a radial expulsion of ions due to thermal motion, and hence a hollow channel, the ion density in our simulations shows an additional density peak on the symmetry axis.

4.2 Theoretical Model

In the previous part, simulations showed that the ion channel is formed by an acceleration of background plasma ions in the vicinity of the plasma wave. Still, from the simulation and the experimental results alone it becomes not immediately clear how the ions are accelerated and on what parameters this depends. In this part, analytical models are used in order to get further insights into this process.

The ion channel formation was theoretically predicted by Gorbunov *et al.* [63, 126, 127] for laser-driven plasma waves and by Vieira *et al.* [64, 65] for self-modulated proton-driven plasma waves. Both models describe essentially the same process that we are observing in the experiments. There is also a direct effect of a charged particle driver on the background ions, as described by Rosenzweig *et al.* [128]. In their model, the electron driver is dense enough to directly accelerate the ions within the first plasma cavity. As the simulation in Figure 4.5 suggests, the acceleration in our case happens after the driver has passed, so this process does not contribute significantly to the channel formation reported here.

A very clear and straightforward derivation of an analytical model for long particle driven wakefields can be found in the publication of Vieira *et al.* [65], who showed that

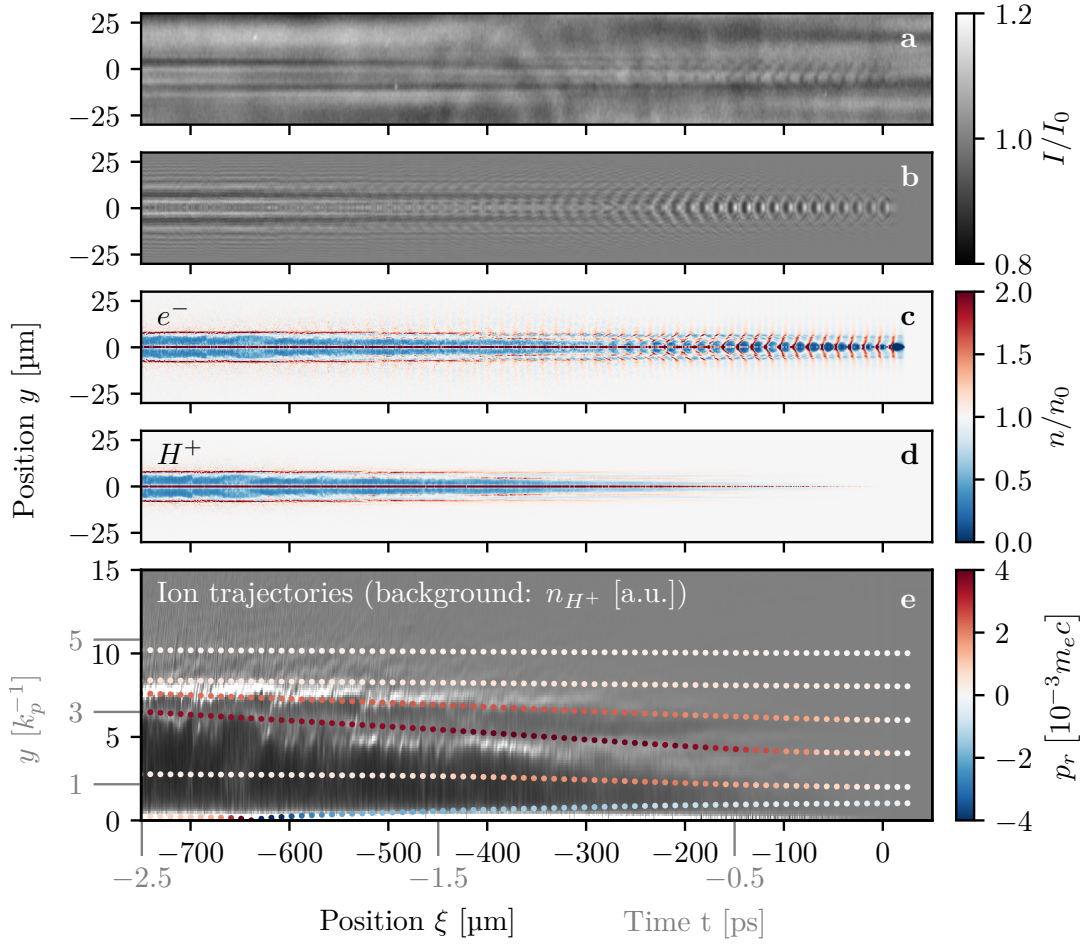

Figure 4.5: Observation and simulation of ion channel formation in beam-driven wakefields. (a) Shadowgram showing a beam-driven plasma wave (propagating to the right) with the ion channel from Figure 4.1 for reference. (b-e) Simulation with the driver and plasma properties of (a), where (b) is a simulated shadowgram of the electron distribution in (c). (d) shows the ion distribution and (e) a close-up with tracks and momenta of selected ion macro-particles. One important observation from (e) is that the ions gain almost all of their momenta within the plasma wave, and not directly from the driver.

the ion background is accelerated by a generalized ponderomotive force of the oscillating electrostatic fields of the plasma wave. This model is valid in a narrow bunch limit where the width of the driver is much smaller than its length such that the electrostatic fields are mainly transverse. It is further assumed that the displacement of the ions is sufficiently small, such that the electron motion is not influenced. While both of these assumptions do not necessarily hold in our case, the model still reproduces the experimental observations qualitatively.

Calculating the ponderomotive force of the plasma wave that acts on the ion background is generally not trivial and usually requires a numerical treatment. However, under certain assumptions one can analytically derive a simple expression that only depends on the fields of the driver. We will briefly describe the derivation of Vieira *et al.*[65] and then apply further approximations to get an analytical expression for the ponderomotive force in the case of a resonant driver. As we will see, the ponderomotive force will lead to an annular ion channel with a density peak on axis, which is in good agreement with our simulations and observations.

Starting with the equations of motion from Dawson's sheet model[72] in a narrow-bunch-limit (no longitudinal fields) and radial symmetry, the plasma electrons oscillate slightly anharmonically around their equilibrium position. The oscillation is forced by the driver's electrostatic fields in its vicinity, and changes to a free oscillation after the driver has passed. The interaction is thus divided into two regions: the vicinity of the driver ($0 < \xi \leq \sigma_z$ in a co-moving frame with $\xi = ct$, denoted by the suffix "1"), and the region behind the driver when the plasma oscillates freely ($\xi > \sigma_z$, denoted by the suffix "2").

First, a solution for the electron motion is derived for the forced oscillation by the driver, which is then used as the initial value to solve the free oscillation after the driver has passed. Once this is found, the motion of the plasma electrons is known and can be used to calculate the transverse fields of the plasma wave and the corresponding ponderomotive force that accelerates the ion background.

The equation of motion including driver fields for small displacements $\Delta r_1(\xi) = r_1(\xi) - r_0$ of an electron ring with initial radius $r_0 = r_1(\xi = 0)$ is [65]

$$c^2 \frac{\mathrm{d}^2 \Delta r_1}{\mathrm{d}\xi^2} = -\frac{eE_r^\mathrm{d}}{m_\mathrm{e}} - \left[\omega_\mathrm{p}^2 + \frac{\mathrm{d}}{\mathrm{d}r}\left(\frac{eE_r^\mathrm{d}(r_0)}{m_\mathrm{e}}\right)\right]\Delta r - \frac{1}{2}\left[\frac{\omega_\mathrm{p}^2}{r_0} + \frac{\mathrm{d}^2}{\mathrm{d}r^2}\left(\frac{eE_r^\mathrm{d}(r_0)}{m_\mathrm{e}}\right)\right]\Delta r^2 \quad (4.1)$$

where E_r^d is the radial electric field of the driver. Note, the formula in [65] is missing a factor of c^2, which is corrected here. The first term is the direct Coulomb-repulsion of the electron ring by the driver via the Lorentz force, the second and third term is the plasma response that leads to the oscillatory motion. For a driver with transverse fields $E_r^\mathrm{d}(r)$ in the interval $0 < \xi \leq \sigma_z$ that are homogeneous in the longitudinal direction, the equation of motion can be solved directly. The electron rings are forced to oscillate according to [65]

$$\Delta r_1 = A_1(r_0)\left[1 - \cos(\phi_1)\right] \quad (4.2)$$

where terms with $\mathcal{O}(\Delta r)^2$ have been neglected. Here, the amplitude of the oscillation is

given by [65]

$$A_1(r_0) = -\frac{E_r^{\mathrm{d}}(r_0)}{\frac{m_\mathrm{e}\omega_\mathrm{p}^2}{e} + \nabla_r E_r^{\mathrm{d}}(r_0)} = -\frac{eE_r^{\mathrm{d}}(r_0)}{m_\mathrm{e}\omega_\mathrm{p}^2}\left(1 - \frac{e}{m_\mathrm{e}\omega_\mathrm{p}^2}\nabla_r E_r^{\mathrm{d}}(r_0)\right) + \mathcal{O}\left(\nabla_r E_r^{\mathrm{d}}(r_0)^2\right), \tag{4.3}$$

where the terms with $\nabla_r E_r^{\mathrm{d}}(r_0)^2$ are anharmonic corrections due to spatially varying driver fields. The phase ϕ_1 of the oscillation is given by [65]

$$\phi_1(r_0) = \frac{\omega_\mathrm{p}\xi}{c}\left[1 + \frac{e}{\omega_\mathrm{p}^2 m_\mathrm{e}}\nabla_r E_r^{\mathrm{d}}(r_0)\right]^{\frac{1}{2}} \tag{4.4}$$

where again the $\nabla_r E_r^{\mathrm{d}}(r_0)^2$ term is an anharmonic correction.

After the driver has passed ($\xi > \sigma_z$), the E_r^{d}-terms vanish in the equation of motion 4.1. The solution becomes [65]

$$\Delta r_2 = A_2(r_0)\cos(\phi_2) - \frac{A_2^2(r_0)}{12 r_0}\left[\cos\left(2\phi_2(r_0)\right) - 3\right] + \mathcal{O}\left(A_2^3\right) \tag{4.5}$$

with amplitude $A_2(r_0)$ and phase $\phi_2(r_0)$. These parameters now depend on the initial conditions, i. e., the electron ring displacement Δr_1 and its derivative at the transition $\xi = \sigma_z$. The amplitude is found to be [65]

$$A_2(r_0) = \left[\Delta r_2(\sigma_z)^2 + \frac{c^2}{\omega_\mathrm{p}^2}\left(\frac{d\Delta r_2(\sigma_z)}{d\xi}\right)^2\right]^{\frac{1}{2}} \tag{4.6}$$

where $\Delta r_2(\sigma_z) = \Delta r_1(\sigma_z)$ is the displacement at the transition, and $d\Delta r_2(\sigma_z)/d\xi = d\Delta r_1(\sigma_z)/d\xi$ the derivative evaluated at $\xi = \sigma_z$. The phase is [65]

$$\phi_2 = \omega_p \xi\left[1 + \frac{1}{12}\frac{A_2(r_0)^2}{r_0^2}\right], \tag{4.7}$$

which has an anharmonic correction term that depends on the oscillation amplitude. With this, the radius of each electron ring and thus the whole distribution of the plasma electrons is known in principle, or at least, can be calculated.

In order to calculate the force exerted on the ion background by the plasma wave, the electrostatic fields $E_{1,2}$ of the plasma electrons need to be found. This can be achieved by inverting the electron trajectories. The total energy gain of an ion located at r_0 is then depending on the averaged Lorentz force $F_{1,2} = e\left\langle E_{1,2}(r_0)\right\rangle$. In the interval after which the driver has passed ($\xi > \sigma_z$), averaging the field over a plasma period yields

$$\langle E_2\rangle = \frac{1}{2\pi}\int_0^{2\pi} E_2 d\phi = -\frac{1}{4}\nabla_r \frac{e\hat{E}_2^2}{m_\mathrm{e}\omega_\mathrm{p}^2} + \mathcal{O}\left(\nabla_r \hat{E}_2\right)^3 \tag{4.8}$$

where $\hat{E}_2 = m_\mathrm{e}\omega_\mathrm{p}^2 A_2/e$ is the field amplitude. The main result of this derivation is that the Lorentz force corresponding to the average field $F = q_\mathrm{i}\langle E_2\rangle \propto \nabla_r \hat{E}_2^2 + \mathcal{O}(\nabla_r \hat{E}_2^2)$

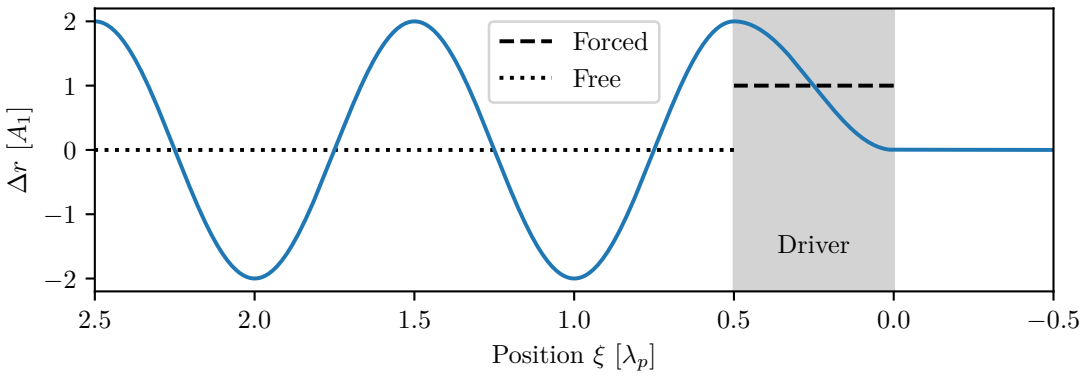

Figure 4.6: Motion of an electron ring in a simplified linear case and with a resonant driver. The dashed and dotted lines denote the equilibrium position during the interaction with the driver and thereafter. Initially, before the driver arrives (at $\xi < 0$), the electron ring is at rest in its equilibrium position $\Delta_r = r - r_0 = 0$. While the driver passes the electron ring ($0 \leq \xi < \lambda_p/2$), its fields lead to a temporary change of the equilibrium position to $r_0 + A_1$, around which the initially resting electron ring starts to oscillate. The length $\sigma_z = \lambda_p/2$ of the driver is chosen such that the electron ring completes one half oscillation and is at rest at $\Delta_r = 2A_1$. At this time, the driver has passed the electron ring and the external fields vanish, such that the old equilibrium position at $\Delta_r = 0$ is restored. As the electron ring is at rest at the moment the old equilibrium is restored, the new oscillation amplitude will be given by the corresponding displacement $A_2 = 2A_1$.

with the ion charge q_i has the structure of a ponderomotive force. This means, ions are accelerated from regions of high average field amplitude to low average field amplitude. From this, one can already guess that the acceleration of some ions towards the symmetry axis in Figure 4.5 is the result of the vanishing field amplitudes in the center because of the radial symmetry. Under certain approximations this result can easily be analytically obtained from the equations of motion.

We will use a simplified case of a step-like driver to demonstrate the motion of the background plasma electrons and the long-term behavior of the ions. As we will see, the basic picture is that the plasma counteracts the electrostatic fields of the driver by moving electrons away and thus creating a charge imbalance. This charge imbalance is still present after the driver has passed and is sustained over long timescales, during which it accelerates the background ions.

Under the assumption of a step-like, resonant driver with transverse fields $E_r^\mathrm{d}(r_0)$, length $\sigma_z = \lambda_p/2$ and large width (where the fields do not vary significantly over the displacement of background plasma electrons $e/m_e\omega_p^2\nabla_r E_r^d \ll 1$), however, one can find a simple solution of the ponderomotive force depending only on the driver fields. Under these conditions, i. e., neglecting all orders of $\nabla_r E_r^d$, the equation of motion of the forced

oscillation simply reduces to

$$\Delta r_1 = eE_r^d/m_e\omega_p^2[1 - cos(\omega_p\xi/c)]. \tag{4.9}$$

Thus, in the presence of the driver, the equilibrium radius of an electron ring is temporarily increased by A_1, as shown in Figure 4.6. This change happens instantly, such that the electrons begin to oscillate around $r_0 + A_1$ starting from the radius $r(0) = r_0$ at rest. After $\xi = \sigma_z$, the displacement of such a ring is

$$\Delta r_2(\sigma_z) = -2\frac{e}{m_e\omega_p^2}E_r^d(r_0), \tag{4.10}$$

At this point, the ring completed half an oscillation and is at rest again, so the derivative becomes zero.

$$\frac{d\Delta r_2(\sigma_z)}{d\xi} = 0 \tag{4.11}$$

The ring has moved by twice the amplitude A_1 to $r(\xi) = r_0 + 2A_1$. After the driver has passed, the drive term in the equation of motion instantly vanishes and the ring begins oscillating around its initial equilibrium position r_0, to which it now has a displacement of $2A_1$ and is at rest, such that the new amplitude becomes

$$A_2(r_0) = 2A_1(r_0). \tag{4.12}$$

by substituting Equations 4.10 and 4.11 for Δr_1 and its derivative in Equation 4.6. The amplitude of the free oscillation $A_2(r_0)$ and $\hat{E}_2 = m_e\omega_p^2 A_2/e$ can be inserted into Equation 4.8 to finally get the ponderomotive force

$$F_p(r) = q_i \langle E_2(r)\rangle = -q_i\nabla_r \left[E_r^d(r)\right]^2 \tag{4.13}$$

which is, in this simplified case, directly proportional to the gradient of the squared driver fields. Equation 4.13 holds only under the previously mentioned assumptions, however, the argument that the driver imprints an averaged field onto the plasma is qualitatively still true for more realistic cases.

Consider for example a cylindrical driver with a homogeneous charge distribution with radius $\sigma_r \ll \sigma_z$ and assume only transverse fields. The field $E_r^d(r < \sigma_r)$ inside of the driver increases linearly with radius and decreases with $1/r$ for $r > \sigma_r$ outside the driver, which is illustrated in Figure 4.7. The derivative of E_r^d is then positive for $r \leq \sigma_r$ and negative for $r > \sigma_r$, thus the ponderomotive force $F \propto -\nabla(E_r^d)^2$ of the plasma wave pushes ions away from the cylinder surface where the field reaches its maximum. This leads to ions inside of the driver being accelerated towards the center, and ions on the outside towards higher radii, which eventually results in an annular channel with a density peak on axis.

4.3 Implications on the Design of PWFAs

The ion channel formation leads to a perturbation of the plasma over rather long timescales. This can be problematic, e. g., for accelerators that operate with long driver

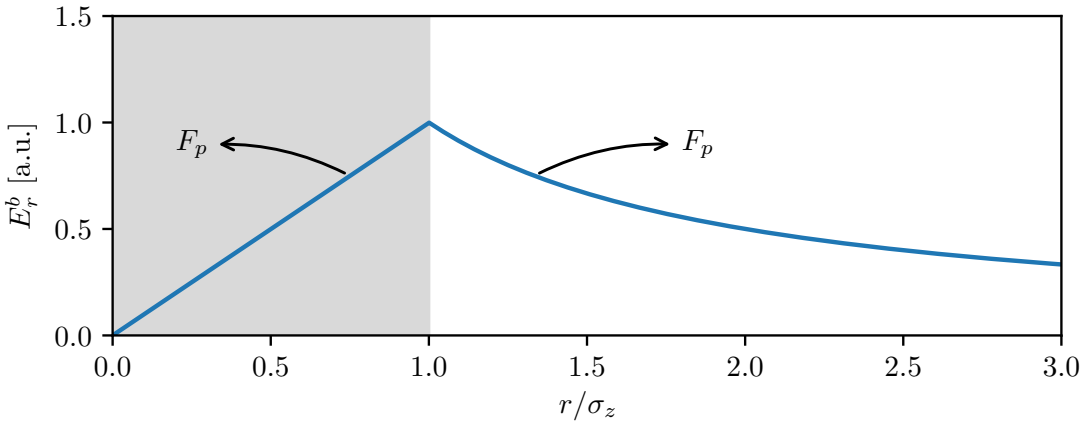

Figure 4.7: Electric field of a dense cylindrical electron beam with radius σ_z, neglecting boundary fields. The area with driver electrons is shaded in gray. In a simplified model, the ponderomotive force of the plasma wave (direction denoted by the arrows) $F_p \propto \nabla_r (E_r^{\mathrm{d}})^2$ pushes ions away from regions where the driver-fields were high.

bunches in the self-modulated regime, or future accelerators that may operate at high repetition frequencies (or bursts) if the plasma has not yet recovered when the subsequent driver arrives.

Using the hybrid scheme enables a relatively easy way to estimate these timescales, as shadowgrams can easily be taken long after the driver has passed. For this purpose, a *fifth* experiment was carried out in the context of a collaboration at the Laboratoire d'Optique Appliquée (LOA) in France, with a setup similar to the previous experiment. A sketch of this setup is shown in Figure 4.9a. The LWFA and PWFA stage each consists of a supersonic de Laval nozzle with 3 mm outlet diameter (these are not mentioned in the section 2.2.1), whose center-to-center distance was set to 3.5 mm. In order to get the stages so close, they were rotated by 45° with respect to each other along the azimuthal angle of the laser axis. In order to block the laser between the stages, a circular BoPET foil (Mylar) was pressed between two circularly etched steel supports with 120 holes for the foil along the perimeter (see Figure 4.9a). This structure was motorized and can be rotated to the next position on the foil for each subsequent shot. The first stage was operated with a gas mixture of 99 % H_2 and 1 % N_2 in order to inject electrons by ionization injection [21, 22], the second stage with pure H_2. Figure 4.8 shows spectra of two reference shots from the LWFA stage and foil in the beam path. The absolute measured charge is 46 pC and 35 pC at a high-energy cutoff of 160 MeV and 140 MeV, respectively. The gas in the second jet can optionally be pre-ionized with an additional, counter-propagating laser.

Figure 4.9b shows shadowgrams of the PWFA stage at different times, with and without pre-ionization. Here, only the timing of the probe was changed. The self-ionized case shows an expanding diffraction feature up to at least 167 ps (which corresponds to

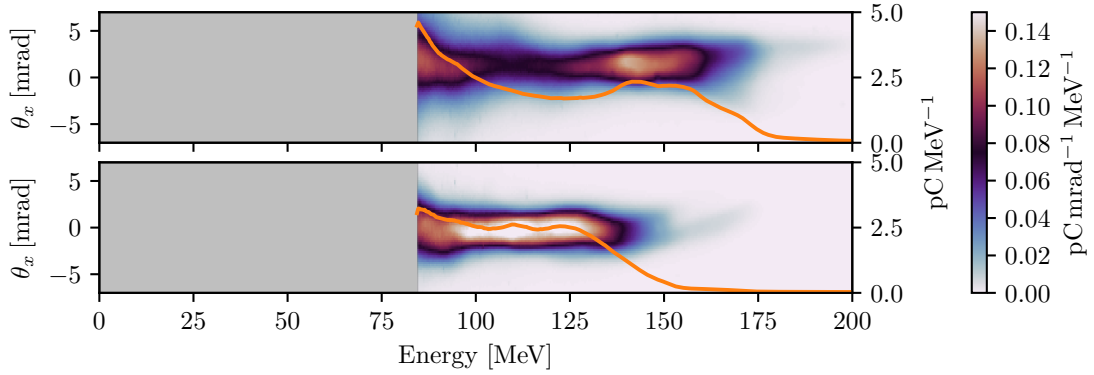

Figure 4.8: Experiment *five*: Two consecutive driver beam spectra for shots in Figure 4.9 with second stage disabled and foil enabled. The gray shaded area in the spectrum is below the measurable bandwidth of the spectrometer. The total charge of the two shots is 46 pC and 35 pC, respectively, whereas the energy contained in the high-energy peak of the first shot (120 MeV to 200 MeV) is 23 pC.

a propagation distance of 10 mm) after the driver has passed. Here, the electron beam ionizes the gas by itself, and the diffraction feature can be either an expanding ionization channel, an ion channel formed by the ponderomotive force of the plasma wave, or a mixture of both. The diffraction feature is still visible in the case of the pre-ionized plasma, although with a substantial amount of noise. In this case, it can be ruled out that the observed feature is an ionization channel, as the gas is already fully ionized by the pre-ionizing laser beam, so the features can be attributed to the ion channel formation. In both cases the plasma wave is not visible because the probe beam is not sufficiently temporally compressed. The Mylar foil was mounted on a rotating wheel that only allowed 120 shots before the vacuum chamber needed to be vented in order to replace the foil. Unfortunately, this led to the foil running out of free spots such that there is no data for the pre-ionized case at 167 ps.Because of the scaling with the plasma density, the time over which this perturbation would be measurable in a large-scale low-density accelerator at a density of $1 \times 10^{14}\,\mathrm{cm}^{-3}$ is in the range of nanoseconds. This experiment shows that the perturbations due to the ion motion is sustained over long timescales and can thereby be problematic for accelerators the rely either on a long interaction like for the self-modulation process, or on high repetition rates.

One particular case where the ion channel formation has already led to a constraint on an actual experiment is the AWAKE project at CERN [25, 50]. In this experiment, the driver is a long proton beam with a length in the order of $100 \times \lambda_\mathrm{p}$, which drives the PWFA stage in a self-modulated regime. Simulations suggested that the ion channel formation in a Hydrogen plasma would lead to an early saturation of the self-modulation growth [64]. As suggested by Rosenzweig *et al.*[128], the plasma perturbation of the ion channel can, however, be mitigated by using a heavier ion species. The ponderomotive

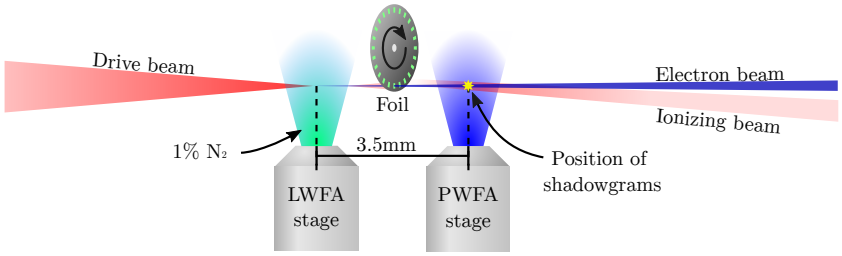

(a) Setup of the *fifth* experiment (at LOA) consisting of a gas jet with shock-front injector followed by a H_2 gas jet with 3.5 mm center distance. The shadowgrams are taken close to the center of the second stage (yellow star). The laser is blocked with a Mylar foil in between the jets, and a second laser beam is optionally used to preionize the second stage.

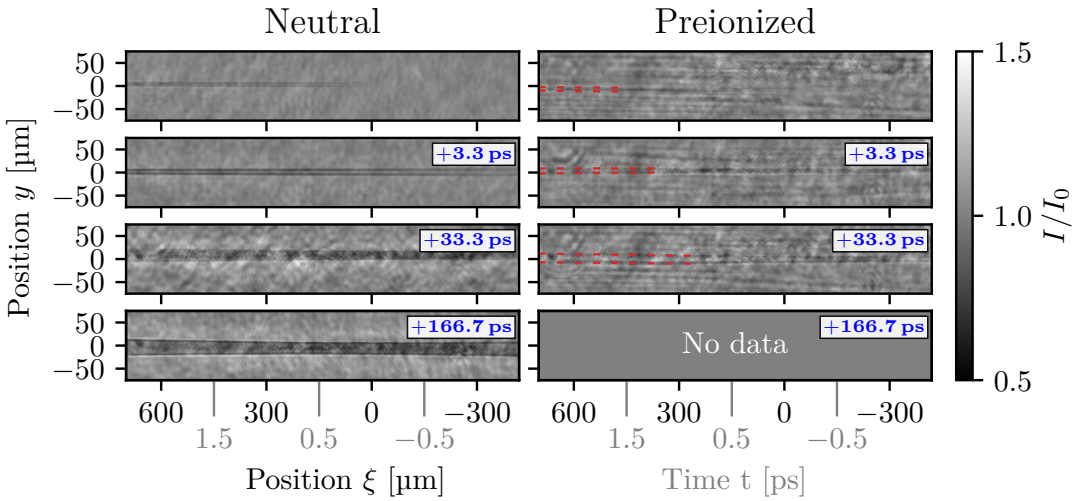

(b) Shadowgrams of the second stage at different times. The left side shows the self-ionized case (i. e., the ionizing laser beam is deactivated), whereas the right side shows the preionized case.

Figure 4.9: The shadowgrams in the self-ionized case show a strong diffraction signal even at 167 ps ≙ 50 mm after the driver has passed. Here, the diffraction signal is not necessarily caused by the ion motion, but can simply be caused by an expanding column of plasma. The pre-ionized case, however, also shows a relatively weak signal, which cannot be attributed to ionization but rather the ion channel formation.

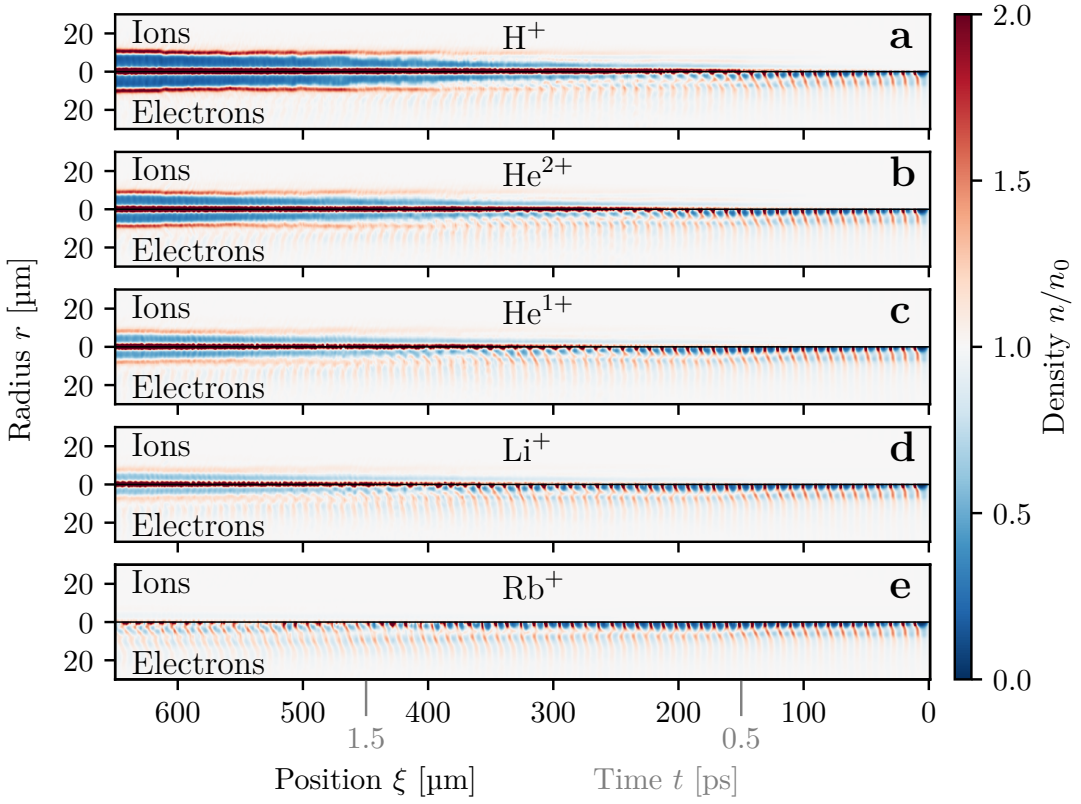

Figure 4.10: Simulations of the ion channel formation with different ion species. The top half of each density plot shows the ion density, the bottom half shows the electron density. As the ponderomotive ion acceleration scales with the ratio of charge to mass, its effect becomes gradually smaller when going from lighter ions in (a) to heavy ions in (e). As the ion channel formation is suppressed for heavy ions, the plasma wave is sustained over longer times.

force in Equation 4.13 shows that the acceleration depends on the ratio of the ion's charge to mass, so the ponderomotive acceleration becomes smaller and the ion channel formation is suppressed for increasing ion mass. Figure 4.10 shows the same simulation as in the first part of this chapter (see Figure 4.5) but with different ion species. As the ratio of mass to charge is increased, the ion channel becomes less and less pronounced. This is the reason that AWAKE uses a particularly heavy gas, specifically Rb, for which the ion channel in Figure 4.10e is almost not visible any more. The simulations also show that for such heavy ion species the plasma wave is sustained over much longer times than in the case of light ions like H^+, which clearly demonstrates that the ion motion plays a crucial role in the ability to sustain plasma waves over long times, and that it can be responsible for the early breaking of plasma waves in accordance with e. g., [63, 64].

The ion channel formation is an important energy dissipation channel in plasma

wakefields, as energy is directly transferred from the plasma wave to the ion background before thermalisation. Figure 4.11 shows the (H^+) ion and electron energy densities in a particle-in-cell simulation with a non-evolving electron driver. As before, the simulation is radially symmetric with a window of $(r \times z) = (45 \times 440) \cdot k_\mathrm{p}^{-2}$ at a resolution of $\Delta r = \Delta z = 0.033 k_\mathrm{p}^{-1}$ and four particles per cell and species. The driver has infinite longitudinal momentum (free-streaming), a peak density of $n = 2.5 n_0$ and a size of $\sigma_\xi = \sigma_r = 0.5 k_\mathrm{p}^{-1}$. Initially, energy is transferred from the driver to plasma electrons, leading to the formation of the plasma wave, which accelerates the ion background by its ponderomotive force. The ion species gains energy throughout the plasma wave, until it saturates when the wave dies off. At this point, the total amount of energy of the accelerated ions is approximately 5 % of the (now mostly thermal) energy of the electrons.

4.4 Difference to Laser-Driven Wakefields

As the ion channel is formed by the plasma wave's ponderomotive force, which is solely due to the presence of oscillating fields with transversally varying amplitude, one might conclude that also laser-driven plasma waves should excite such a channel, and in principle this is correct. However, as described in the last chapter, we did not observe ion channels in the LWFA stage, at least not as pronounced as in the PWFA stage. Assuming that the ponderomotive force of a laser-driven plasma wave has a similar shape as the ponderomotive force of a beam-driven wave, this can have at least two obvious possible reasons. The first one is that the overall force might lower, e. g., because of a larger radius which results in a smaller gradient. The second one is that the time over which the acceleration happens might be shorter, e. g., because the wave breaks earlier. The length of the plasma wave that we measured in the LWFA stage is not generally shorter than the plasma waves in the PWFA stage, so in many cases this reason can be ruled out. The radius of the plasma wave, however, does indeed differ and has a strong influence on the channel formation.

Gorbunov *et al.*[63] studied the ion channel formation of linear, laser-driven plasma waves analytically and numerically. They found that the shape of the ion channel depends strongly on the width of the driver. Figure 4.12 shows the transverse shape $f(k_\mathrm{p} r)$ of the ion distribution for various laser widths at an arbitrary point behind the driver. In dimensionless coordinates ($\rho = k_\mathrm{p} r$ and $\eta = k_\mathrm{p} \xi$), it is defined as

$$f(\rho) = -\frac{16}{\rho_0^2} \exp^{-4\frac{\rho^2}{\rho_0^2}} \left[\left(1 - \frac{4}{\rho_0^2}\right) - 4\frac{\rho^2}{\rho_0^2}\left(1 - \frac{12}{\rho_0^2}\right) - 64\frac{\rho^4}{\rho_0^6} \right] \tag{4.14}$$

with the dimensionless laser width ρ_0. The actual density perturbation is directly proportional to f and can be calculated with

$$\frac{\delta n_\mathrm{i}}{n_0} = \frac{\pi \delta a_0^4 \eta_0^2}{256} \eta^2 \exp^{-\frac{\eta_0^2}{4}} f(\rho) \tag{4.15}$$

where $\delta = Z m_\mathrm{e}/m_\mathrm{i}$ is the charge-to-mass ratio of the ion species normalized to an electron, and η_0 is the dimensionless length of the laser. Noteworthy, the shape of the ion

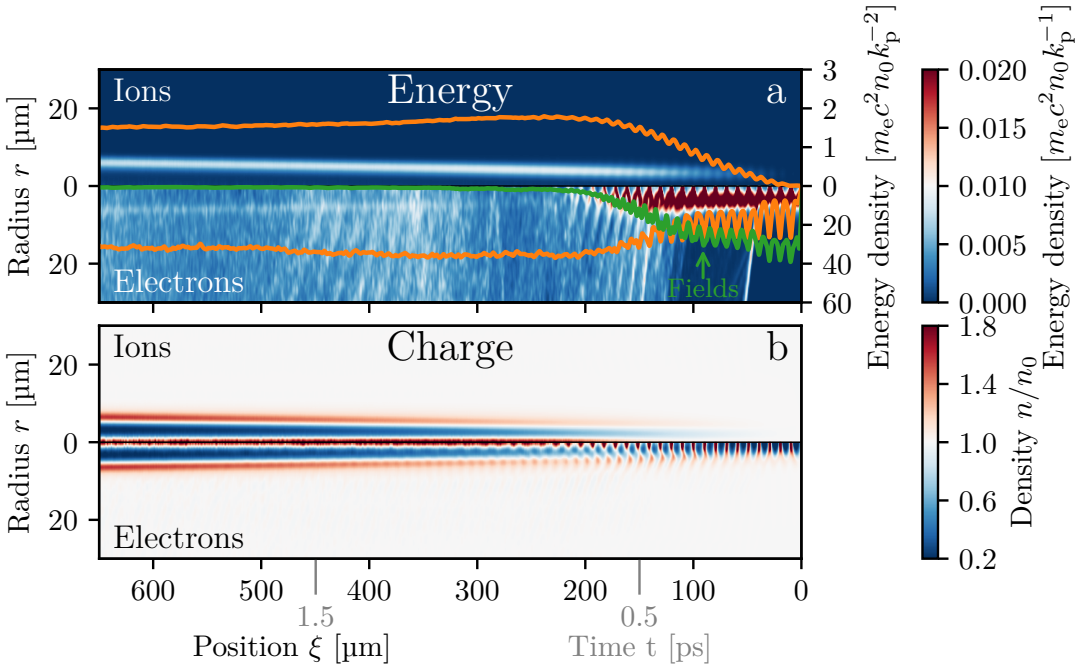

Figure 4.11: Energy dissipation of a simulated beam-driven plasma wave with a non-evolving driver. The top plot (a) shows the kinetic energy density integrated over the azimuthal coordinate ϕ of the ion (top half) and electron (bottom half) species. The lineouts show the energy density integrated over the whole transverse plane (r and ϕ), so the energy per length in longitudinal direction for the particle species (orange) and the electromagnetic fields (green). For a better visibility, the scale of the ion energy lineout is increased by a factor of 20 with respect to the electron energy lineout (note the different scales on the right). (b) shows the charge distribution of both species. The modulation of the electron kinetic energy in the interval $0 < \xi < 200$ is the oscillation of the plasma wave, where energy is transferred between kinetic and potential energy, i. e., electrostatic fields. In this interval also the ion species gains kinetic energy by being transversally accelerated in the plasma wave. The ion species gains kinetic energy throughout the plasma wave. After it has broken down, the energy contained in the ion species is approximately 5 % of the energy contained in the electron species.

channel does only depend on the laser width ρ_0 and not on a_0. Figure 4.12 shows, that for increasing laser widths the ion modulation becomes shallower, and below a FWHM of $\lambda_p/2$, the distribution has a density peak on axis and on an outer radius. In contrast, the channel of a plasma wave driven by a wider laser is just a shallow ion depression region with a significantly reduced depth. Figure 4.13 exemplarily shows simulations of ion channels created by laser pulses with various intensities and sizes after 1 mm of propagation in plasma. For increasing a_0 the channel becomes slightly larger and the modulation depth slightly decreases, but the ion channel is clearly visible in all cases. Due to the lower gradient of the electrostatic fields in the case of a driver with twice the diameter, the depth of the ion channel is strongly reduced by a factor of approximately 10. In this parameter range, at least, it appears that the difference in width has a much stronger influence on the ion channel formation compared to the difference in the vector potential.

The strong dependence of the ion channel depth on the laser width may explain why only one of the waves in the shadowgram with two waves from the previous chapter (Figure 3.3) is accompanied by an ion channel. Assuming that the FWHM width of the laser at the end of the LWFA stage is equal to the vacuum focus $w_0 = 25\,\mu\text{m}$ of the F/25 optics, the width of the laser increases by a factor of 9 during the vacuum propagation towards the PWFA stage. As a_0 is directly proportional to the width, it will decrease by a factor of 9 solely due to its divergence. Assuming further that the laser did not loose any of the 2.5 J energy in the LWFA stage, the vector potential at the beginning of the PWFA stage is then $a_0 \approx 0.24$. Considering the simulation in Figure 4.13e (where the laser also has an energy of $\sim 2.5\,\text{J}$), even with an increase in width by only a factor of 2 there is no ion channel visible at all. Self-focusing might eventually reduce the size after some propagation, however, the simulation suggests that even after the simulated interaction length of 3 mm the laser did not self-focus sufficiently to generate a noticeable ion channel.

In comparison with the laser, the electron bunch remains relatively small. The measured divergence was usually well below 2 mrad, which results in a FWHM bunch size of approximately 15 µm at the beginning of the PWFA stage (assuming an initial FWHM waist of 5 µm at the end of the first stage), which is approximately equal to the plasma wavelength and a factor of 15 smaller than the laser. The simulations of the previous chapter show that the electron beam self-focuses much stronger than the laser, so the difference in size will increase even more.

Figure 4.13 demonstrates, that at least in our setup, the formation of the ion channel is strongly suppressed because the laser diffracts in the vacuum gap between the stages, however, even a low-amplitude plasma wave is visible in the shadowgram. So, if a plasma wave is observed without an ion channel, it is likely driven by the laser. On the other hand, if an ion channel is visible, the plasma wave is likely driven by the electrons, as their size is typically much smaller than the laser. Further studies are necessary to understand why the laser-driven plasma wave does not show such clear ion channels even when it is tightly focused in the LWFA jet.

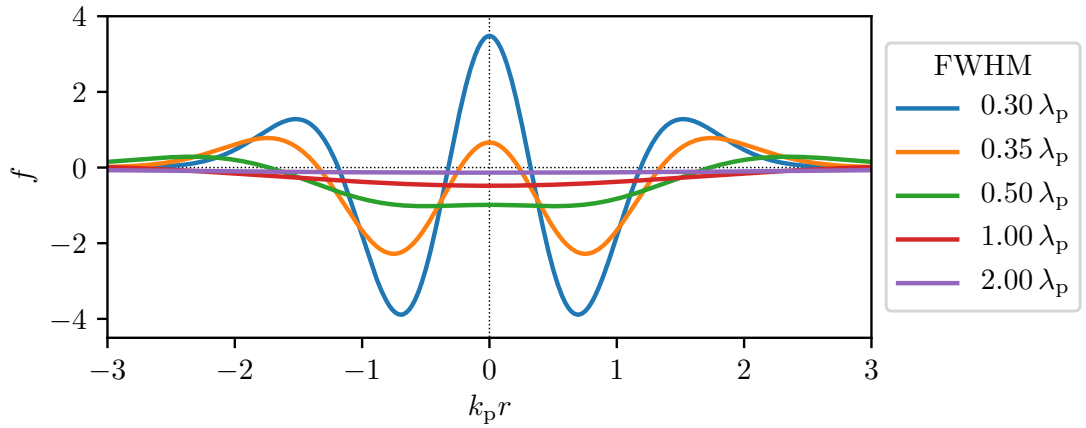

Figure 4.12: Transverse shape of the ion distribution for different laser waists according to Gorbunov *et al.*[63]. For laser (FWHM) waists below approximately half the plasma wavelength, a density peak appears on axis. For larger laser waists, the peak disappears, and the ion channel becomes shallower. In our experiments, the vacuum laser waist is typically at approximately twice the plasma wavelength (purple line).

4.5 Summary

In this chapter, we showed that the conical diffraction feature that was regularly observed in the shadowgrams of beam-driven plasma waves can be attributed to the dynamics of the background plasma ions. Simulations clearly reproduce this feature as shown in Figure 4.5. They show that ions within the plasma wave become accelerated to either the symmetry axis or away from the plasma wave, depending on their initial position, which results in an annular ring with a peak on axis.

Theoretical models of Vieira *et al.*[64, 65] and Gorbunov *et al.*[63, 126] show that the ion channel is formed by a ponderomotive acceleration of the ion background from the oscillating fields of the plasma wave. From this, a direct connection between the fields of the driver and the force acted on the ions was found in a simplified resonant case. Exemplarily, if a dense cylindrical driver is used, the annular shape of the ion channel with a central peak becomes directly apparent (see Figure 4.7).

The ion channel formation perturbs the plasma after several plasma periods over long timescales. In our experiment, the plasma perturbation is sustained over at least 33 ps at a density of $\sim 1 \times 10^{18}\,\mathrm{cm}^{-3}$, which translates to a perturbation on a nanosecond-scale for plasma wakefield accelerators at densities of $1 \times 10^{14}\,\mathrm{cm}^{-3}$ (see Figure 4.9b) which is used in e. g. the AWAKE project. However, we demonstrate that the ion channel formation can be suppressed by choosing a heavy ion species. In AWAKE, this already led to an actual constraint, where the ion channel formation of light gases like H_2 would lead to a suppression of the self-modulation process, such that it is necessary to use a

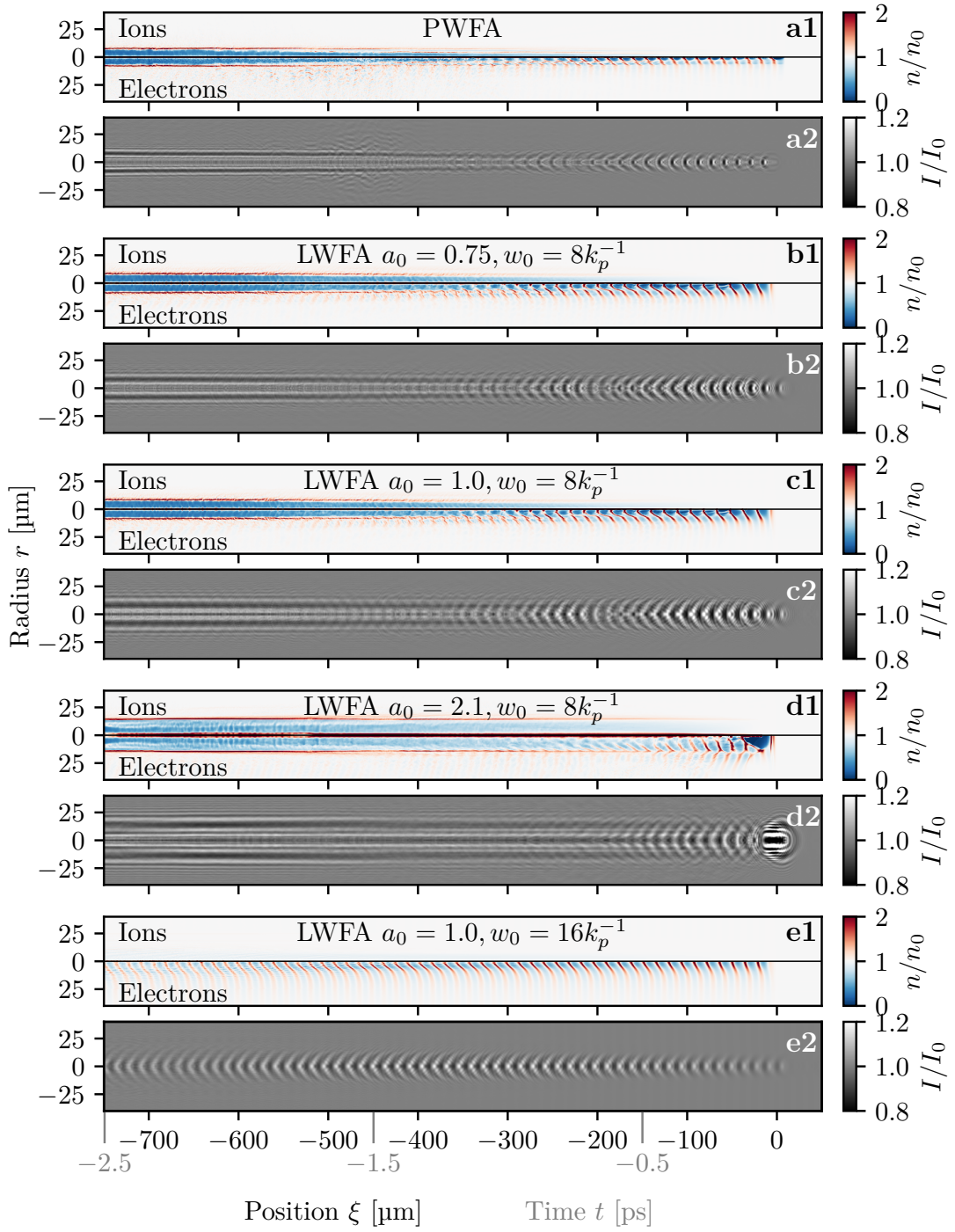

Figure 4.13: Particle-in-cell simulations and synthetic shadowgrams of the ion dynamics of laser- and particle-driven plasma waves. (a) shows the beam-driven plasma wave from Figure 4.1 for reference. (b-d) shows simulations of lasers with different amplitudes, and (e) for a laser with twice the diameter.

heavier gas.

A question that arose in the first chapter was whether the existence of an ion channel is an indicator for the plasma wave being driven by an electron bunch. The fact, that solely the ponderomotive force of the plasma wave is responsible for the acceleration of the ions means that also laser-driven waves should create ion channels. However, as the laser is usually larger than the electron bunch, especially in the second stage after the laser has substantially diffracted, the excitation of the ion channel is expected to be highly suppressed as predicted by Gorbunov *et al.*[63]. Simulations suggest that the laser in the experiments presented here will not show any sign of an ion channel in the second stage as they are simply too large in diameter (c. f. Figure 4.13). However, further studies are necessary to verify this.

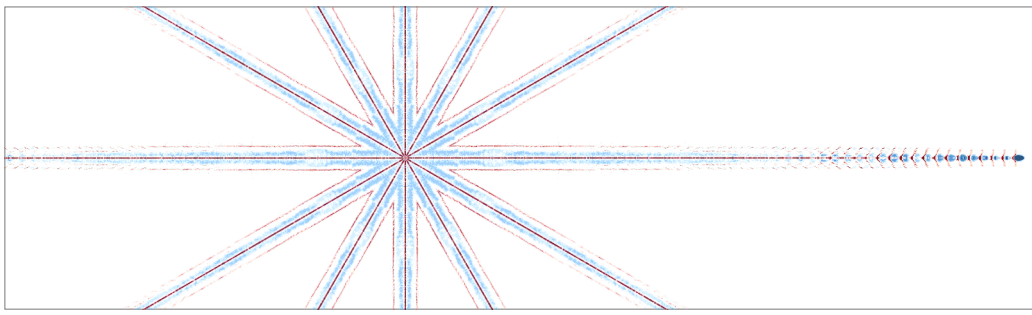

Chapter 5

Conclusion and Outlook

— And now, ten shots without powder.

Conventional radio-frequency (RF) accelerators deliver particle beams for various applications like high-energy particle colliders and light sources. They significantly contributed to a plethora of discoveries and advances in many fields of science, like high-energy physics, medicine, chemistry and material science. However, they suffer from limited acceleration gradients, which makes them large and expensive. A promising novel accelerator concept that overcomes this limitation is plasma acceleration.

There exist two major kinds of plasma accelerators that drive the acceleration process either with laser pulses (LWFA) or with charged particle bunches (PWFA). While PWFA requires highly energetic particle beams and therefore large RF pre-accelerators, it has the prospect of generating ultra-high quality particle beams and is arguably the most promising candidate for building a new generation of large-scale accelerators and FELs. On the other hand, LWFA systems are much more compact, as they do not require RF pre-accelerators. They nowadays deliver nC-scale electron beams with currents exceeding the kA-level [30, 31]. However, the suffer from limited energy gains in a single stage, and in terms of energy spread and stability they are far from reaching the performance of RF accelerators.

The hybrid acceleration scheme [1] combines the benefits of LWFA and PWFA, such that the prospects of PWFA can be realized in compact and cost-effective laser facilities. This is achieved by using the high current and low divergence electron beam produced in an LWFA stage to drive the PWFA process. The experiments presented in this thesis are together with the studies of our colleagues at the HZDR the first experimental breakthrough.

In a first part, we demonstrated the feasibility of the hybrid scheme. This was achieved by firstly proving that the LWFA-generated electron bunches are able to drive their own plasma waves in a separate plasma target. For that, we generated nanocoulomb-scale electron bunches with divergences below 1 mrad and observed their driven plasma waves with few-cycle shadowgraphy [57]. In a second step, these plasma waves were used to

accelerate witness electron bunches with gradients on the order of $10\,\mathrm{GeV\,m^{-1}}$. These witness beams were externally generated and injected into the PWFA stage with capture efficiencies exceeding 50 %, which is (to our knowledge) higher than all previously reported capture efficiencies into plasma accelerators.

In a second part, we showed that the hybrid scheme is a valuable tool to study fundamental PWFA mechanisms. First observations of the PWFA process showed a channel pattern in shadowgrams, which can be attributed to plasma ions being accelerated by a generalized ponderomotive force of the plasma wave. This was theoretically proposed several years ago [63, 64] and has strong implications on the design of large-scale PWFA experiments like in the AWAKE project. To our knowledge, our measurement is the first reported observation of the ion dynamics.

With our research, we paved the way towards using the hybrid scheme to its full potential. This led to a collaboration with groups from the Helmholtz-Zentrum Dresden-Rossendorf (HZDR), the Laboratoire d'Optique Appliquée (LOA) at the Institut Polytechnique de Paris, the Deutsches Elektronen-Synchrotron (DESY), and the University of Strathclyde, to combine expertise and bring the hybrid scheme forward with dedicated research. Recent measurements of J. P. Couperus Cabadağ *et al.* (preliminary, unpublished) show controlled internal injection in the PWFA stage and acceleration gradients exceeding $100\,\mathrm{GeV\,m^{-1}}$. Further measurements of M. Foerster *et al.* (preliminary, unpublished) suggest that the PWFA-generated beam stabilities are comparable to conventional, state-of-the-art PWFA experiments. Future studies will also focus on novel injection methods like Trojan Horse, WII, and optically-induced density down-ramps. In 2020, the hybrid scheme was listed as a potential and innovative development path in the EuPRAXIA Conceptual Design Report, and it will be studied whether it can have a future implementation to improve EuPRAXIA machine properties [129].

It can be expected, that the steady advances in laser peak powers will increase the LWFA performance and thus open new doors to study the hybrid scheme. The ATLAS was recently moved to the Centre for Advanced Laser Applications (CALA) and was upgraded by a tenfold in peak power to 3 PW, which makes it one of the strongest Ti:Sa laser systems worldwide and an ideal system for the development of hybrid accelerators. However, even with widely available 100 TW-level laser systems there is still a lot of potential. Firstly, development of LWFA plasma targets and LWFA injection mechanisms may allow further optimization of the beam parameters for the PWFA process in terms of current, divergence, energy and stability. Secondly, our experiments were limited by mechanical constraints that can easily be overcome. Mainly, the separation of the LWFA and PWFA stage can be significantly reduced by dedicated hybrid target structures, such that the detrimental effects from the beam transport and the foil that blocks the laser can be mitigated. This may allow to utilize the hybrid scheme with novel injection mechanisms like Trojan Horse or WII in the near future.

There are long- and mid-term prospects of building dedicated hybrid-based FELs, but it could have a much more short-term application. The proof-of-concept LWFA-based FEL realization by Wang *et al.* [55] and several other experiments pursuing FEL lasing would benefit significantly from improved beam qualities, and upgrading the LWFA stage to a hybrid LWFA-PWFA stage may be a promising and relatively easy option.

Generally, now that laser systems are strong enough to drive a hybrid accelerator, the first and arguably biggest step has been made. The realization of compact PWFA machines and beam qualities exceeding the ones from individual LWFA and PWFA systems comes within close reach and will open new opportunities in the development of e. g. novel light sources and the next generation of particle colliders.

Bibliography

1. Hidding, B. *et al.* Monoenergetic Energy Doubling in a Hybrid Laser-Plasma Wakefield Accelerator. *Physical Review Letters* **104,** 195002 (May 2010).
2. Kilpatrick, W. D. Criterion for vacuum sparking designed to include both rf and dc. *Review of Scientific Instruments* **28,** 824–826 (1957).
3. Broemmelsiek, D. *et al.* Record high-gradient SRF beam acceleration at Fermilab. *New Journal of Physics* **20,** 113018 (2018).
4. Benedikt, M. *et al. Future Circular Collider - The Lepton Collider (FCC-ee)* tech. rep. Future Circular Collider - European Strategy Update Documents (CERN, Geneva, 2019).
5. Benedikt, M. *et al. Future Circular Collider - The Hadron Collider (FCC-hh)* tech. rep. 1. Benedikt, M., Blondel, A., Brunner, O., Capeans Garrido, M., Cerutti, F., Gutleber, J., Janot, P., Jimenez, J. M., Mertens, V., Milanese, A., Oide, K., Osborne, J. A., Otto, T., Papaphilippou, Y., Poole, J., Tavian, L. J. & Zimmermann, F. Future Circul (CERN, Geneva, 2019).
6. The CEPC Study Group. CEPC Conceptual Design Report: Volume 1 - Accelerator. *arXiv.org* **physics.ac,** arXiv:1809.00285 (Sept. 2018).
7. Behnke, T. *et al. ILC Technical Design Report* tech. rep. (2013).
8. High Energy Accelerator Research Organization (KEK). *Recommendations on ILC Project Implementation* tech. rep. (High Energy Accelerator Research Organization (KEK), 2019).
9. International Linear Collider (ILC) Advisory Panel. *Summary of the ILC Advisory Panel's Discussions to Date after Revision* tech. rep. (2018).
10. Huang, N., Deng, H., Liu, B., Wang, D. & Zhao, Z. Features and futures of X-ray free-electron lasers. *Innovation(United States)* **2,** 100097 (2021).
11. Decking, W. *et al.* A MHz-repetition-rate hard X-ray free-electron laser driven by a superconducting linear accelerator. *Nature Photonics* **14,** 391–397 (2020).
12. Madey, J. M. J. Stimulated Emission of Bremsstrahlung in a Periodic Magnetic Field. *Journal of Applied Physics* **42,** 1906–1913 (Apr. 1971).
13. Tajima, T. & Dawson, J. Laser electron accelerator. *Physical Review Letters* **4,** 267–270 (1979).
14. Chen, P., Dawson, J. M., Huff, R. W. & Katsouleas, T. Acceleration of Electrons by the Interaction of a Bunched Electron Beam with a Plasma. *Physical Review Letters* **54,** 693–696 (1985).
15. Hidding, B., Foster, B., Hogan, M. J., Muggli, P. & Rosenzweig, J. B. Directions in plasma wakefield acceleration. *Philosophical Transactions of the Royal Society A: Mathematical, Physical and Engineering Sciences* **377** (2019).

16. Rosenzweig, J., Barov, N., Murokh, A., Colby, E. & Colestock, P. Towards a plasma wake-field acceleration-based linear collider. *Nuclear Instruments and Methods in Physics Research Section A: Accelerators, Spectrometers, Detectors and Associated Equipment* **410,** 532–543 (June 1998).

17. Pukhov, a. & Meyer-ter-Vehn, J. Laser wake field acceleration: the highly non-linear broken-wave regime. *Applied Physics B: Lasers and Optics* **74,** 355–361 (Apr. 2002).

18. Rosenzweig, J. B., Breizman, B., Katsouleas, T. & Su, J. J. Acceleration and focusing of electrons in two-dimensional nonlinear plasma wake fields. *Physical Review A* **44,** R6189–R6192 (Nov. 1991).

19. Schmid, K. *et al.* Density-transition based electron injector for laser driven wake-field accelerators. *Physical Review Special Topics - Accelerators and Beams* **13,** 091301 (Sept. 2010).

20. Faure, J. *et al.* Controlled injection and acceleration of electrons in plasma wake-fields by colliding laser pulses. *Nature* **444,** 737–739 (2006).

21. McGuffey, C. *et al.* Ionization Induced Trapping in a Laser Wakefield Accelerator. *Physical Review Letters* **104,** 025004 (Jan. 2010).

22. Pak, A. *et al.* Injection and Trapping of Tunnel-Ionized Electrons into Laser-Produced Wakes. *Physical Review Letters* **104,** 025003 (Jan. 2010).

23. Rosenzweig, J. B. *et al.* Experimental Observation of Plasma Wake-Field Acceleration. *Physical Review Letters* **61,** 98–101 (July 1988).

24. Steinke, S. *et al.* Multistage coupling of independent laser-plasma accelerators. *Nature* **530,** 190–193 (2016).

25. Adli, E. *et al.* Acceleration of electrons in the plasma wakefield of a proton bunch. *Nature* **561,** 363–367 (Sept. 2018).

26. Wu, Y. *et al.* High-throughput injection–acceleration of electron bunches from a linear accelerator to a laser wakefield accelerator. *Nature Physics* **17,** 801–806 (2021).

27. Faure, J. *et al.* A laser–plasma accelerator producing monoenergetic electron beams. *Nature* **431,** 541–544 (Sept. 2004).

28. Mangles, S., Murphy, C. & Najmudin, Z. Monoenergetic beams of relativistic electrons from intense laser–plasma interactions. *Nature,* 535–538 (2004).

29. Geddes, C. G. R. *et al.* High-quality electron beams from a laser wakefield accelerator using plasma-channel guiding. *Nature* **431,** 538–541 (Sept. 2004).

30. Gilljohann, M. F. *et al.* Direct Observation of Plasma Waves and Dynamics Induced by Laser-Accelerated Electron Beams. *Physical Review X* **9,** 011046 (Mar. 2019).

31. Couperus, J. P. *et al.* Demonstration of a beam loaded nanocoulomb-class laser wakefield accelerator. *Nature Communications* **8,** 487 (Dec. 2017).

32. Gonsalves, A. J. *et al.* Petawatt Laser Guiding and Electron Beam Acceleration to 8 GeV in a Laser-Heated Capillary Discharge Waveguide. *Physical Review Letters* **122,** 084801 (Feb. 2019).

33. Maier, A. R. *et al.* Decoding Sources of Energy Variability in a Laser-Plasma Accelerator. *Physical Review X* **10,** 31039 (2020).

34. Mangles, S. P. An overview of recent progress in laser wakefield acceleration experiments. *CAS-CERN Accelerator School: Plasma Wake Acceleration 2014, Proceedings* **001,** 289–300 (2014).

35. Strickland, D. & Mourou, G. Compression of amplified chirped optical pulses. *Optics Communications* **55,** 447–449 (Oct. 1985).

36. Sprangle, P. *et al.* Wakefield generation and GeV acceleration in tapered plasma channels. *Physical Review E - Statistical, Nonlinear, and Soft Matter Physics* **63,** 564051–5640511 (2001).

37. Caizergues, C., Smartsev, S., Malka, V. & Thaury, C. Phase-locked laser-wakefield electron acceleration. *Nature Photonics* **14,** 475–479 (Aug. 2020).

38. Kalmykov, S., Yi, S. A., Khudik, V. & Shvets, G. Electron self-injection and trapping into an evolving plasma bubble. *Physical Review Letters* **103,** 1–4 (2009).

39. Kostyukov, I., Nerush, E., Pukhov, A. & Seredov, V. Electron self-Injection in multidimensional relativistic-plasma wake fields. *Physical Review Letters* **103,** 1–4 (2009).

40. Thomas, A. G. Scalings for radiation from plasma bubbles. *Physics of Plasmas* **17** (2010).

41. Yi, S. A., Khudik, V., Kalmykov, S. Y. & Shvets, G. Hamiltonian analysis of electron self-injection and acceleration into an evolving plasma bubble. *Plasma Physics and Controlled Fusion* **53,** 014012 (Jan. 2011).

42. Schroeder, C. B., Esarey, E., Shadwick, B. A. & Leemand, W. P. *Trapping and Dark Current in Plasma-Based Accelerators* in *AIP Conference Proceedings* **737** (AIP, 2004), 564–570.

43. Martinez de la Ossa, A., Grebenyuk, J., Mehrling, T., Schaper, L. & Osterhoff, J. High-Quality Electron Beams from Beam-Driven Plasma Accelerators by Wakefield-Induced Ionization Injection. *Physical Review Letters* **111,** 245003 (Dec. 2013).

44. Hidding, B. *et al.* Beyond injection: Trojan horse underdense photocathode plasma wakefield acceleration. *AIP Conference Proceedings* **1507,** 570–575 (2012).

45. Blumenfeld, I. *et al.* Energy doubling of 42 GeV electrons in a metre-scale plasma wakefield accelerator. *Nature* **445,** 741–744 (Feb. 2007).

46. Martinez de la Ossa, A., Mehrling, T. J., Schaper, L., Streeter, M. J. & Osterhoff, J. Wakefield-induced ionization injection in beam-driven plasma accelerators. *Physics of Plasmas* **22** (2015).

47. Yakimenko, V. *et al.* FACET-II facility for advanced accelerator experimental tests. *Physical Review Accelerators and Beams* **22,** 101301 (Oct. 2019).
48. D'Arcy, R. *et al. FLASHForward - A Future-Oriented Wakefield-Accelerator Research and Development Facility at FLASH* in *Proceedings of IPAC2017* (Copenhagen, Denmark, 2017), 1692–1695.
49. Bracco, C. *et al.* AWAKE: A Proton-Driven Plasma Wakefield Acceleration Experiment at CERN. *Nuclear and Particle Physics Proceedings* **273-275,** 175–180 (Apr. 2016).
50. Gschwendtner, E. *et al.* AWAKE, The Advanced Proton Driven Plasma Wakefield Acceleration Experiment at CERN. *Nuclear Instruments and Methods in Physics Research, Section A: Accelerators, Spectrometers, Detectors and Associated Equipment* **829,** 76–82 (2016).
51. Aschikhin, A. *et al.* The FLASHForward facility at DESY. *Nuclear Instruments and Methods in Physics Research Section A: Accelerators, Spectrometers, Detectors and Associated Equipment* **806,** 175–183 (Jan. 2016).
52. Deng, A. *et al.* Generation and acceleration of electron bunches from a plasma photocathode. *Nature Physics* **15,** 1156–1160 (2019).
53. Ullmann, D. *et al.* All-optical density downramp injection in electron-driven plasma wakefield accelerators. *Physical Review Research* **3,** 1–12 (2021).
54. Knetsch, A. *et al.* Stable witness-beam formation in a beam-driven plasma cathode. *Physical Review Accelerators and Beams* **24,** 101302 (Oct. 2021).
55. Wang, W. *et al.* Free-electron lasing at 27 nanometres based on a laser wakefield accelerator. *Nature* **595,** 516–520 (July 2021).
56. Hidding, B. *et al.* Fundamentals and applications of hybrid LWFA-PWFA. *Applied Sciences (Switzerland)* **9** (2019).
57. Buck, A. *et al.* Real-time observation of laser-driven electron acceleration. *Nature Physics* **7,** 543–548 (July 2011).
58. Yu, L. H. Generation of intense uv radiation by subharmonically seeded single-pass free-electron lasers. *Physical Review A* **44,** 5178–5193 (Oct. 1991).
59. Chou, S. *et al.* Collective Deceleration of Laser-Driven Electron Bunches. *Physical Review Letters* **117,** 144801 (Sept. 2016).
60. Heigoldt, M. *et al.* Temporal evolution of longitudinal bunch profile in a laser wakefield accelerator. *Physical Review Special Topics - Accelerators and Beams* **18,** 1–6 (2015).
61. Kuschel, S. *et al.* Demonstration of passive plasma lensing of a laser wakefield accelerated electron bunch. *Physical Review Accelerators and Beams* **19,** 071301 (2016).
62. Götzfried, J. *et al.* Physics of High-Charge Electron Beams in Laser-Plasma Wakefields. *Physical Review X* **10,** 041015 (Oct. 2020).

63. Gorbunov, L. M., Mora, P. & Solodov, A. A. Plasma Ions Dynamics in the Wake of a Short Laser Pulse. *Physical Review Letters* **86,** 3332–3335 (2001).

64. Vieira, J., Fonseca, R. A., Mori, W. B. & Silva, L. O. Ion Motion in Self-Modulated Plasma Wakefield Accelerators. *Physical Review Letters* **109,** 145005 (Oct. 2012).

65. Vieira, J., Fonseca, R. A., Mori, W. B. & Silva, L. O. Ion motion in the wake driven by long particle bunches in plasmas. *Physics of Plasmas* **21,** 056705 (May 2014).

66. Jackson, J. D. *Classical Electrodynamics* 3rd (Wiley, New York, 1999).

67. Fitzpatrick, R. *Plasma Physics: An Introduction* (CRC Press, Taylor & Francis Group, 2014).

68. Gibbon, P. *Short Pulse Laser Interaction with Matter* 312 (Imperial College Press, London, 2007).

69. Kruer, W. & Dawson, J. *The physics of laser plasma interactions* (Westview Press, 2003).

70. Esarey, E., Schroeder, C. B. & Leemans, W. P. Physics of laser-driven plasma-based electron accelerators. *Reviews of Modern Physics* **81,** 1229–1285 (Aug. 2009).

71. Joachain, C. J. Atoms in intense laser fields C. *AIP Conference Proceedings* **3** (1998).

72. Dawson, J. Nonlinear electron oscillations in a cold plasma. *Physical Review* **113** (1959).

73. Gorbunov, L. & Kirsanov, V. Excitation of plasma waves by an electromagnetic wave packet. *Sov. Phys. JETP* **18,** 290–294 (1987).

74. Fubiani, G., Esarey, E., Schroeder, C. B. & Leemans, W. P. Beat wave injection of electrons into plasma waves using two interfering laser pulses. *Physical Review E* **70,** 016402 (July 2004).

75. Panofsky, W. K. H. & Wenzel, W. A. Some Considerations Concerning the Transverse Deflection of Charged Particles in Radio-Frequency Fields. *Review of Scientific Instruments* **27,** 967–967 (Nov. 1956).

76. Esarey, E., Sprangle, P., Krall, J., Ting, A. & Joyce, G. Optically guided laser wake-field acceleration. *Physics of Fluids B* **5,** 2690–2697 (1993).

77. Teychenné, D., Bonnaud, G. & Bobin, J. Wave-breaking limit to the wake-field effect in an underdense plasma. *Physical Review E* **48,** 3248–3251 (1993).

78. Berezhiani, V. I. & Murusidze, I. G. Interaction of highly relativistic short laser pulses with plasmas and nonlinear wake-field generation. *Physica Scripta* **45,** 87–90 (Feb. 1992).

79. Sprangle, P., Esarey, E. & Krall, J. Self-guiding and stability of intense optical beams in gases undergoing ionization. *Physical review. E, Statistical physics, plasmas, fluids, and related interdisciplinary topics* **54,** 4211–4232 (Oct. 1996).

80. Sun, G.-Z., Ott, E., Lee, Y. C. & Guzdar, P. Self-focusing of short intense pulses in plasmas. *Physics of Fluids* **30,** 526 (1987).

81. Esarey, E., Shadwick, B. A., Schroeder, C. B. & Leemans, W. P. Nonlinear Pump Depletion and Electron Dephasing in Laser Wakefield Accelerators. *AIP Conference Proceedings* **737** (2004).

82. Shadwick, B. a., Schroeder, C. B. & Esarey, E. Nonlinear laser energy depletion in laser-plasma accelerators. *Physics of Plasmas* **16,** 056704 (2009).

83. Muggli, P. Beam-driven, plasma-based particle accelerators. *CAS-CERN Accelerator School: Plasma Wake Acceleration 2014, Proceedings,* 119–142 (2014).

84. Bane, K. L. F., Wilson, P. B. & Weiland, T. *Wake Fields and Wake Field Acceleration* in *Physics of High Energy Particle Accelerators* (eds Month, M., Dahl, P. F. & Dienes, M.) (American Institute of Physics, 1985).

85. Chen, P., Su, J. J., Dawson, J. M., Bane, K. L. F. & Wilson, P. B. Energy Transfer in the Plasma Wake-Field Accelerator. *Physical Review Letters* **56,** 1252–1255 (Mar. 1986).

86. Rosenzweig, J. Nonlinear Plasma Dynanics in the Plasma Wakefield Accelerator. *IEEE Transactions on Plasma Science* **15,** 186–191 (1987).

87. Günther, B. *Design, implementation and characterisation of the 300TW-upgrade of the ATLAS laser system* Masterthesis (Technische Universität München, 2014).

88. Trebino, R. *et al.* Measuring ultrashort laser pulses in the time-frequency domain using frequency-resolved optical gating. *Review of Scientific Instruments* **68,** 3277–3295 (1997).

89. Oksenhendler, T. *et al.* Self-referenced spectral interferometry. *Applied Physics B: Lasers and Optics* **99,** 7–12 (2010).

90. Pretzler, G., Kasper, A. & Witte, K. Angular chirp and tilted light pulses in CPA lasers. *Applied Physics B: Lasers and Optics* **70,** 1–9 (Jan. 2000).

91. Hebling, J. Derivation of the pulse front tilt caused by angular dispersion. *Optical and Quantum Electronics* **28,** 1759–1763 (Dec. 1996).

92. Popp, A. *et al.* All-Optical Steering of Laser-Wakefield-Accelerated Electron Beams. *Physical Review Letters* **105,** 215001 (Nov. 2010).

93. Popp, A. *Dynamics of electron acceleration in laser-driven wakefields: Acceleration limits and asymmetric plasma waves* Dissertation (Ludwig-Maximilians Universität München, 2011).

94. Schmid, K. *Supersonic Micro-Jets And Their Application to Few-Cycle Laser-Driven Electron Acceleration* Dissertation (Ludwig–Maximilians–Universität München, 2009).

95. Hüther, M. *Design and Characterisation of Supersonic Nozzles for Shock Front Electron Injection in Laser Wakefield Acceleration* Masterthesis (Ludwig-Maximilians-Universität München, 2015).

96. Buck, A. *et al.* Shock-Front Injector for High-Quality Laser-Plasma Acceleration. *Physical Review Letters* **110,** 185006 (May 2013).

97. De Laval, C. G. P. *Steam Turbine* 1888.

98. Sutton, G. P. & Biblarz, O. *Rocket Propulsion Elements* (John Wiley & Sons., 2001).

99. Wildgruber, L. *Few-cycle probing of high-power laser induced plasma* Masterthesis (Ludwig-Maximilians-Universität München, 2017).

100. Ding, H. *et al.* Nonlinear plasma wavelength scalings in a laser wakefield accelerator. *Physical Review E* **101,** 023209 (Feb. 2020).

101. Sampath, A. *et al.* Extremely Dense Gamma-Ray Pulses in Electron Beam-Multifoil Collisions. *Physical Review Letters* **126,** 064801 (Feb. 2021).

102. Lynch, G. R. & Dahl, O. I. Approximations to multiple Coulomb scattering. *Nuclear Inst. and Methods in Physics Research, B* **58,** 6–10 (1991).

103. Zyla, P. A. *et al.* Review of Particle Physics. *Progress of Theoretical and Experimental Physics* **2020,** 1–2093 (Aug. 2020).

104. Corde, S. *et al. Beam focusing by near-field transition radiation* tech. rep. hal-02937777v2 HAL (IP Paris, CEA, MPIK, 2020).

105. Wille, K. *Physik der Teilchenbeschleuniger und Synchrotronstrahlungsquellen* 2nd, 365 (B. G. Teubner, Stuttgart, 1996).

106. Raj, G. *et al.* Probing ultrafast magnetic-field generation by current filamentation instability in femtosecond relativistic laser-matter interactions. *Physical Review Research* **2,** 1–7 (2020).

107. Hidding, B. *et al.* First Measurements of Trojan Horse Injection in a Plasma Wakefield Accelerator. *Proceedings of IPAC2017* (2017).

108. Kurz, T. *Calibration of scintillation screens for bunch charge determination in laser wakefield acceleration* Masterthesis (Ludwig-Maximilians-Universität München, 2016).

109. Kurz, T. *et al.* Calibration and cross-laboratory implementation of scintillating screens for electron bunch charge determination. *Review of Scientific Instruments* **89,** 093303 (Sept. 2018).

110. Panigrahi, P. K. & Muralidhar, K. *Schlieren and Shadowgraph Methods in Heat and Mass Transfer* 139 (2012).

111. Sävert, A. *et al.* Direct Observation of the Injection Dynamics of a Laser Wakefield Accelerator Using Few-Femtosecond Shadowgraphy. *Physical Review Letters* **115,** 055002 (July 2015).

112. Ding, H. *Doktorarbeit (in progress, unpublished)* Dissertation (Ludwig-Maximilians-Universität München, 2021).

113. Daiber, F. M. *Generation of Few Cycle Pulses for Direct Observation of the Plasma Wave Master thesis* Masterthesis (Ludwig-Maximilians-Universität, München, 2015).

114. Siminos, E. *et al.* Modeling ultrafast shadowgraphy in laser-plasma interaction experiments. *Plasma Physics and Controlled Fusion* **58,** 065004 (2016).

115. Wenz, J. *et al.* Dual-energy electron beams from a compact laser-driven accelerator. *Nature Photonics* **13,** 263–269 (Apr. 2019).

116. Schindler, S. *et al. Tunable X-ray source by Thomson scattering during laser-wakefield acceleration* in *Laser Acceleration of Electrons, Protons, and Ions V* (eds Esarey, E., Schroeder, C. B. & Schreiber, J.) (SPIE, Apr. 2019), 22.

117. Ferri, J. *et al.* Effect of experimental laser imperfections on laser wakefield acceleration and betatron source. *Scientific Reports* **6,** 1–10 (2016).

118. Chou, S.-W. *Investigation of electron acceleration and deceleration in plasmas* Dissertation (Ludwig-Maximilians-Universität München, 2016).

119. Fonseca, R., Silva, L. & Tsung, F. OSIRIS: A three-dimensional, fully relativistic particle in cell code for modeling plasma based accelerators. *Computational Science — ICCS 2002: Lecture Notes in Computer Science* **2331,** 342–351 (2002).

120. Heigoldt, M. *Temporal dynamics of the longitudinal bunch profile in a laser wakefield accelerator* PhD thesis (Ludwig-Maximilians-Universität München, 2017).

121. Bruhwiler, D. L. *et al.* Particle-in-cell simulations of tunneling ionization effects in plasma-based accelerators. *Physics of Plasmas* **10,** 2022–2030 (May 2003).

122. Kurz, T. *et al.* Demonstration of a compact plasma accelerator powered by laser-accelerated electron beams. *Nature Communications* **12,** 2895 (Dec. 2021).

123. Vieira, J., Mori, W. B. & Muggli, P. Hosing instability suppression in self-modulated plasma wakefields. *Physical Review Letters* **112,** 1–5 (2014).

124. Mangles, S. P. *et al.* Electron acceleration in cavitated channels formed by a petawatt laser in low-density plasma. *Physical Review Letters* **94,** 1–4 (2005).

125. Tarkeshian, R. *et al.* Transverse Space-Charge Field-Induced Plasma Dynamics for Ultraintense Electron-Beam Characterization. *Physical Review X* **8,** 21039 (2018).

126. Gorbunov, L. M., Mora, P. & Solodov, A. A. Dynamics of a plasma channel created by the wakefield of a short laser pulse. *Physics of Plasmas* **10,** 1124–1134 (2003).

127. Chizhonkov, E. & Gorbunov, L. Numerical modelling of ion dynamics in the 3D nonlinear wakefield. *Russian Journal of Numerical Analysis and Mathematical Modelling* **16,** 235–246 (Jan. 2001).

128. Rosenzweig, J. B., Cook, A. M., Scott, A., Thompson, M. C. & Yoder, R. B. Effects of Ion Motion in Intense Beam-Driven Plasma Wakefield Accelerators. *Physical Review Letters* **95,** 195002 (Oct. 2005).

129. Assmann, R. W. *et al.* EuPRAXIA Conceptual Design Report. *The European Physical Journal Special Topics* **229,** 3675–4284 (Dec. 2020).

Publications by the Author

- Gao, Y., Bin, J., Haffa, D., Kreuzer, C., Hartmann, J., Speicher, M., Lindner, F. H., Ostermayr, T. M., Hilz, P., Rösch, T. F., Lehrack, S., Englbrecht, F., Seuferling, S., **Gilljohann, M.**, Ding, H., Ma, W., Parodi, K. and Schreiber, J. An automated, 0.5 Hz nano-foil target positioning system for intense laser plasma experiments. High Power Laser Sci. Eng. 5, e12 (2017).

- Döpp, A., Hehn, L., Götzfried, J., Wenz, J., **Gilljohann, M.**, Ding, H., Schindler, S., Pfeiffer, F. and Karsch, S. Quick x-ray microtomography using a laser-driven betatron source. Optica 5, 199 (2018).

- Götzfried, J., Döpp, A., **Gilljohann, M.**, Ding, H., Schindler, S., Wenz, J., Hehn, L., Pfeiffer, F. and Karsch, S. Research towards high-repetition rate laser-driven X-ray sources for imaging applications. Nucl. Instruments Methods Phys. Res. Sect. A Accel. Spectrometers, Detect. Assoc. Equip. 909, 286–289 (2018).

- **Gilljohann, M. F.**, Ding, H., Döpp, A., Götzfried, J., Schindler, S., Schilling, G., Corde, S., Debus, A., Heinemann, T., Hidding, B., Hooker, S. M., Irman, A., Kononenko, O., Kurz, T., Martinez de la Ossa, A., Schramm, U. and Karsch, S. Direct Observation of Plasma Waves and Dynamics Induced by Laser-Accelerated Electron Beams. Phys. Rev. X 9, 011046 (2019).

- Haffa, D., Yang, R., Bin, J., Lehrack, S., Brack, F.-E., Ding, H., Englbrecht, F. S., Gao, Y., Gebhard, J., **Gilljohann, M.**, Götzfried, J., Hartmann, J., Herr, S., Hilz, P., Kraft, S. D., Kreuzer, C., Kroll, F., Lindner, F. H., Metzkes-Ng, J., et al. I-BEAT: Ultrasonic method for online measurement of the energy distribution of a single ion bunch. Sci. Rep. 9, 6714 (2019).

- Martinez de la Ossa, A., Assmann, R. W., Bussmann, M., Corde, S., Couperus Cabadağ, J. P., Debus, A., Döpp, A., Ferran Pousa, A., **Gilljohann, M. F.**, Heinemann, T., Hidding, B., Irman, A., Karsch, S., Kononenko, O., Kurz, T., Osterhoff, J., Pausch, R., Schöbel, S. and Schramm, U. Hybrid LWFA–PWFA staging as a beam energy and brightness transformer: conceptual design and simulations. Philos. Trans. R. Soc. A Math. Phys. Eng. Sci. 377, 20180175 (2019).

- Schindler, S., Döpp, A., Ding, H., **Gilljohann, M.**, Götzfried, J. and Karsch, S. Tunable X-ray source by Thomson scattering during laser-wakefield acceleration. in Laser Acceleration of Electrons, Protons, and Ions V (eds. Esarey, E., Schroeder, C. B. and Schreiber, J.) 22 (SPIE, 2019). doi:10.1117/12.2520354.

- Wenz, J., Döpp, A., Khrennikov, K., Schindler, S., **Gilljohann, M. F.**, Ding, H., Götzfried, J., Buck, A., Xu, J., Heigoldt, M., Helml, W., Veisz, L. and Karsch, S.

Dual-energy electron beams from a compact laser-driven accelerator. Nat. Photonics 13, 263–269 (2019).

- Ding, H., Döpp, A., **Gilljohann, M.**, Götzfried, J., Schindler, S., Wildgruber, L., Cheung, G., Hooker, S. M. and Karsch, S. Nonlinear plasma wavelength scalings in a laser wakefield accelerator. Phys. Rev. E 101, 023209 (2020).

- Götzfried, J., Döpp, A., **Gilljohann, M. F.**, Foerster, F. M., Ding, H., Schindler, S., Schilling, G., Buck, A., Veisz, L. and Karsch, S. Physics of High-Charge Electron Beams in Laser-Plasma Wakefields. Phys. Rev. X 10, 041015 (2020).

- Raj, G., Kononenko, O., **Gilljohann, M. F.**, Doche, A., Davoine, X., Caizergues, C., Chang, Y.-Y., Couperus Cabadağ, J. P., Debus, A., Ding, H., Förster, M., Goddet, J.-P., Heinemann, T., Kluge, T., Kurz, T., Pausch, R., Rousseau, P., San Miguel Claveria, P., Schöbel, S., et al. Probing ultrafast magnetic-field generation by current filamentation instability in femtosecond relativistic laser-matter interactions. Phys. Rev. Res. 2, 1–7 (2020).

- Kurz, T., Heinemann, T., **Gilljohann, M. F.**, Chang, Y. Y., Couperus Cabadağ, J. P., Debus, A., Kononenko, O., Pausch, R., Schöbel, S., Assmann, R. W., Bussmann, M., Ding, H., Götzfried, J., Köhler, A., Raj, G., Schindler, S., Steiniger, K., Zarini, O., Corde, S., et al. Demonstration of a compact plasma accelerator powered by laser-accelerated electron beams. Nat. Commun. 12, 2895 (2021).

- Couperus Cabadağ, J. P., Pausch, R., Schöbel, S., Bussmann, M., Chang, Y.-Y., Corde, S., Debus, A., Ding, H., Döpp, A., Foerster, F. M., **Gilljohann, M.**, Haberstroh, F., Heinemann, T., Hidding, B., Karsch, S., Koehler, A., Kononenko, O., Knetsch, A., Kurz, T., et al. Gas-dynamic density downramp injection in a beam-driven plasma wakefield accelerator. Phys. Rev. Res. 3, L042005 (2021).

Acknowledgements

I want to thank all my colleagues and people that I got to know during my PhD for one of the most interesting times in my life.

Thanks to my supervisor **Stefan Karsch**, who is unarguably the most experienced and competent person in all parts of optics and other fields that I know. From no one I learned as much during my PhD. Thank you for all the patience and commitment to your group, the freedom you gave us to tackle all the challenges in new and interesting ways, and also for all the long nights you spent helping us with the experiments.

Thanks to **Andreas Döpp**, who is an expert in 'generally knowing what to do' and presenting the results and opportunities of our work in the way they deserve. Without you, our research would probably not have reached all the audience it is reaching now.

Thanks to all my (former) co-PhD colleagues and students in our group for your incredible amount of time and dedication in preparing and running the experiments with me: **Hao Ding**, **Johannes Götzfried**, **Sabine Schindler** and our students **Felix** 'Guardian Of The Bonsai' **Daiber**, **Christoph Eberle**, **Moritz Foerster** (who later became a Doktorand), **Tim Hager**, **Tobias Heider**, **Mathias Hüther**, **Lucas Prins** and **Ludwig Wildgruber**. Thanks also to all the new group members that arrived shortly before I left Garching for the nice discussions: **Katinka Grafenstein**, **Florian Haberstroh**, **Faran Irshad** and **Enes Travac**.

Thanks to **Gregor Schilling**, our laser engineer and all-around technical expert, for giving me a much better understanding in many technical fields and all your great work.

Thanks to the old team and the PFS group for all the nice beers, coffee breaks and all you taught me: **Benedikt Günther**, **Matthias Heigoldt**, **Olga Jahn**, **Alexander Kessel**, **Mathias Krüger**, **Konstantin Khrenikov**, **Andreas Münzer**, **Antonia Popp**, **Christoph Skrobol** and **Johannes Wenz**.

Thanks to Jörg Schreiber and his whole group for their dedication in LEX and the great time we spent: **Daniel Haffa**, **Leonard Doyle**, **Martin Speicher**, **Jens Hartmann**, **Florian Lindner**, **Thomas Rösch**, **Ying Gao**, **Johannes Gebhart** and everyone else.

Thanks to **Katharina Adler**, **Klaus Franke**, **Martin Gross**, **Felix Rauscher**, **Florian Saran**, **Karolina Schneider**, **Hans Wirth**, the mechanical and the electronical workshop, and everyone else I worked with for your great support.

Thanks to all of the people from our hybrid collaboration and IMPRS-APS for the great meetings and discussions.

Und, am allerwichtigsten, vielen Dank an meine liebste Familie. Ich hätte es niemals ohne euch geschafft. Ihr seid und wart immer für mich da, seid meine besten Freunde, und werdet immer die wichtigsten Plätze in meinem Herzen haben.